**UNIVERSITY OF SOUTHAMPTON**

FACULTY OF ENGINEERING AND THE ENVIRONMENT
AERODYNAMICS AND FLIGHT MECHANICS

# Aeroacoustic Investigation of Aircraft Spoiler During Steep Approach

by

Kondwani Kanjere

Thesis Submitted for the Degree of Doctor of Philosophy

November 2013

UNIVERSITY OF SOUTHAMPTON

ABSTRACT

FACULTY OF ENGINEERING AND THE ENVIRONMENT
AERODYNAMICS AND FLIGHT MECHANICS

Doctor of Philosophy

**Aeroacoustic Investigation of Aircraft Spoiler During Steep Approach**

by Kondwani Kanjere

A computational aeroacoustic investigation is performed of a two-dimensional and three-dimensional high-lift system in steep approach landing configuration in order to identify the noise impact of the deflected spoiler. Computations are performed on a conventional HLD without the spoiler, a steep HLD with a full-span and half-span spoiler deployed at 20 degrees. A hybrid strategy is used to compute the far-field noise using the Ffowcs-Williams and Hawking integral method. Deflecting the spoiler increase the overall noise from the high-lift model with the maximum increase confined to low frequencies.

The deflected spoiler reduces the frequency of vortex shedding behind the flap by half. The farfield noise spectra from the steep HLDs have a peak at the frequency corresponding to the vortex shedding. Deploying the spoiler caused the expansion of the slat cove vortex. The three-dimensional simulations show that the slat farfield noise reduce when the spoiler is deflected. Simulation of the half-span spoiler show that a streamwise vortex forms at the side-edge of the spoiler similar to the flap side-edge. The vortex induces both broadband and tonal noise increase due to its interaction with the main-element, spoiler and flap.

Initial 2D simulations have shown the perforations on the spoiler reduces the low frequency vortex shedding behind the flap, thus reducing the spoiler noise impact at the low frequencies.

# Contents

# List of Figures

# List of Tables

# Declaration of Authorship

I, .....
declare that this thesis and the work presented in it are my own and has been generated by me as the result of my own original research.

**Aeroacoustic Investigation of Aircraft Spoiler During Steep Approach**

I confirm that:

1. This work was done wholly or mainly while in candidature for a research degree at this University;
2. Where any part of this thesis has previously been submitted for a degree or any other qualification at this University or any other institution, this has been clearly stated;
3. Where I have consulted the published work of others, this is always clearly attributed;
4. Where I have quoted from the work of others, the source is always given. With the exception of such quotations, this thesis is entirely my own work;
5. I have acknowledged all main sources of help;
6. Where the thesis is based on work done by myself jointly with others, I have made clear exactly what was done by others and what I have contributed myself;
7. Part of this work have been published as:
   K. Kanjere, X. Zhang, Z. Hu, and D. Angland. Aeroacoustic Investigation of Deployed Spoiler During Steep Approach Landing. *16th AIAA/CEAS Aeroacoustics Conference*, Stockholm, Sweden,07-09 June 2010.

Signed: .....

Date: .....

# Acknowledgements

First and foremost, I would like to thank Professor Xin Zhang and Dr David Angland for their guidance, encouragement and inspiration in this work.

I would like to extend my warmest thank you to the following friends I have met during my PhD here at Southampton University; Angelo, Cindy, Cheryl, Ed, Jaye, Jean, Koen, Max, Sammie and Phil. Thanks for the morning footie, afternoon coffees and the summer cricket action.

A very special thanks to my wonderful wife Katie for her unfaltering love and constant support throughout my PhD. *Ndimakukonda kwambirimbiri.*

My most gratitude to my parents and the rest of my family for their unconditional support and encouragement throughout my life. All this would not have been possible without you.*Zimatha!, Zaitwa!, Zikomo!.*

*I dedicate this thesis to my wonderful mum. None of this would have been possible if it was not for all your hard work. Words cannot express how grateful I am.*

*To my son Oliver, your arrival gave me the added motivation to finish this work.*

# Nomenclature

All units are in SI

## Alphanumeric

| | |
|---|---|
| $c$ | Speed of sound, m/s |
| $C_D$ | Drag coefficient |
| $C_{DES}$ | Constant in DES model |
| $C_L$ | Lift coefficient |
| $C_p$ | Pressure coefficient; $(p - p_\infty)/\frac{1}{2}\rho_\infty U_\infty^2$ |
| $C$ | Reference chord, m |
| $c_F$ | Flap chord, m |
| $c_p$ | Specific heat at constant pressure J/g.K |
| $d$ | Length scale for SA model, m |
| $\tilde{d}$ | Modified length scale for DES model, m |
| $E$ | Total Energy, J/kg |
| $E(f)$ | Power Spectral Density, dB/Hz |
| $e$ | Internal specific energy, J/kg |
| $f$ | Frequency, Hz |
| $H(f)$ | Heaviside function |
| $I$ | Acoustic Intensity, W/m$^2$ |
| $k$ | Turbulent kinetic energy, m$^2$/s$^2$ |

| | |
|---|---|
| $l_o$ | Correlation length of acoustic sources, m |
| $M$ | Mach number |
| $p$ | Static pressure, N/m$^2$ |
| $P$ | Acoustic Power, $W$ |
| $P_{ij}$ | Compressive stress tensor, N/m$^2$ |
| $P_r$ | Prandtl number |
| $Pr_t$ | Turbulent Prandtl number |
| $Re$ | Reynolds number |
| $r$ | Distance to observer in farfield, m |
| $St$ | Strouhal number |
| $S_{ij}$ | Strain rate tensor, 1/s |
| $t$ | Flow time, s |
| $T$ | Static temperature, K |
| $T_{ij}$ | Lighthill stress tensor, N/m$^2$ |
| $u^+$ | Non-dimensional velocity |
| $u_n$ | Velocity normal to a boundary, m/s |
| $U$ | Velocity magnitude, m/s |
| $u, v, w$ | Velocity components in Cartesian coordinates |
| $V$ | Non-linear region in acoustic analogy |
| $x, y, z$ | Cartesian coordinate system |
| $y^+$ | Non-dimensional wall distance |

## Greek

| | |
|---|---|
| $\alpha$ | High-lift model angle of attack, degrees |
| $\Delta x$, $\Delta y$, $\Delta z$ | Cell dimensions in $x$, $y$ and $z$ directions, m |
| $\delta_F$ | Flap deflection angle, degrees |

| | |
|---|---|
| $\delta_S$ | Slat deflection angle, degrees |
| $\delta_s$ | Spoiler deflection angle, degrees |
| $\delta(f)$ | Dirac delta function |
| $\delta_{ij}$ | Kronecker delta function |
| $\Delta t$ | Physical timestep size, seconds |
| $\delta^*$ | Boundary layer displacement thickness, m |
| $\epsilon$ | Turbulent dissipation rate, $m^2/s^3$ |
| $\gamma$ | Ratio of specific heats |
| $\mu$ | Molecular viscosity, $Ns/m^2$ |
| $\mu_t$ | Turbulent viscosity, $Ns/m^2$ |
| $\nu$ | Kinematic viscosity, $m^2/s$ |
| $\nu_t$ | Eddy viscosity, $m^2/s$ |
| $\tilde{\nu}$ | Modified eddy viscosity in SA model, $m^2/s$ |
| $\theta$ | Farfield noise radiation angle, degrees |
| $\tau_{ij}$ | Shear stress tensor, $N/m^2$ |
| $\rho$ | Fluid density, $kg/m^3$ |
| $\omega$ | Vorticity, $1/s$ |

## Symbols

| | |
|---|---|
| $^-$ | Time averaged quantity |
| $'$ | Fluctuating component |

## Subscripts

| | |
|---|---|
| $_\infty$ | Freestream value |
| $_{rms}$ | Root mean square value |

## Abbreviations

| | |
|---|---|
| 2D | Two-dimensional |

| | |
|---|---|
| 3D | Three-dimensional |
| ACARE | Advisory Council for Aeronautics Research in Europe |
| AIAA | American Institute of Aeronautics and Astronautics |
| CAA | Computational Aeroacoustics |
| CFD | Computational Fluid Dynamics |
| CFL | Courant-Friedrichs-Lewy |
| DES | Detached Eddy Simulation |
| DNS | Direct Numerical Simulation |
| FW-H | Ffowcs-Williams and Hawkings |
| FFT | Fast Fourier Transform |
| HLD | High Lift Devices |
| LES | Large Eddy Simulation |
| PIV | Particle Image Velocimetry |
| PSD | Power Spectral Density |
| RANS | Reynolds-Averaged Navier-Stokes |
| S-A | Spalart-Allmaras turbulence model |
| SPL | Sound Pressure Level |
| SST | Shear Stress Transport |
| URANS | Unsteady Reynolds-Averaged Navier-Stokes |

# Chapter 1

# Introduction

The airframe noise of an aircraft on approach to landing can be reduced by adopting steep approach landing procedures that utilise a steeper glide slope compared to the conventional 3 degrees glide slope. However a steep approach is limited by the descent velocity for passenger comfort. In order to slow down the aircraft near to the airport perimeter, spoilers can be deployed. The impact of the deployed spoiler on the noise from the high-lift devices is not yet understood.

In this thesis, a computational aeroacoustic investigation is performed on a high-lift wing in steep approach landing with the spoiler deployed in order to investigate the noise impact of the spoiler. The results help to quantify and characterize spoiler noise as well as reveal some of the underlying flow physics of noise generation from a high-lift wing with deployed spoiler. The understanding of the noise mechanisms is used to develop noise reduction methods that can be applied to reduced spoiler noise.

## 1.1 Background and Motivation

Advances in low noise high bypass ratio turbofan engines have resulted in a reduction in jet engine noise such that on approach to landing, when the engines are operating at a low power setting, airframe noise becomes the dominant noise source. Airframe noise is defined as the "non-propulsive noise of an aircraft in flight, due to the airflow around the airframe" [1]. The major contributors to airframe noise are landing gears and high-lift devices. Airframe noise causes a lot of annoyance for the communities living near airports. The growth in air traffic

at major airports in recent years has resulted in an increase in complaints from the local communities around airports. This has led to governments introducing more stringent noise regulations. Evidently there has been an increased interest in research to understand airframe noise generation mechanisms in order to find ways of reducing aircraft noise impact on communities around airports.

Steep approach landing procedure utilizes a steeper glide slope compared to the conventional 3 degrees glide slope to reduce noise on the ground. By adopting a steeper glide angle, the aircraft flies at higher altitudes over residential areas close to the airport. The engines can be operated at lower power settings because the amount of thrust required to maintain the approach speed is reduced. The combined effect of reduced engine power and greater altitude is a reduction in the noise levels on the ground. Steep approach landing procedures are currently operated at several airports e.g. London City Airport (LCY). At London City Airport, all aircraft must be capable of making an approach at 5.5 degrees or steeper glide slope in order to operate at the airport. In addition to reducing noise level on the ground, steep approach allows the aircraft to clear obstacles along the flight path e.g. tall buildings around the airport perimeter.

The noise reduction potential of steep approaches has been demonstrated in several studies. Antoine and Kroo [2] estimated the noise reduction due to a steep approach at a glide angle of 4.5 degrees to be as much as 7.7 dB compared to conventional landing at a glide angle of 3 degrees. Clarke *et al.* [3] performed flight tests at Louisville International Airport that showed steep approach landing procedures reduced the A-weighted peak noise level along the flight path by 3.9 to 6.5 dBA. The study also showed that steep approach reduced the fuel consumption during approach, due to the reduce engine power requirement.

Steep approach is limited by the descent velocity requirement for passenger comfort. Dobrzynski [4] suggests the descent velocity should not exceed 1100 ft/min (5.588 m/s). In FAR/JAR 25.723 the maximum landing descent velocity is 3.66 m/s. In order to meet the descent velocity requirements, spoilers can be deployed as air brakes to slow down the aircraft. A spoiler is a small hinged flat plate that, when deflected, spoils the flow on the suction surface of a wing. It works by increasing the drag and reducing the lift generated by the wing. Conventionally, spoilers are operated on the ground during landing to aid in braking by dumping the lift thereby placing the weight of the whole aircraft on the landing gear and slowing the aircraft by creating drag.

In steep approach flight tests performed by Clarke *et al.* [3], it was noted that

pilots used air brakes (spoilers) to slow down the aircraft on a steep approach. They reported that use of the air brakes resulted in increased noise levels on the ground. However there was no quantitative data on the noise impact of the deployed spoilers. Quantitative data on spoiler noise were obtained by Kipersztok and Sengupta [5], who performed flight tests of a 747 aircraft to investigate the noise contribution from different airframe components. The individual component noise contribution was isolated by logarithm subtraction of the noise level of the clean configuration from the configuration with the component deployed. The noise radiated by the extension of the spoilers caused an increase in level of 3 dB throughout the entire spectrum (up to 8 kHz). The noise spectrum of the isolated spoiler had a peak at a lower frequency of 80 Hz. Dobrzynski [4] also concluded that the spoiler self noise is primarily a low frequency phenomenon. Unpublished noise source distribution on a scale model showed reduced slat noise with a deflected spoiler. This was attributed to the local effect of the deflected spoiler on the slat sectional lift. Dobrzynski [4] conjectured that the spoiler self noise generation mechanism may be similar to the flap side-edge noise problem.

It is evident that there is little data available to date to quantify and characterise spoiler noise. As a result the understanding of the relevant noise generation mechanisms is very limited. The thesis presents an attempt to fill in the gap in the understanding of spoiler noise mechanisms through dedicated numerical simulations.

## 1.2 Aims of Research

A numerical study of spoiler aerodynamics and aeroacoustics during steep approach as part of a new landing procedure to alleviate noise pollution is performed. The aim of the research is to get a better understanding of the noise generation mechanisms on a high-lift wing with the spoiler deployed. The understanding of the noise generation can be used in the development of noise reduction techniques for aircraft in steep approach.

The novelty of the current research is in the computation of entire HLD configurations with a deflected spoiler using high-order accurate numerical schemes. To date there are no publicly available literature on the aeroacoustic simulation of entire high-lift wings with a spoiler.

In this research, 2D and 3D simulations are performed of: a high-lift wing with

a deployed spoiler, from here on referred to as *steep* configuration and a high-lift wing with the spoiler retracted, from here on referred to as *conventional* configuration. The simulations are conducted following a hybrid strategy where the noise generation and the noise propagation are uncoupled. The unsteady flow field around the HLDs is obtained using a high-order and low-order flow solvers. The unsteady flow is then used as inputs to a Ffowcs-Williams and Hawkings [6] (FW-H) integral method to compute the far-field noise spectra and directivity. Detailed comparisons of the near-field flow and the far-field noise are used to identify relevant noise generation mechanisms.

The following research goals have been achieved:

- Simulation of the two-dimensional and three-dimensional flow around the conventional and steep HLDs.
- Computation of the far-field noise from the conventional and steep HLDs using FW-H integral method.
- Simulation of the three-dimensional flow around the steep HLDs with a half-span spoiler and computation of the far-field noise.
- The impact of the spoiler on the near unsteady flowfield around the HLDs and its associated far-field acoustic radiation has been identified and analysed.
- A noise reduction treatment for HLDs with a spoiler has been proposed based on the understanding of the noise generation mechanisms obtained from the analysis of the results from the simulations.

## 1.3 Structure of Thesis

The thesis is organised into seven chapters. Chapter 2 is a review of the relevant literature pertaining to high-lift noise. This chapter also includes discussion of literature pertaining to wings with deployed spoiler.

Details of the numerical methods employed in this work are outlined in Chapter 3. The description of the numerical schemes employed in the two CFD solvers used in this work is given. The two solvers used are: a high-order finite difference CFD/CAA solver, SotonCAA, which is further developed as part of this work; and

a low-order commercial finite volume CFD solver which is used for simulation of more complex geometry that employs unstructured meshes. Also included in this chapter is a description of the far-field acoustic solver which employs the FW-H integral formulation.

Chapter 4 discusses the results obtained from the 2D simulations of the conventional and steep HLDs. The 2D simulations are performed using the high-order finite difference CFD solver SotonCAA. Chapter 5 outlines the results from 3D simulations of the conventional and steep HLDs. The simulations are performed using the high-order finite difference CFD/CAA solver SotonCAA.

Chapter 6 contains results of the 3D simulations of the steep HLDs with a half-span spoiler. The simulations are performed using the low-order commercial finite volume CFD code. The aims of the 3D simulations in Chapter 5 and 6 are to confirm the 2D results and to investigate the contribution of the spoiler side-edge flow field to the far-field noise respectively.

The results from the 2D simulations of the noise reduction treatment are differed to Appendix A. The simulations are performed using the low-order commercial CFD solver.

Finally, Chapter 7 contains the conclusions and recommendations for further work.

# Chapter 2

# Literature Review

## 2.1 Introduction

One of the major sources of airframe noise for an aircraft on approach to landing is due to the flow around the high-lift devices (HLD). The HLD typically consist of the leading edge slat and the trailing edge flaps. On landing approach, the high-lift devices are deployed to increase the lift generated by the wing. The complex flow field around the high-lift devices involves unsteady phenomena such as flow separation and shear layer instability forming vortices (for example in the slat cove and flap side-edge). The complex flow features on the high-lift system are illustrated in Fig. 2.1. The pressure fluctuations arising from these complex flows can radiate to the far-field as sound. In this chapter, literature pertaining to high-lift device noise is reviewed with emphasis on the relevant noise mechanisms, the far-field noise spectra and directivity.

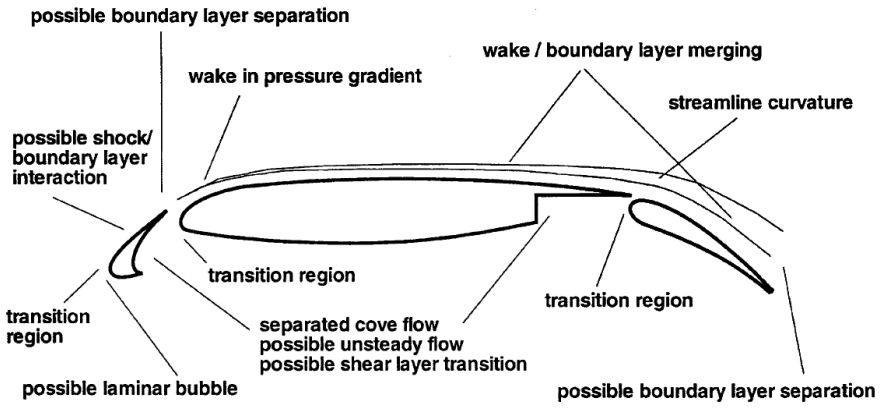


FIGURE 2.1: Schematic showing the complex flow field around a high lift system

## 2.2 Slat Noise

The slats have been identified as the most dominant source of noise for large passenger aircraft. Fink and Schlinker [7] performed measurements on a 2D wing section with deployable slats, flap and a landing gear. Slat noise spectra at different freestream velocity collapsed when the amplitudes were scaled with the velocity to the fifth power. A directional microphone measured the maximum slat noise at the slat trailing edge. Dobrzynski *et al.* [8] conducted measurements on a 1/10th scale-model wing section to identify the aeroacoustic source mechanisms of slat noise. The broadband slat noise spectra collapsed when the levels were normalised by the flow velocity to the power of 4.5 and plotted against the Strouhal number based on the slat chord as the reference length dimension.

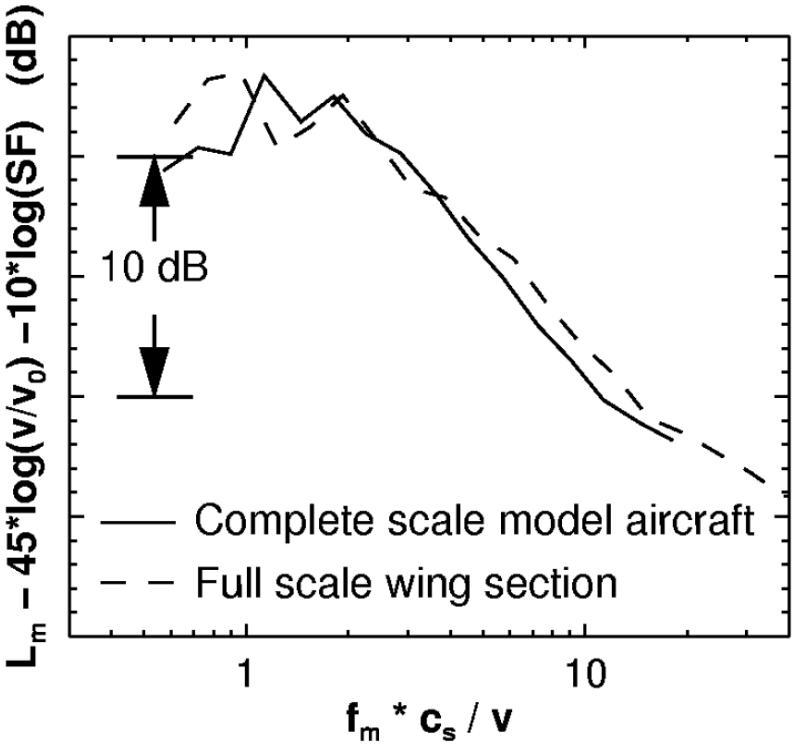


FIGURE 2.2: Comparison of the normalised spectra from a scaled complete aircraft model and a full scale wing section.

Figure 2.2 shows a typical slat noise spectra obtained from noise measurements on a scaled 1/7.5 complete aircraft model and on the outer section of a full scale A320 wing [9]. The noise generated by the slat is shown to scale with the velocity to the power 4.5. Guo and Joshi [10] performed an airframe noise test on a 4.7% DC-10 model in the 40-by-80 ft wind tunnel at NASA Ames Research Center. They found that slat noise scaled with the velocity to the power of 5.0. The fact

that the exponent is closer to 5 lends support to the hypothesis that the slat noise mechanism is associated with the scattering of turbulent flow by the slat trailing edge [7, 9]. Based on these findings, Dobrzynski and Pott-Pollenske [11] formulated a slat noise model which approximate the trailing edge source directivity by that of a compact edge dipole shown in Fig. 2.3. Guo and Joshi [10] attributes the fifth power of velocity scaling law to the approximately two dimensional geometry of the slat, which introduce 2D sources, that scale according to the fifth power law.

The maximum slat noise level occurs at low Strouhal numbers between 1 and 2 (Fig. 2.2). The Strouhal number is based on the slat chord as the characteristic length and the freestream velocity as the characteristic velocity. Guo and Joshi [10] also found that slat noise was dominant over the flap noise at low-to-mid frequencies.

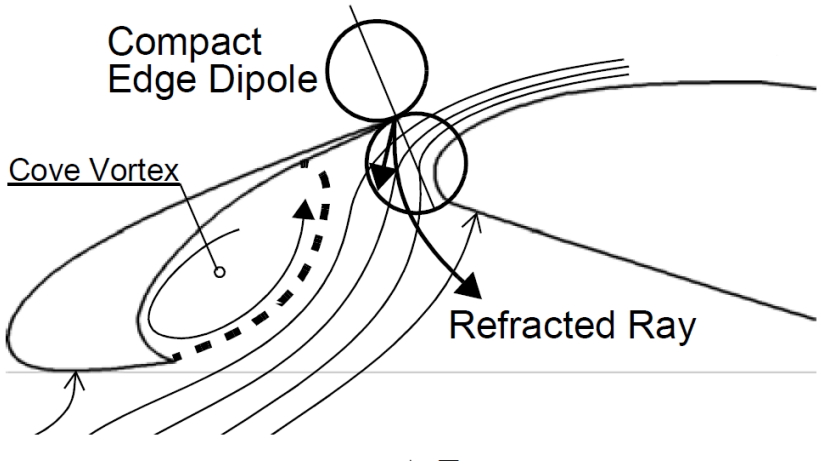


FIGURE 2.3: Schematic representation of the slat geometry of an idealized slat trailing edge compact dipole source.

The slat noise directivity shows maximum levels in the rear arc radiation direction [9, 10]. Increasing the angle of attack causes an increase in slat noise levels [9]. According to Soderman *et al.*[12] this is caused by the increase in wing circulation and in the local flow velocity through the slat gap and at the slat trailing edge. The effect of deploying a spoiler is a reduction in the wing circulation and a corresponding reduction in the low flow velocity in the slat gap. Therefore it is expected that deploying the spoiler will result in a reduction in slat noise. This effect of a deflected spoiler on slat noise is reported by Dorbzynski [4]. However in a separate study on a generic 2D high lift wing model in AWB, Dobrzynski and Pott-Pollenske [11] showed that decreasing the angle of attack caused the cove vortex to expand and turbulent levels near the slat trailing edge were increased. Therefore the effect of reducing the wing circulation can result in the expansion of

the slat cove vortex and an increase in the turbulence intensity. The current work is aimed at getting a better understanding of the effects of deploying the spoiler on the flow field around the slat and the far-field noise.

### 2.2.1 Slat Noise Mechanism

The vortex shedding at the slat trailing edge was identified as an important slat noise source, therefore became the subject of experiments and CFD simulations. An experiment in the NASA Langley Research Center's Low-Turbulence Pressure Tunnel (LTPT) showed that the noise measured from a slat deployed at 30 degrees had a large amplitude peak at high frequency which was absent at a slat deflection of 20 degrees [13]. Unsteady Reynolds-Averaged Navier-Stokes (URANS) simulations [14] on a 2D model showed vortex shedding from the slat trailing edge at a deflection of 30 degrees which was absent for slat deflection at 20 degrees. Using an FW-H integral method, Singer *et al.* [15] calculated the far-field noise from the near field fluctuations of the 2D computations of reference [14]. Overall, the results agreed well with the measurements from LTPT experiment. This led the investigators to conclude that the source of the high amplitude peak at high frequency was the vortex shedding from the slat trailing edge. Takeda *et al.* [16] performed a simulation of a 2D simplified high-lift model. An FW-H integral method was used to compute far-field noise levels. A dipole-type source radiating at the vortex shedding frequency was identified as the slat trailing edge noise source.

Experiments and simulations have shown that the free shear layer that emanates from the slat cusp is an important flow feature in the generation of slat broadband noise. Figure 2.4 shows an instantaneous Particle Image Velocimetry (PIV) snapshot of the typical flow in the slat cove. Discrete vortical structures form in the shear layer that emanates from the slat cusp (cove lip). The vortices move along the shear layer towards the reattachment point. At the reattachment point some vortices are trapped in the recirculation region whereas others escape through the gap between the slat and the main-element. The highest turbulent kinetic energy levels occur at the reattachment point, where the shear layer impinges on the slat cove surface. The reattachment point has been identified as a source of low frequency noise in a companion simulation by Khorrami *et al.* [17]. Increasing the angle of attack causes a reduction in the peak turbulent kinetic energy levels.

As discussed above, PIV measurements have shown that the shear layer is unstable

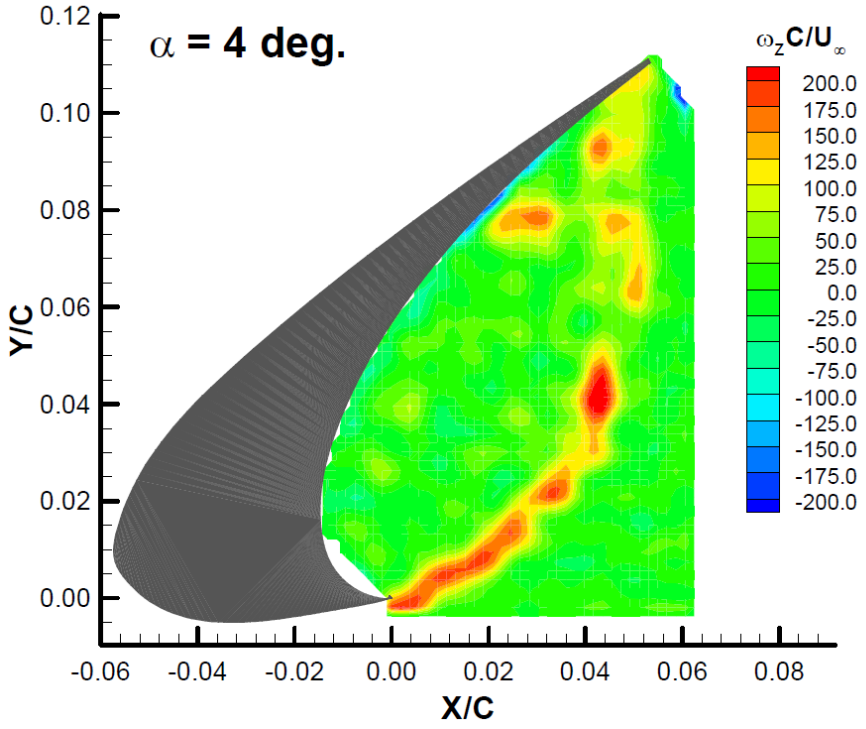


FIGURE 2.4: Instantaneous PIV snapshot of the flow in the slat cove for angle of 4 degrees.

and rolls up into discrete vortices. Modeling such a flow phenomenon using URANS proved very challenging. Early on, fully turbulent simulations required external forcing of the free shear layer to excite and maintain the large-scale vortical structures [18]. However, fully turbulent simulations were found to be overly diffusive and the rolled up discrete vortices rapidly decayed within a short distance from the slat cusp. Later Khorrami *et al.* [19] performed URANS simulation in which the turbulent production term in the turbulence transport equation was switched off in the slat cove region to eliminate the excessive diffusive effect of the turbulence model. He argued that, due to the relatively small Reynolds number and the short distance between the stagnation point and the slat cusp coupled with the strong favourable pressure gradient in this region, the flow in the cove can be considered to be"quasi-laminar". This modification allowed the free shear layer to naturally roll up into discrete vortices without any external forcing. The far-field acoustics computed from the simulation showed higher amplitudes compared with experiment. This was due to the perfect spanwise correlation assumed for the 2D near-field unsteady signal in the FW-H computation. In contrast, in the experiment, the 3D effects produce a spanwise correlation that is less than perfect.

In order to account for the 3D effects on slat noise, Choudhari and Khorrami

[20] performed a 3D simulation of an unswept three-element high-lift wing. The results showed that accounting for the 3D nature of the flow fluctuations leads to improved agreement with the experimental results. The high intensity turbulent fluctuations near the reattachment point were identified as significant in the generation of broadband slat noise. Imamura *et al.* [21] also performed a 3D unsteady simulation of flow in the slat cove of a high-lift wing. A zonal LES/RANS methodology was used where the slat region was computed using LES and the rest of the flow was computed using RANS with Spalart-Allmaras turbulence model. A switching function was used in the region between the LES and RANS. The power spectral density of the coefficient of pressure agreed very well with experimental measurements. High frequency narrowband and low frequency broadband fluctuations were observed. The frequency of the narrowband peak agreed very well with the frequency of pressure fluctuations from the slat trailing edge due to vortex shedding. The authors conjectured that the source of the low frequency broadband noise was the longitudinal vortical structures that form when the shear layer impinges on the slat lower surface. The two computational studies above highlight the importance of 3D computations in the slat cove region.

In continuing with the investigation of the unsteady flow in the slat, Lockard and Choudhari [22] performed simulations to examine the effects of cross flow on the near field fluctuations and far-field acoustics. The cross flow was imposed by changing the freestream velocity vector and modifying the Reynolds number. They found that the cross flow changed the flow dynamics in the slat cove, however it did not have any impact on far-field noise. Since the Mach number and the Reynolds number were varied simultaneously, separating out their individual effect proved difficult.

### 2.2.2 Slat Noise Reduction

Dobrzynski *et al.* [9] applied a slat cove cover designed to attenuate the strength of the vorticity in the free shear layer between the cove vortex and the slat gap flow. Previously the slat free shear layer and the slat cove vortex were identified as the source of broadband slat noise therefore the cover represented a reduction of the actual source quantity. The slat cove cover was tested on a 3D scale model aircraft in the wind tunnel and was shown to reduce the slat broadband noise. However the slat cove cover did not satisfy the operational aerodynamic performance constraints. The rigid cover could not be retracted for cruise flight and it was only optimal for one chosen angle of attack.

Khorrami and Lockard [23] used a similar approach using an extended seal that was attached to the slat cusp. Simulation of a 2D high-lift wing with the extended cove seal showed not only broadband noise reduction but also high frequency tonal noise reduction. The extended cove seal reduced the strength of the vortices growing in the free shear layer from the slat cusp and altered the wake instability at the slat trailing edge resulting in weaker shed vortices.

Following a similar idea to reduce the slat cove vortex strength, Horne *et al.* [24] applied a slat cove filler to a model scale slat in the NASA Ames 40 by 80 ft wind tunnel. Slat cove fillers completely cover the entire slat cove with a streamlined body eliminating the slat cove vortex entirely. Significant noise reduction potential was demonstrated. However it was noted that the slat cove filler was only effective in reducing noise at the design point. At different angles of attack which deviated slightly from the design point, the slat cove filler was found to potentially cause a noise increase.

Substantial noise reduction has been obtained by application of flow transparent edge replacement such as perforated/porous material [25, 26] or brushes [27] and edge modification such as serrated edges. According to Khorrami *et al.* [25] the serrations work by partially redirecting spanwise vorticity into streamwise vorticity and therefore significantly reduces spanwise correlations of the local turbulent fluctuations. However the appropriate design of any edge treatment must be carefully considered in order to not degrade the high-lift performance. For example, Ortmann and Wild [28] performed 3D simulations to study the effect of brushlike devices at the slat trailing edge on the aerodynamic properties of a high-lift system. They found that the brushes adversely affected the aerodynamic properties of a high-lift system, due to the influence on the slat wake.

Other noise reduction treatments that do not involve add-on devices include application of acoustic liners on the slat cove and main-element leading edge surface. In contrast to add-on devices, liners do not affect the source mechanisms. They work by attenuation of sound waves as they propagate between the slat cove and main-element leading edge. Ma and Zhang [29] performed a numerical investigation of the potential for acoustic liners in attenuating slat broadband noise. They found that acoustic liners treatment in the slat gap region were most effective in attenuating slat broadband noise.

## 2.3 Flap Noise

The flaps represent the next dominant source of high lift noise, especially on aircraft without slotted slats. Fink and Schlinker [7] found that the far-field noise spectra of the full and part-span flap coalesced when the levels were normalised with the sixth power velocity law. The noise radiation from a highly deflected flap was found to be a combination of noise caused by the wing's turbulent wake convected past the flap and the noise caused by the convection of the flap upper-surface separated flow past the flap side and trailing edges.

Hayes *et al.* [30] characterized the HLD noise sources of a 4.7% scale DC-10 model using the source maps obtained from phase microphone array data. With only the flap deployed the dominant noise source was found at the outboard edge of the inboard flap. When the slats were deployed, the dominant sources were the slats and the outboard edge of the outboard flap. They also found that increasing flap deflection resulted in an increase in flap noise. Flap noise directivity showed a forward radiation emphasis that diminished at higher frequencies. Based on these results, the authors suggested the noise generation mechanism was associated with a baffled dipole aligned with the flap side-edge.

Dobrzynski at al. [8] found that flap side-edge noise scaled with: a sixth power law in the mid-frequency range; a fifth power law in the low frequency range and a power law with a velocity exponent greater than six at high frequencies. The interaction of the separated and then reattaching turbulent flow with the flap side-edge surface was considered as a 3D dipole type sound source hence the predominance of a sixth power law in the mid-frequency range. The high power law at high frequency was found to be due to noise radiated from the rotation of inhomogeneous vorticity, originating from the flap boundary layer and sucked into the edge vortex. No effect of angle attack on the flap side-edge noise was detected for low and intermediate Strouhal numbers. At high Strouhal numbers there was a significant increase in noise with an increasing angle of attack due to the strengthening of the vortex by the increase in flap loading. Based on a unit radiation area, the source strength of flap side-edge noise was found to dominate at high frequencies.

Guo and Joshi [10] used a phased microphone array for source localisation and free field microphone to measure sound pressure spectra and directivity from 4.7% DC-10 scale model aircraft. The flap noise radiation was found to be typically that of the dipole type caused by unsteady pressure fluctuations on the flap, which

lead to the sixth power law. Noise sources associated with the flap had maximum radiation in the forward direction. Flap noise was found to be dominant at high frequencies (more than 10 kHz full scale), whereas slat noise was dominant at the low-to-mid frequencies $\approx 100 < f < 2500$ Hz for full scale.

### 2.3.1 Flap Noise Mechanism

Flap noise originates from the unsteady flow at the flap side-edge. The difference in lift between the flapped and unflapped portions of the wing with a part-span flap result in formation of a trailing vortex near the flap edge. Khorrami *et al.* [31] performed a 3D steady RANS simulation of the flow around a generic high-lift wing with a half span flap. The simulation captured the dual vortex system at the flap edge observed in the experiments. Figure 2.5 shows the development of this complex vortex system along the flap chord [31]. Near the flap leading edge, two vortices are formed at the lower and upper corner of the flap edge. The reattachment point of the side edge vortex moves up the edge as the flow

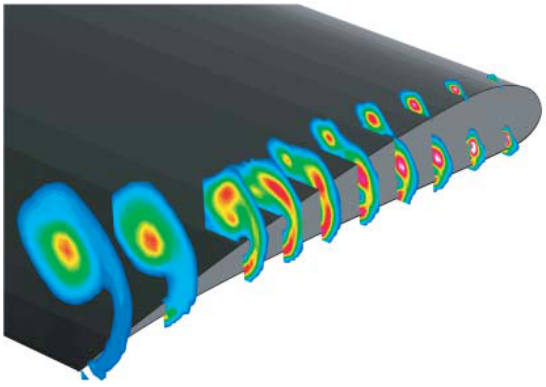

FIGURE 2.5: Development of the complex vortex system downstream of the flap side-edge.

moves down the flap chord, eventually reaching the upper corner. The side edge vortex then moves over the upper corner and merges with the upper surface vortex forming a single trailing vortex that separates from the flap surface. The location of the separation is dependent on the flap geometry and deflection. Vorticity from the cylindrical shear layer that originates from the lower edge corner is continuously "fed" into the trailing vortex. This produces a strong jet-like flow in the core of the vortex, where streamwise velocity can reach up to twice the freestream velocity. Streett [32] used the steady RANS of Khorrami *et al.* [31] as mean flow field within which unsteady disturbances were simulated. The simulation showed two basic disturbance modes; the first is associated with the instability of the cylindrical

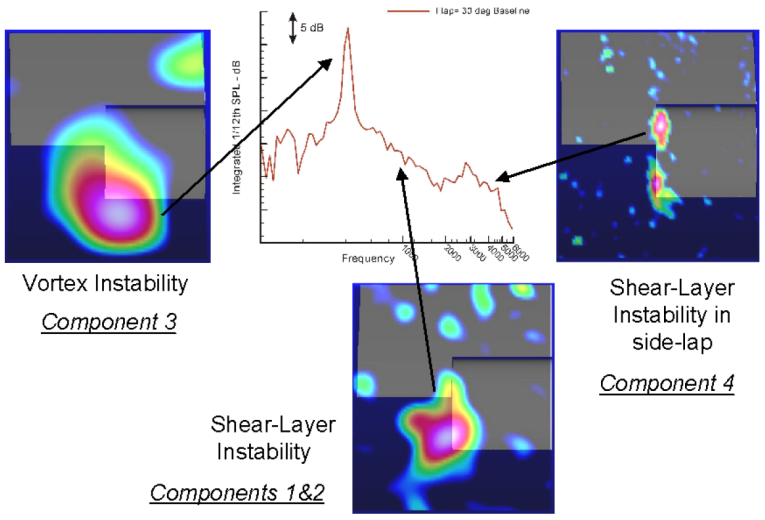


FIGURE 2.6: Flap side-edge noise spectrum and equivalent source maps from array measurements from LTPT experiement.

shear layer, which overlies the side-edge separation in the upstream portion, and feeds vorticity into the trailing edge vortex downstream. The second disturbance mode is associated with instabilities of the vortex and its jet-like core flow, which possesses a significant oscillatory structure in the streamwise direction. Figure 2.6 show a typical flap noise spectra with the corresponding noise source mechanisms for each spectral feature obtained from the LTPT experiments of Choundhari et al [13].

### 2.3.2 Flap Noise Reduction

This section outlines some of the noise reduction methods applied to the flap side-edge problem. From previous studies, the flap noise mechanism was attributed to the dynamics of the dual vortex system on the side edge of the flap. Therefore most flap noise reduction treatments were aimed at reducing the strength of this dual vortex system by eliminating, displacing, or altering the dynamics of the vortex.

Dobrzynski [9] demonstrated the effectiveness of flap-edge fences in reducing flap side-edge noise. Guo and Joshi [10] performed airframe noise tests on a 4.7% DC-10 aircraft model. They found that the flap-edge fences were most effective for high-frequency noise. However, the flap-edge fences were found to cause a noise increase at the low frequency. It was also found that the amount of noise reduction did not increase linearly with fence height. According to Choudhari and Khorrami [33], the flap side-edge fence delayed the roll-up of the shear layer and locked the

position of the side-edge near the bottom so that it could not merge with the vortex along the top edge and form a single dominant vortex. The side-edge fence adds a small amount of weight to the high-lift system that would have to be carried even through the cruise stage. In addition it may have a drag penalty associated with it.

Choudhari and Khorrami [33] showed the effectiveness of porous side-edge treatment as a passive means for flap noise reduction through steady Reynolds-Averaged Navier-Stokes computations. The porous surface treatment resulted in a milder variation in surface pressures along the flap side-edge. Since the near-field unsteadiness was not modeled, it was not possible to translate the above flow alterations into corresponding reductions in far-field sound pressure levels. Angland *et al.* [34] performed wind-tunnel experiments to investigate the flap side-edge vortex. A porous side-edge treatment was applied to a half-span flap which resulted in substantial broadband noise reduction. They found that the effect of the porous side-edge was to reduce the Reynolds stresses contained within the vortex and the shear layer and to displace the vortex further away from the flap surface. The effect of a porous edge on the aerodynamic performance was found to be negligible.

Another approach is to eliminate the flap side-edge vortex system through continuous moldline technology. Continuous moldline technology involves a flexible panel that deforms to provide a continuous surface between two movable parts (i.e. the main-element trailing edge and the flap side-edge). In a study conducted by Storms *et al.* [35], continuous moldline technology was applied at the flap tip junction of the wind tunnel model which comprised of a simplified wing with a half span hinged flap. The flap side-edge noise was almost eliminated to below measurable levels with the application of the continuous moldline technology. However it incurred an aerodynamic performance penalty as a result of the reduced overall lift and suffers from structural constraints due to its complexity for practical applications.

Koop *et al.* [36] used active flow control to reduce noise from a flap side-edge. Koop *et al.* applied blowing to displace or destroy the vortical structure near the flap side-edge. They conjectured that blowing air changed the circumferential velocity profile of the vortex and thus the dynamic interaction between the shear layer and the vortex instability. In addition, blowing displaces the vortical structure away from the solid surface which results in noise reduction.

## 2.4 Spoiler

The spoiler is a flat plate that when deflected spoils the flow on the suction surface of a wing. Spoilers consist of small, hinged flat plates of various back-side shapes which when retracted retain the airfoil sectional shape of the wing. Spoilers are used as effective control surfaces for lateral controls when deflected differentially (e.g. only on one wing). Spoilers are used as speed brakes to slow down the aircraft and cause it to descend by increasing the drag and reducing the lift of the aircraft. Spoilers are commonly operated on the ground to bring the aircraft to rest by dumping the lift and thereby transferring all aircraft weight from the wings to the landing gear to allow mechanical braking. When spoilers are used on the ground, they are sometimes referred to as ground spoilers. The use of spoilers as trailing-vortex-alleviation devices on a transport model was investigated by Croom [37]. The effectiveness of spoilers in suppressing flutter onset for a low-aspect-ratio, rectangular wing was investigated by Coe [38], with a NACA 64A010 airfoil shape. Wentz and Seethram [39] investigated different spoiler back-side shapes to see their effect on performance of the spoiler.

This section contains the literature reviewed concerning the spoiler. Section 2.4.1 discusses the results from experiments on airfoils with a deployed spoiler. Section 2.4.2 discusses the results from computational simulations of the flow around spoilers. Section 2.4.3 presents previous work on flow around flat plates.

### 2.4.1 Spoiler Experimental Studies

The flow field around a spoiler is complex, involving flow separation, reattachment, recirculation bubbles, and vortex shedding. The flow on the suction surface separates upstream of the spoiler hinge line as a result of the adverse pressure gradient created by the presence of the spoiler. The flow then reattaches to the spoiler forming a recirculating bubble above the hinge line sometimes called the 'hinge bubble'. The flow then separates again due to discontinuity in the surface at the tip of the spoiler convecting into the wake as a free shear layer. The flow on the lower airfoil surface also leaves at the trailing edge and convects into the wake. The two separating shear layers form a large reverse flow bubble just downstream of the trailing edge. The wake behind the spoiler is highly turbulent and oscillatory due to the shedding of vortices from the spoiler tip and trailing edge and thus may interact with the tail surface causing buffet.

Lee *et al.* [40] conducted an experimental study of a 2D airfoil with a spoiler. The tests were performed on a Boeing Advanced Transport Research airfoil with chord length of 8 inches (0.2032 m) fitted with a 1.25 inches (0.03175 m) spoiler hinged at 73% chord. The Reynolds number of the test was $2.8 \times 10^5$ based on the chord. Surface pressure distribution, boundary layer and wake profile were measured using a 5-micron single hot-wire. The aims of the experiment were to evaluate the effects of the airfoil incidence and spoiler deflection on the mean and fluctuating quantities of the flow field. The results showed that at low angles of attack and large spoiler deflections, a laminar hinge bubble formed that extended up to 25% of the chord. At high angles of attack, the boundary layer became turbulent and the hinge bubble was smaller.

Bodapati [41] visualised the vortex shedding from an airfoil with a deflected spoiler using Schlieren in order to understand the flow structure. The variation in vortex shedding was found to be random and required a high speed movie to capture the complete process. The Schlieren photographs clearly showed the flow separation at the tip of the spoiler and at the trailing edge of the airfoil forming a recirculation bubble.

### 2.4.2 Spoiler Computational Studies

Despite the complexity of the spoiler-airfoil geometry and the complexity of the flow field, several attempts have been made to simulate the flow around an airfoil with a deployed spoiler. In this area, most of the numerical simulations were interested in the dynamic response of a spoiler. Early attempts at computation of the flow field around a spoiler adopted the discrete vortex method [40] [42].

Kim and Rho [43] performed an investigation of the flow field around an airfoil with a stationary and an oscillating spoiler by solving turbulent 2D compressible Navier-Stokes equations. The model used for the stationary case was based on a Boeing Advance Transport Research airfoil. A spoiler of 15.5% chord length was hinged at 73% chord from the leading edge of the airfoil. The computations were performed at $M_\infty = 0.13$ and $Re = 2.8 \times 10^5$. The spoiler deflection angle was 15°, 30° and 60°, and the airfoil angle of attack was 0°. The calculation was initiated with freestream conditions and continued until periodic vortex shedding was achieved. The non-dimensional time step used was $\Delta tU/C = 0.02$ and second-order time accuracy was preserved using subiterations. Comparison of time-average pressure coefficient at different spoiler angles agreed well with the experiment from reference

[40]. Discrepancies were observed on the suction surface near the trailing edge due to difference in geometry and imperfection of the Baldwin-Lomax turbulence model. The time-average lift decreased and the time-averaged drag increased with an increase in the spoiler deflection. The vortex shedding frequency was found to decrease and the fluctuation amplitude increased with increasing spoiler deflection angle. This is consistent with general bluff body flow in that the vortex shedding frequency is inversely proportional to the width of the wake of the body. They also argue that the spoiler projection height is an appropriate characteristic length of the Strohaul number for the flow than the airfoil chord length. The vortex shedding was found to induce a fluctuating pressure field over the surface of the airfoil. They argue further that the plot of chordwise distribution of peak values of pressure spectra confirms that the shedding frequency can be estimated from the lift history or single point wake velocity measurement. The results clearly show the vortices from the spoiler-tip and the airfoil-trailing edge.

Choi and Chang [44] performed a CFD study of the transient aerodynamic response of an airfoil to a rapidly deploying spoiler using 2D turbulent compressible Navier-Stokes flow model. The spoiler moving relative to the stationary airfoil was treated by an overset grid method. The airfoil used in the study was the ONERA supercritical airfoil (RA16C) used in Reference [45]. A spoiler with chord length 15% of the airfoil chord was hinged at 52% chord from the leading edge of the airfoil. The spoiler was modelled with a sharp trailing edge in contrast with experiment where a finite trailing edge was used. Two cases were considered: a subsonic flow with the conditions $M_\infty = 0.3$, $Re = 1.9 \times 10^6$, $\alpha = 0°$, spoiler at 20° and a transonic flow with $M_\infty = 0.73$, $Re = 4.7 \times 10^6$, $\alpha = 0°$, and spoiler angle at 10°. Due to the unsteady vortex behind the spoiler a time-accurate solution was required. A nondimensional time step $\Delta tU/C = 0.01$ (CFL $\approx$ 1200) was used in the subsonic case and $\Delta tU/C = 0.001$ (CFL $\approx$ 300) was used in the transonic case. The pressure coefficients averaged over a period agreed well with experimental data from reference [45]. Discrepancies were observed at the trailing edge partly because of the imperfection of the turbulence model and partly because of the shape modification of the spoiler trailing edge. The fluid-dynamic mechanism of the adverse lift and the effect of spoiler deploying rate on the unsteady airfoil characteristics was analysed. The adverse lift caused by the spoiler vortex was capture very well. The maximum adverse lift occured when the reattachment point of the separation bubble just reached the trailing edge of the airfoil. Increasing the spoiler deploying rate initially elevated the adverse lift then followed by a decrease in adverse lift afterwards.

### 2.4.3 Flow around Flat Plate

There has been a lot of research into methods of reducing or eliminating vortex shedding from bluff bodies. The following is a review of the relevant literature on the reduction of vortex shedding from flat plates. De Bray [46] performed tests in a low speed wind tunnel on perforated square flat plates aimed at measuring the effects of perforations on the drag and velocity fluctuations downstream of a square plate. Measurements of drag were carried out using a capacity-type drag balance. In addition, hot-wire measurements were performed of the longitudinal velocity fluctuations in a plane behind the perforated plate. He found that perforating the plate gave substantial reductions in the level of velocity fluctuations, at the expense of comparatively small reductions in drag coefficient.

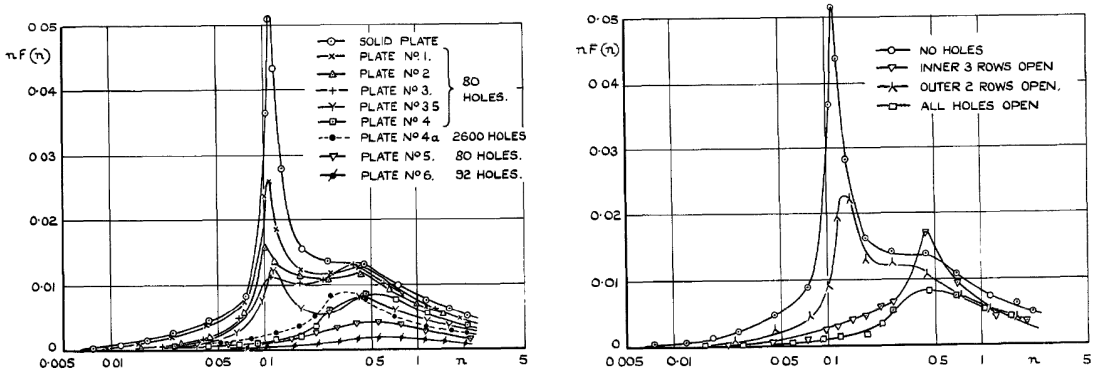


(a) Uniform perforated plate [46].

(b) Partly perforated plate[46].

FIGURE 2.7

Figure 2.7 shows the power spectral density of the velocity fluctuations behind uniformly perforated plates and partly perforated plates. The non-dimensional frequency $n = \frac{fl}{U}$ i.e. equivalent to the Strouhal number and $nF(n)$ is the power spectral density magnitude. The peak at non-dimensional frequency $n = 0.115$ corresponds to the vortex shedding frequency behind the solid plate. The plate number divided by 10 is equivalent to the plate porosity, e.g. plate no. 2 has a porosity of 0.2 and plate no. 3.5 has a porosity of 0.35 and so on. Figure 2.7 shows that an increase in the porosity (free area ratio) gave a progressive reduction in the peak velocity fluctuations at $n = 0.115$. For uniform perforated plates with porosity below 0.35, the shedding frequency remained at $n = 0.115$. For uniformly perforated plates with porosity higher than 0.35, the peak disappeared. The flow behind the perforated plates can therefore be divided into two flow regimes: for porosity lower than 0.35, where vortex shedding is present and reduces with increase porosity; and for porosity higher than 0.35, where vortex shedding is

completely suppressed.

Figure 2.7(a) shows that a uniform perforated plate with a free area ratio of 0.40 gave a reduction in the low-frequency component of velocity fluctuations of 30% of that for a solid plate. This was accompanied by a loss in drag coefficient of less than 20%. Increasing the free area ratio beyond 0.40 incurred a further reduction in the drag coefficient. Perforating only the central portion of the plate produced the best results (Figure 2.7(b)). A centrally perforated plate with an area ratio of 0.20 reduced the low frequency velocity fluctuations by the same amount as a uniformly perforated plate of an area ratio of 0.40. The perforated plate of 40% porosity induced a 6% increase in drag coefficient. Perforating only near the edges was found to be less effective than uniform perforations in terms of both drag performance and reduction of velocity fluctuations.

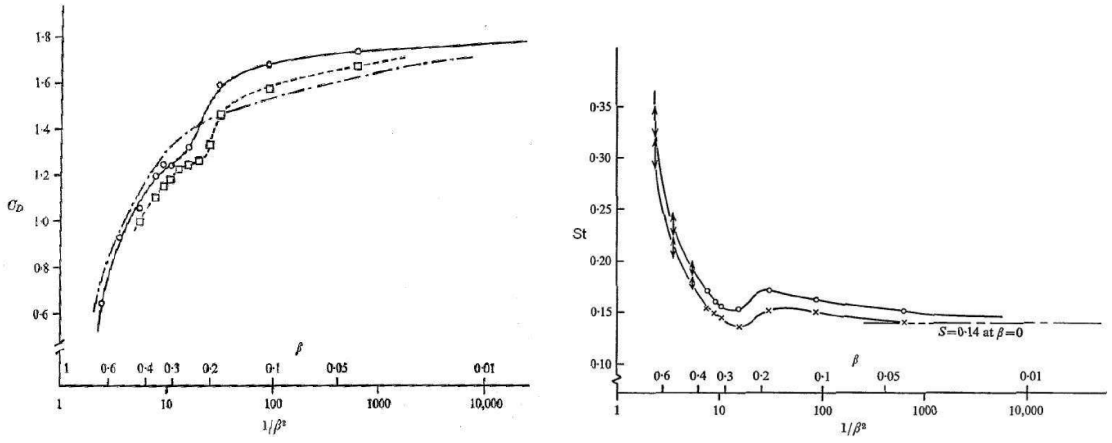


(a) Drag coefficient $C_D$ plot.

(b) Strouhal number $St$ plot.

FIGURE 2.8: Perforated plate drag coefficient $C_D$ and Strouhal number $St$ variation with porosity(free area ratio)

Castro [47] measured the drag of perforated plates of different porosities placed normal to an air stream. Measurements of drag and shedding frequency were made in the Reynolds number range $2.5 \times 10^4 < Re < 9.0 \times 10^4$. A wake transverse and drag balance was used to measure the drag and a hot-wire was used to measure the vortex shedding frequency. Figure 2.8(a) shows a plot of drag coefficient against perforated plate porosity(free area ratio). The drag coefficient reduced with increasing porosity.

A plot of the shedding frequency against perforated plate porosity is shown in Figure 2.8(a). The frequency is non-dimensionalised by the plate chord length and the freestream velocity. As the porosity increases there is a gradual increase in Strouhal number up to a porosity equal to 0.2, where an abrupt reversal of slope occurs. Similar abrupt changes in the drag coefficient can be seen in Figure 2.8(b),

with a sudden drop in drag at a porosity equal to 0.20. The sudden change in drag and Strouhal number corresponds to the elimination of vortex shedding. Castro argued that the porosity of 0.20 is a critical point at which there is just enough bleed air through the holes to prevent the shear layers that separated from the top and bottom edges from interacting to form a vortex street. This is in agreement with the findings of de Bray [46], that showed the flow around perforated plates can be divided into two flow regimes, where shedding occurs and where shedding is suppressed. The above work clearly demonstrates that perforation can be used to reduce or eliminate vortex shedding behind a flat plate or spoiler.rs. Similar abrupt changes in the drag coefficient can be seen in Figure 2.8(b), with a sudden drop in drag at a porosity equal to 0.20. The sudden change in drag and Strouhal number corresponds to the elimination of vortex shedding. Castro argued that the porosity of 0.20 is a critical point at which there is just enough bleed air through the holes to prevent the shear layers that separated from the top and bottom edges from interacting to form a vortex street. This is in agreement with the findings of de Bray [46], that showed the flow around perforated plates can be divided into two flow regimes, where shedding occurs and where shedding is suppressed. The above work clearly demonstrates that perforation can be used to reduce or eliminate vortex shedding behind a flat plate or spoiler.

## 2.5 Summary

The main contributions to airframe noise during approach to landing have been identified as the landing gear and high-lift devices. A review pertaining to the noise from high-lift devices has been conducted. The main noise sources are from the slat and the flap. The detail of the noise generation mechanisms have been presented. Furthermore the noise reduction treatments applied to the noise from the high-lift devices have been discussed. The literature review has revealed the lack of studies of the aeroacoustics of the spoiler. None of the studies reviewed have attempted to unravel the details of noise generation from a deployed spoiler. The current study aims to provide an understanding of the noise generation mechanisms when the spoiler is deployed on a high-lift wing.

In the current study the hybrid computational approach is used to compute the far-field noise. In this approach the noise generation and propagation are uncoupled. A CFD solver is used to compute an unsteady flow field which is used as noise source input to an acoustic solver. A review of the literature on the

computational methods used in the study of aerodynamically generated noise has been performed. The computational methods are ranked according to the level of modeling used. The increase in computational cost is related to the decrease in the level of modeling applied. The best methods are those that offer a high level of modeling and a low level of computational cost. From the discussion in this chapter the computational method that achieves this balance are the URANS and the DES methods. DES employs modeling of the small scale turbulent structures, whereas the large scale structures in the separated regions are resolved explicitly. The next chapter discusses the details of the numerical schemes employed in the current study.

# Chapter 3

# Numerical Methods

This chapter presents the computational methodology, including the governing equations, turbulence models and boundary conditions for the CFD and CAA solvers. A high-order accurate CAA code SotonCAA is used to simulate the flow around the HLDs. In addition, a low-order commercial CFD solver is employed to simulate flow around 3D geometries.

## 3.1 Computational Aeroacoustics

Computational Aeroacoustics (CAA) involves the use of numerical techniques in the computation of sound generation and propagation in air from the fundamental governing equations. The numerical modeling of aeroacoustics is very different from standard computational fluid dynamics computations. CAA must overcome several important computational challenges [48]:

- Aeroacoustic problems involve the resolution of a very wide frequency range. Numerical resolution of the high frequency waves with extremely short wavelength becomes a formidable obstacle requiring very fine grids and accurate high-order numerical schemes.
- The length scales of the noise generating turbulent structures are usually very different from the acoustic wavelength. There is a very large disparity between the length scale of the near-field region and that of the acoustic far-field region. CAA methods must be designed to deal with problems with greatly varying length scales in different parts of the computational domain.

- The small amplitude of the acoustic waves compared with the mean flow quantities coupled with the long propagation distances, means accurate numerical simulation of sound waves propagation requires numerical schemes with very low dissipation and dispersion errors. The dissipation and dispersion properties of low order traditional CFD numerical schemes tend to dampen the acoustic oscillations and may sometimes generate artificial disturbances. This leads to the use of high-order-accurate numerical methods, in particular compact and optimized finite difference schemes for the spatial discretisation and low dispersion low dissipation Runge-Kutta time marching schemes coupled with non-reflection boundary conditions.

- Proper choice of boundary conditions to avoid the reflection of outgoing sound waves back into the computational domain, and thus contaminate the numerical solution. Radiation boundary conditions are often imposed at the artificial exterior boundaries to assist the waves in exiting the computational domain smoothly. Such boundary conditions are not required for CFD.

The best choice of discretisation for a given geometry and accuracy requirement is the one that is most computationally efficient, i.e. requires the smallest computing time for a given error tolerance. The choice of discretisation is also influenced by the ease of implementation of boundary conditions, efficiency of parallelisation, memory requirements and the potential for straightforward implementation for different geometries and flow conditions. Finite difference schemes satisfy most of the above requirements and therefore have evolved as the standard for computational aeroacoustics. Furthermore, the finite difference schemes can be easily extended to higher-order-accuracy.

There are two well known approaches used to model aeroacoustic problems. These are the direct approach and the hybrid approach.

In the direct computational approach, the full compressible Navier-Stokes equations describing the flow field, the aerodynamically generated acoustic field and the propagation of the sound are solved directly in one computation. Thus in the flow simulation both the energy containing eddies range and the dissipative eddies range of scales are resolved. This requires very high numerical resolution due to the wide range of length and time scales present between the acoustic variables and the flow variables. As a result it is very computationally expensive and unsuitable for most practical engineering applications. The Reynolds numbers of the computed flows using DNS are relatively small, however they are rapidly

increasing due to increases in computational power and resources. DNS provides benchmark databases to test and develop models of unsteady flow and their sound generation mechanisms.

Due to the high computational demands of direct computation of noise, hybrid approaches have been developed and have become popular due to the reduction in computational resource demands it offers. In these approaches the computational domain is divided into two different regions such that the governing acoustic and flow field equations are solved separately. The near field sound generation process is therefore separated from the sound propagation to the far-field. This involves using two different numerical solvers, a CFD solver is used to compute the near flow field and then an acoustic solver, using integral methods such as the FW-H equation, is used to compute the propagation of noise to the far-field. The hybrid approach is based on the fundamental assumption that the sound is generated by inhomogeneities in the flow field, but the flow field itself is not influenced by the acoustic field. The accuracy requirements of the hybrid approach are far less than those of the direct computational approach, since only the flow inhomogeneities need to be resolved rather than the propagation of the small acoustic waves. However, the far-field noise is very dependent on the accurate resolution of the near-field unsteady flow. This is in turn dependent on how well the effects of turbulence are resolved or modeled.

## 3.2 High-Order CFD Solver

SotonCAA is a high-order accurate compact finite difference solver. The code is a multi block Navier-Stokes solver for structured grids. It is based on high-order compact finite difference schemes that offer up to 4th-order accuracy in space and time. The code is capable of simulating flow around complex geometry since the governing equation are solved in generalised coordinates in multi-block form. To allow efficient communication between connected blocks, the code is parallelized using Message Passing Interface (MPI).

This Chapter contains details of the governing equations, numerical scheme, turbulence models and boundary conditions employed in SotonCAA. The validation of the SotonCAA is presented in Appendix B.

### 3.2.1 Governing Equations

SotonCAA solves the compressible 3D Navier-Stokes equations in generalised coordinates. In the absence of body forces and external heat addition, the governing equations may be written in generalized coordinates as follows:

$$\frac{\partial \hat{\mathbf{Q}}}{\partial t} + \frac{\partial \hat{\mathbf{F}}}{\partial \xi} + \frac{\partial \hat{\mathbf{G}}}{\partial \eta} + \frac{\partial \hat{\mathbf{H}}}{\partial \zeta} = \frac{M_\infty}{Re_L}\left[\frac{\partial \hat{\mathbf{F}}_v}{\partial \xi} + \frac{\partial \hat{\mathbf{G}}_v}{\partial \eta} + \frac{\partial \hat{\mathbf{H}}_v}{\partial \zeta}\right], \tag{3.1}$$

where $t$ is the time, $\hat{\mathbf{Q}} = (1/J)[\rho, \rho u, \rho v, \rho w, \rho E]^T$ denotes the solution vector of conserved variables and $J = \partial(\xi, \eta, \zeta)/\partial(x, y, z)$ is the coordinates transformation Jacobian. The inviscid fluxes $\hat{\mathbf{F}}$, $\hat{\mathbf{G}}$, $\hat{\mathbf{H}}$ and viscous fluxes $\hat{\mathbf{F}}_v$, $\hat{\mathbf{G}}_v$, $\hat{\mathbf{H}}_v$ are given by

$$\hat{\mathbf{F}} = \frac{1}{J}\begin{bmatrix} \rho U \\ \rho U u + \xi_x p \\ \rho U v + \xi_y p \\ \rho U w + \xi_z p \\ (\rho E + p)U \end{bmatrix}, \qquad \hat{\mathbf{F}}_v = \frac{1}{J}\begin{bmatrix} 0 \\ \xi_x \tau_{xx} + \xi_y \tau_{xy} + \xi_z \tau_{xz} \\ \xi_x \tau_{xy} + \xi_y \tau_{yy} + \xi_z \tau_{yz} \\ \xi_x \tau_{xz} + \xi_y \tau_{yz} + \xi_z \tau_{zz} \\ \xi_x b_x + \xi_y b_y + \xi_z b_z \end{bmatrix}, \tag{3.2}$$

$$\hat{\mathbf{G}} = \frac{1}{J}\begin{bmatrix} \rho V \\ \rho V u + \eta_x p \\ \rho V v + \eta_y p \\ \rho V w + \eta_z p \\ (\rho E + p)V \end{bmatrix}, \qquad \hat{\mathbf{G}}_v = \frac{1}{J}\begin{bmatrix} 0 \\ \eta_x \tau_{xx} + \eta_y \tau_{xy} + \eta_z \tau_{xz} \\ \eta_x \tau_{xy} + \eta_y \tau_{yy} + \eta_z \tau_{yz} \\ \eta_x \tau_{xz} + \eta_y \tau_{yz} + \eta_z \tau_{zz} \\ \eta_x b_x + \eta_y b_y + \eta_z b_z \end{bmatrix}, \tag{3.3}$$

$$\hat{\mathbf{G}} = \frac{1}{J}\begin{bmatrix} \rho W \\ \rho W u + \zeta_x p \\ \rho W v + \zeta_y p \\ \rho W w + \zeta_z p \\ (\rho E + p)W \end{bmatrix}, \qquad \hat{\mathbf{G}}_v = \frac{1}{J}\begin{bmatrix} 0 \\ \zeta_x \tau_{xx} + \zeta_y \tau_{xy} + \zeta_z \tau_{xz} \\ \zeta_x \tau_{xy} + \zeta_y \tau_{yy} + \zeta_z \tau_{yz} \\ \zeta_x \tau_{xz} + \zeta_y \tau_{yz} + \zeta_z \tau_{zz} \\ \zeta_x b_x + \zeta_y b_y + \zeta_z b_z \end{bmatrix}, \tag{3.4}$$

where $\rho, u, v, w, p$ and $E$ are the instantaneous density, cartesian velocity components, static pressure and specific total energy, respectively. The specific

total energy is defined as

$$E = e + \frac{1}{2}\left(u^2 + v^2 + w^2\right), \tag{3.5}$$

where $e$ is the specific internal energy. The pressure is related to the other thermodynamic variables by the equation of state for an ideal gas

$$p = (\gamma - 1)\rho\left(E - \frac{1}{2}\left(u^2 + v^2 + w^2\right)\right), \tag{3.6}$$

where $\gamma = c_p/c_v$ is the ratio of specific heat coefficients under constant pressure and constant volume. The terms $U$, $V$, and $W$ in the inviscid fluxes are the contravariant velocities defined as,

$$\begin{aligned} U &= \xi_x u + \xi_y v + \xi_z w, \\ V &= \eta_x u + \eta_y v + \eta_z w, \\ W &= \zeta_x u + \zeta_y v + \zeta_z w. \end{aligned} \tag{3.7}$$

The viscous stress and the heat flux are defined in tensor notations (summation convection implied) respectively as

$$\tau_{ij} = \mu\left[\left(\frac{\partial u_j}{\partial x_i} + \frac{\partial u_i}{\partial x_j}\right) - \frac{2}{3}\frac{\partial u_k}{\partial x_k}\delta_{ij}\right], \tag{3.8}$$

$$b_j = u_i\tau_{ij} + \frac{1}{(\gamma - 1)}\frac{\mu}{Pr}\frac{\partial T}{\partial x_j}, \tag{3.9}$$

where $\mu$ is the molecular viscosity, $\delta_{ij}$ is the Kronecker delta and $Pr$ is the Prandtl number.

The equations are non-dimensionalised with a reference length $L^*$, freestream density $\rho^*_\infty$, freestream sound speed $c^*_\infty$ and molecular viscosity $\mu^*_\infty$. The superscript notation $()^*$ denotes dimensional reference quantity. Based on the characteristic parameters we define the following non-dimensional quantities of Mach number $M_\infty$, Reynolds number $Re$ and Prandtl number $Pr$ as follows:

$$M_\infty = \frac{|\mathbf{u}^*_\infty|}{c^*_\infty},\ Re_L = \frac{\rho^*_\infty|\mathbf{u}^*_\infty|L^*}{\mu^*_\infty},\ Pr = \frac{c^*_p\mu^*_\infty}{k^*_\infty}, \tag{3.10}$$

where $c^*_p$ is the specific heat coefficient at constant pressure, $k^*_T$ is the thermal conductivity coefficient and $\mathbf{u}^*_\infty$ is the freestream velocity vector.

### 3.2.2 Spatial Discretization

A finite-difference scheme approach is employed to discretise the governing equations. Following [49] the general compact derivative of a function may be written as:

$$[\mathbf{B}]D = \frac{1}{\Delta x}[\mathbf{C}]f, \tag{3.11}$$

where $D$ is the spatial derivative of $f$ and $\mathbf{B}$ is a matrix which can be easily inverted (non-singular) and positive definite. The first-order spatial derivative $(\partial f/\partial \eta)_i$ at a node $i$ is computed in the transformed space by solving the following systems of equations:

$$\alpha_F D^F_{i+1} + \beta_F D^F_i = \frac{a_F f_{i+2} + b_F f_{i+1} + c_F f_i + d_F f_{i-1} + e_F f_{i-2}}{\Delta x}, \tag{3.12}$$

$$\beta_B D^B_i + \gamma_B D^B_{i-1} = \frac{a_B f_{i+2} + b_B f_{i+1} + c_B f_i + d_B f_{i-1} + e_B f_{i-2}}{\Delta x}, \tag{3.13}$$

$$D_i = \frac{1}{2}\left(D^F_i + D^B_i\right), \tag{3.14}$$

where $D_i$, the desired approximation of the spatial derivative, is obtained by summing the forward and backward approximations given by $D^F_i$ and $D^B_i$ respectively. The coefficients $a_F$, $b_F$, $c_F$, etc. determine the spatial properties of the algorithm e.g. the order of accuracy, dispersion and dissipation characteristics and stability.

Hixon [49] first applied the prefactorization procedure to a formally 6th-order compact scheme. Later Ashcroft and Zhang [50] applied prefactorization and optimisation techniques to develop a family of prefactored compact optimised schemes of up to 4th-order accuracy. The schemes are derived by matching the coefficient of the forward and backwards stencils to either 6th- or 8th-order accurate compact schemes. The procedure produces a set of equations which must be solved in order to determine the schemes coefficients. Due to the quadratic terms in one of the equations, the coefficients are not uniquely determined by the system of equations alone. Therefore, the coefficients are chosen which minimise the propagation of errors from the computational boundaries.

Following Kim and Lee [51], the schemes are optimised by minimising the integrated error which consists of a weighting function. The application of this procedure to the formally 8th-order compact scheme leads to the optimized

TABLE 3.1: Central coefficients for 4th-order Optimised prefactored scheme of Ashcroft and Zhang.

| Coefficient | Values |
|---|---|
| $\alpha_F$ | 0.364692465 |
| $\beta_F$ | 0.683373548 |
| $\gamma_F$ | 0.0 |
| $a_F$ | 0.0 |
| $b_F$ | 0.801891884 |
| $c_F$ | -0.538991333 |
| $d_F$ | -0.279626973 |
| $e_F$ | 0.016726422 |

prefactored scheme defined by the coefficients in Table 3.1.

The optimised prefactored scheme derived from the 8th-order compact scheme requires a five-point stencil while the scheme derived from the formally 6th-order compact scheme only requires a three-point stencil. Both schemes result in reducing the tridiagonal matrix system of the compact scheme to two bi-diagonal matrix system.

For a computational domain consisting of $N$ points, the five-point stencil fourth-order scheme can be applied from $j = 3$ to $j = N - 2$. At and near the domain boundaries it is therefore necessary to employ additional expressions. These boundary stencils are also required along inter-block boundaries in multi-block calculations. For the five-point stencil fourth-order scheme, the boundary stencils are required at nodes $j = 1$, $j = 2$, $j = N - 1$ and $j = N$. The coefficients of the biased explicit stencils used at these points have been obtained by matching the Taylor series expansions of the explicit stencils to those of the interior forward and backward derivative operators to third-order. The resulting boundary stencils for $j = 2$ and $j = N - 1$ are given by:

$$D_2^B = \frac{1}{\Delta x}\sum_{j=1}^{4} s_j f_j \qquad\qquad D_{N-1}^B = \frac{1}{\Delta x}\sum_{j=N-3}^{N} e_j f_j, \tag{3.15}$$

and the forward stencil is given as:

$$D_2^F = \frac{1}{\Delta x}\sum_{j=1}^{4} -e_{N+1-j} f_j \qquad\qquad D_{N-1}^F = \frac{1}{\Delta x}\sum_{j=N-3}^{N} -s_{N+1-j} f_j, \tag{3.16}$$

TABLE 3.2: Boundary coefficients for nodes $j = 2$ and $j = N - 1$.

| Coefficient | Value | Coefficient | Value |
|---|---|---|---|
| $s_1$ | -0.266441396584756 | $e_N$ | 0.40022527008191 |
| $s_2$ | -0.633783873497153 | $e_{N-1}$ | 0.3662161265028 |
| $s_3$ | 1.0668919367485766 | $e_{N-2}$ | -0.9331080632514 |
| $s_4$ | -0.16666666666666 | $e_{N-3}$ | 0.1666666666666 |

where the coefficients are given in Table 3.2. At the actual boundary point $j = 1$ and $j = N$, the following third-order explicit stencil is used:

$$D_1 = \frac{1}{\Delta x} \sum_{j=1}^{4} c_j f_j \qquad\qquad D_N = \frac{1}{\Delta x} \sum_{j=N-3}^{N} -c_{N+1-j} f_j, \tag{3.17}$$

where $c_1 = -33/18$, $c_2 = 3$, $c_3 = -3/2$ and $c_4 = 1/3$.

In this work the 4th-order five-point stencil optimised prefactored scheme of Ashcroft and Zhang [50] is employed for spatial discretisation. At each time step, the derivatives of the inviscid fluxes are obtained by first forming the fluxes at the nodes and subsequently differentiating each component using the equations above. For computation of the viscous terms, the primitive variables $u$, $v$, $w$ and $c$ are first differentiated to form the components of the stress tensor (Equation 3.8) and the heat flux vector (Equation 3.9) at each node. The viscous flux derivatives are then computed by a second application of the same scheme.

### 3.2.3 Filtering Scheme

The compact finite difference schemes described in the previous section are nondissipative and therefore susceptible to numerical instabilities due to the growth of high-frequency modes. Such modes originate from mesh nonuniformity, boundary conditions, nonlinear flow features or poorly specified initial conditions. In order to overcome these difficulties and extend the flow solver to practical problems, while retaining the improved accuracy of the spatial compact discretization, a high-order implicit filtering is used. In this work the implicit filters of Visbal and Gaitonde[52] are used.

If the components of the solution are denoted by $f$, filtered values $\hat{f}$ are obtained

by solving the tridiagonal system

$$\alpha_f \hat{f}_{i-1} + \hat{f}_i + \alpha_f \hat{f}_{i+1} = \sum_{n=0}^{N} \frac{a_n}{2} \left( \hat{f}_{i+1} + \hat{f}_{i-1} \right), \tag{3.18}$$

where the coefficients $\alpha_f$, $a_0$, $a_1$,..., $a_N$ determine the order and spectral response of the filter. Equation (3.18) provides a $2N$th order formula on a $2N+1$ point stencil depending on the choices of the coefficients. The $N+1$ coefficients, $a_0$, $a_1$,....$a_N$, are derived in terms of $\alpha_f$ with Taylor-and-Fourier-series analyses. The adjustable parameter $\alpha_f$ satisfies the inequality $-0.5 < \alpha_f \leq 0.5$, with higher values of $\alpha_f$ corresponding to a less dissipative filter. Extensive numerical experience suggests that regardless of time-integration scheme, values of $\alpha_f$ between 0.3 and 0.5 are appropriate. However, in extremely poor quality meshes a lower value of $\alpha_f \approx 0.1$ may suffice. The filter is typically chosen to be at least two orders of accuracy higher than the difference scheme.

In the work presented in this report the 8th-order filter has been used, with $\alpha_f = 0.495$. This choice ensures the spectral characteristics of the filter closely match those of the spatial compact discretization thus preserving the scheme accuracy. The eighth-order filter requires a nine point stencil, therefore it is not suitable for use at and near boundary points. Therefore special formulae are required at point $j = 1$ to $j = 5$ and at $j = N - 4$ to $j = N$. Following Visbal and Gaitonde [52], in these regions the order of accuracy of the filter is reduced as the boundary is approached to the level for which a centered filter scheme is available. Values along the boundary are left unfiltered. The filter is applied in all coordinate directions to the primitive variables after every sub-iteration.

### 3.2.4 Time Integration Scheme

For most wall bounded viscous flow which demands the use of extremely fine resolution, the stability constraint of the explicit time-marching scheme is very restrictive and inefficient. Therefore in this work, the implicit lower-upper approximate factorization algorithm employing Newton-like sub iterations is used for time integration. The scheme is second order in time.

Second order accuracy is achieved by reducing errors due to explicit boundary conditions, factorization and linearization using Newton-like sub iterations. This is achieved by introducing a pseudo-time $\tau$ to the governing equations and the

resulting equations can written as:

$$\frac{\partial \hat{\mathbf{Q}}}{\partial \tau} + \frac{\partial \hat{\mathbf{Q}}}{\partial t} + \left( \frac{\partial \hat{\mathbf{F}}}{\partial \xi} + \frac{\partial \hat{\mathbf{G}}}{\partial \eta} + \frac{\partial \hat{\mathbf{H}}}{\partial \zeta} \right) = \frac{M_\infty}{Re_L} \left[ \frac{\partial \hat{\mathbf{F}}_v}{\partial \xi} + \frac{\partial \hat{\mathbf{G}}_v}{\partial \eta} + \frac{\partial \hat{\mathbf{H}}_v}{\partial \zeta} \right] = \mathbf{R}\left(\hat{\mathbf{Q}}\right). \tag{3.19}$$

Discretizing the pseudo-time using first-order backward difference and discretizing the physical time using a second-order central difference, Equation 3.19 becomes

$$\frac{\hat{\mathbf{Q}}^{m-1} - \hat{\mathbf{Q}}^{m}}{\Delta \tau} + \frac{3\hat{\mathbf{Q}}^{m+1} - 4\hat{\mathbf{Q}}^{n} + \hat{\mathbf{Q}}^{n-1}}{2\Delta t} + \left( \frac{\partial \hat{\mathbf{F}}}{\partial \xi} + \frac{\partial \hat{\mathbf{G}}}{\partial \eta} + \frac{\partial \hat{\mathbf{H}}}{\partial \zeta} \right)^{m} = \mathbf{R}\left(\hat{\mathbf{Q}}\right)^{m}, \tag{3.20}$$

where $n$ and $m$ denote the main time step level and the sub-iterative time level. Equation 3.20 can be rewritten as follows:

$$\begin{aligned} &\frac{\hat{\mathbf{Q}}^{m+1} - \hat{\mathbf{Q}}^{m}}{\Delta \tau} + \frac{3\left(\hat{\mathbf{Q}}^{m+1} - \hat{\mathbf{Q}}^{m}\right) + 3\hat{\mathbf{Q}}^{m} - 4\hat{\mathbf{Q}}^{n} + \hat{\mathbf{Q}}^{n-1}}{2\Delta t} \\ &+ \left( \frac{\partial \hat{\mathbf{F}}}{\partial \xi} + \frac{\partial \hat{\mathbf{G}}}{\partial \eta} + \frac{\partial \hat{\mathbf{H}}}{\partial \zeta} \right)^{m} = \frac{M_\infty}{Re_L} \left[ \frac{\partial \hat{\mathbf{F}}_v}{\partial \xi} + \frac{\partial \hat{\mathbf{G}}_v}{\partial \eta} + \frac{\partial \hat{\mathbf{H}}_v}{\partial \zeta} \right]^{m}. \end{aligned} \tag{3.21}$$

The convective fluxes $\hat{\mathbf{F}}$, $\hat{\mathbf{G}}$ and $\hat{\mathbf{H}}$ are linearized about the time level $m$. After neglecting term of second and higher order are obtained as follows:

$$\hat{\mathbf{F}}^{m+1} = \hat{\mathbf{F}}^{m} + \left( \frac{\partial \hat{\mathbf{F}}}{\partial \hat{\mathbf{Q}}} \right)^{m} \Delta \hat{\mathbf{Q}}, \tag{3.22}$$

$$\hat{\mathbf{G}}^{m+1} = \hat{\mathbf{G}}^{m} + \left( \frac{\partial \hat{\mathbf{G}}}{\partial \hat{\mathbf{Q}}} \right)^{m} \Delta \hat{\mathbf{Q}}, \tag{3.23}$$

$$\hat{\mathbf{H}}^{m+1} = \hat{\mathbf{H}}^{m} + \left( \frac{\partial \hat{\mathbf{H}}}{\partial \hat{\mathbf{Q}}} \right)^{m} \Delta \hat{\mathbf{Q}}. \tag{3.24}$$

Let $A$, $B$, $C$ be the Jacobian matrices of the convective fluxes, so that

$$\mathbf{A} = \left( \frac{\partial \hat{\mathbf{F}}}{\partial \hat{\mathbf{Q}}} \right), \tag{3.25}$$

$$\mathbf{B} = \left( \frac{\partial \hat{\mathbf{G}}}{\partial \hat{\mathbf{Q}}} \right), \tag{3.26}$$

$$\mathbf{C} = \left( \frac{\partial \hat{\mathbf{H}}}{\partial \hat{\mathbf{Q}}} \right). \tag{3.27}$$

Substituting the jacobians back into Equation 3.21 and expressing the equation in

delta form we obtain:

$$\left[\left(\frac{1}{\Delta\tau}+\frac{3}{2}\frac{1}{\Delta t}\right)I+\delta_\xi\mathbf{A}+\delta_\eta\mathbf{B}+\delta_\zeta\mathbf{C}\right]\Delta\hat{\mathbf{Q}}^m = -\frac{3\hat{\mathbf{Q}}^m-4\hat{\mathbf{Q}}^n+\hat{\mathbf{Q}}^{n-1}}{2\Delta t} - \left(\frac{\partial\hat{\mathbf{F}}}{\partial\xi}+\frac{\partial\hat{\mathbf{G}}}{\partial\eta}+\frac{\partial\hat{\mathbf{H}}}{\partial\zeta}\right)^m + \frac{M_\infty}{Re_L}\left[\frac{\partial\hat{\mathbf{F}}_v}{\partial\xi}+\frac{\partial\hat{\mathbf{G}}_v}{\partial\eta}+\frac{\partial\hat{\mathbf{H}}_v}{\partial\zeta}\right]^m, \tag{3.28}$$

where $\Delta\hat{\mathbf{Q}}^m = \hat{\mathbf{Q}}^{m+1} - \hat{\mathbf{Q}}^m$. The spatial operators along the $i-$, $j-$, and $k-$ coordinate directions are denoted by $\delta_\xi$, $\delta_\eta$, and $\delta_\zeta$ respectively. Applying Newton-like sub iterations to the pseudo-time system, by setting $\Delta\tau \to \infty$ in Equation 3.28 above yields:

$$\left[\frac{3}{2}I+\Delta t\left(\delta_\xi\mathbf{A}+\delta_\eta\mathbf{B}+\delta_\zeta\mathbf{C}\right)\right]\Delta\hat{\mathbf{Q}}^m = -\frac{3\hat{\mathbf{Q}}^m-4\hat{\mathbf{Q}}^n+\hat{\mathbf{Q}}^{n-1}}{2} - \Delta t\left(\frac{\partial\hat{\mathbf{F}}}{\partial\xi}+\frac{\partial\hat{\mathbf{G}}}{\partial\eta}+\frac{\partial\hat{\mathbf{H}}}{\partial\zeta}\right)^m + \Delta t\frac{M_\infty}{Re_L}\left[\frac{\partial\hat{\mathbf{F}}_v}{\partial\xi}+\frac{\partial\hat{\mathbf{G}}_v}{\partial\eta}+\frac{\partial\hat{\mathbf{H}}_v}{\partial\zeta}\right]^m. \tag{3.29}$$

Following Yoon and Jameson [53], applying the lower-upper approximate factorization method Equation (3.29) may be represented as follows:

$$\left(\mathbf{L}+\mathbf{D}\right)\mathbf{D}^{-1}\left(\mathbf{D}+\mathbf{U}\right)\Delta\hat{\mathbf{Q}}^m = -\frac{3\hat{\mathbf{Q}}^m-4\hat{\mathbf{Q}}^n+\hat{\mathbf{Q}}^{n-1}}{2} - \Delta t D_{\xi 6}\left(\hat{\mathbf{F}}^m-\frac{M_\infty}{Re_L}\hat{\mathbf{F}}_v^m\right) - \Delta t D_{\eta 6}\left(\hat{\mathbf{G}}^m-\frac{M_\infty}{Re_L}\hat{\mathbf{G}}_v^m\right) - \Delta t D_{\zeta 6}\left(\hat{\mathbf{H}}^m-\frac{M_\infty}{Re_L}\hat{\mathbf{H}}_v^m\right). \tag{3.30}$$

In Equation 3.30, the spatial derivatives in the implicit operators (left-hand side) are represented using a standard second order centered approximation whereas the spatial derivatives in the explicit operators (right-hand side) are represented

using a 6th-order Hixon compact scheme [49]. The $D_{\xi 6}$, $D_{\eta 6}$ and $D_{\zeta 6}$ represent the 6th-order difference in the $\xi$, $\eta$ and $\zeta$ directions respectively. Errors due to linearization, factorization and explicit implementation of boundary conditions are eliminated through the use of sub iterations. Three to five sub iterations per time step is suitable for flow calculation as shown by Visbal and Gaitonde [52].

In Equation (3.30), $\Delta\hat{\mathbf{Q}}^{m} = \hat{\mathbf{Q}}^{m+1} - \hat{\mathbf{Q}}^{m}$ where $\hat{\mathbf{Q}}^{m+1}$ is the $m+1$ subiteration to approximate $\hat{\mathbf{Q}}$ at $n+1$ time level. The initial values of the sub iterations are taken as $\hat{\mathbf{Q}}^{m} = \hat{\mathbf{Q}}^{n}$ at time level $n$, and starting from $m = 1$, the sequence of iteration $\hat{\mathbf{Q}}^{m}$, $m = 1, 2, 3...$ converges to $\hat{\mathbf{Q}}^{n+1}$ when the right-hand side unsteady residual equal to zero. The other terms in Equation (3.30) are as follows:

$$\begin{aligned} \mathbf{L} &= -\Delta t \left( \hat{\mathbf{A}}^{+}_{i-1,j,k} + \hat{\mathbf{B}}^{+}_{i,j-1,k} + \hat{\mathbf{C}}^{+}_{i,j,k-1} \right), \\ \mathbf{D} &= \left[ 3/2 + \Delta t \left( r_{\hat{\mathbf{A}}} + r_{\hat{\mathbf{B}}} + r_{\hat{\mathbf{C}}} \right) \right] \mathbf{I}, \\ \mathbf{U} &= \Delta t \left( \hat{\mathbf{A}}^{-}_{i+1,j,k} + \hat{\mathbf{B}}^{-}_{i,j+1,k} + \hat{\mathbf{C}}^{-}_{i,j,k+1} \right), \end{aligned} \tag{3.31}$$

where the flux Jacobian matrices $\hat{\mathbf{A}}$, $\hat{\mathbf{B}}$ and $\hat{\mathbf{C}}$ are given by

$$\begin{aligned} \hat{\mathbf{A}} &= \hat{\mathbf{A}}^{+} + \hat{\mathbf{A}}^{-}, \\ \hat{\mathbf{B}} &= \hat{\mathbf{B}}^{+} + \hat{\mathbf{B}}^{-}, \\ \hat{\mathbf{C}} &= \hat{\mathbf{C}}^{+} + \hat{\mathbf{C}}^{-}, \end{aligned} \tag{3.32}$$

where

$$\begin{aligned} \hat{\mathbf{A}}^{\pm} &= \frac{\hat{\mathbf{A}} \pm r_{\hat{\mathbf{A}}} \hat{\mathbf{I}}}{2}, \\ \hat{\mathbf{B}}^{\pm} &= \frac{\hat{\mathbf{B}} \pm r_{\hat{\mathbf{B}}} \hat{\mathbf{I}}}{2}, \\ \hat{\mathbf{C}}^{\pm} &= \frac{\hat{\mathbf{C}} \pm r_{\hat{\mathbf{C}}} \hat{\mathbf{I}}}{2}, \end{aligned} \tag{3.33}$$

and

$$\begin{aligned} r_{\hat{\mathbf{A}}} &= \max\left( |\lambda_{\hat{\mathbf{A}}}| \right), \\ r_{\hat{\mathbf{B}}} &= \max\left( |\lambda_{\hat{\mathbf{B}}}| \right), \\ r_{\hat{\mathbf{C}}} &= \max\left( |\lambda_{\hat{\mathbf{C}}}| \right), \end{aligned} \tag{3.34}$$

where $\lambda_{\hat{\mathbf{A}}}$, $\lambda_{\hat{\mathbf{B}}}$ and $\lambda_{\hat{\mathbf{C}}}$ are the eigenvalues of the flux Jacobian matrices $\hat{\mathbf{A}}$, $\hat{\mathbf{B}}$ and $\hat{\mathbf{C}}$ respectively. The flux Jacobian matrices are calculated from their cartesian

counterparts by

$$\begin{aligned}\hat{\mathbf{A}} &= \xi_x\mathbf{A} + \xi_y\mathbf{B} + \xi_z\mathbf{C},\\ \hat{\mathbf{B}} &= \eta_x\mathbf{A} + \eta_y\mathbf{B} + \eta_z\mathbf{C},\\ \hat{\mathbf{C}} &= \zeta_x\mathbf{A} + \zeta_y\mathbf{B} + \zeta_z\mathbf{C},\end{aligned} \tag{3.35}$$

where

$$\mathbf{A} = \begin{bmatrix} 0 & 1 & 0 & 0 & 0 \\ -u^2 + \frac{\gamma-1}{2}V^2 & (3-\gamma)u & (1-\gamma)v & (1-\gamma)w & \gamma-1 \\ -uv & v & u & 0 & 0 \\ -wu & w & 0 & u & 0 \\ -\gamma eu + u(\gamma-1)V^2 & \gamma e - \frac{\gamma-1}{2}(2u^2+V^2) & (1-\gamma)uv & (1-\gamma)uw & \gamma u \end{bmatrix}, \tag{3.36}$$

$$\mathbf{B} = \begin{bmatrix} 0 & 0 & 1 & 0 & 0 \\ -uv & v & u & 0 & 0 \\ -u^2 + \frac{\gamma-1}{2}V^2 & (1-\gamma)v & (3-\gamma)u & (1-\gamma)w & \gamma-1 \\ -wv & 0 & w & v & 0 \\ -\gamma ev + v(\gamma-1)V^2 & (1-\gamma)uv & \gamma e - \frac{\gamma-1}{2}(2v^2+V^2) & (1-\gamma)uw & \gamma v \end{bmatrix}, \tag{3.37}$$

$$\mathbf{B} = \begin{bmatrix} 0 & 0 & 0 & 1 & 0 \\ -uw & w & 0 & u & 0 \\ -vw & 0 & w & v & 0 \\ -w^2 + \frac{\gamma-1}{2}V^2 & (1-\gamma)u & (1-\gamma)v & (3-\gamma)w & \gamma-1 \\ -\gamma ew + w(\gamma-1)V^2 & (1-\gamma)uw & (1-\gamma)vw & \gamma e - \frac{\gamma-1}{2}(2w^2+V^2) & \gamma w \end{bmatrix}, \tag{3.38}$$

and $V^2 = u^2+v^2+w^2$. The eigenvalues of $\hat{\mathbf{A}}$ are $U$, $U$, $U$, $U+c\sqrt{\xi_x^2+\xi_y^2+\xi_z^2}$, and $U-c\sqrt{\xi_x^2+\xi_y^2+\xi_z^2}$; the eigenvalues of $\hat{\mathbf{B}}$ are $U$, $U$, $U$, $U+c\sqrt{\eta_x^2+\eta_y^2+\eta_z^2}$, and $U-c\sqrt{\eta_x^2+\eta_y^2+\eta_z^2}$; and the eigenvalues of $\hat{\mathbf{C}}$ are $U$, $U$, $U$, $U+c\sqrt{\zeta_x^2+\zeta_y^2+\zeta_z^2}$, and $U-c\sqrt{\zeta_x^2+\zeta_y^2+\zeta_z^2}$.

### 3.2.5 Turbulence Modeling

Several computational methods are available to calculate the near flow field, depending on the methods used to model the effects of turbulence. In order of increasing level of explicit resolution of turbulent structures, turbulence models can be divided into three groups:

#### URANS

The time-dependent flow governing equations are time-averaged and turbulence models are used for closure. Thus all the turbulence length scales are modelled by the turbulence model used. The turbulence models used range from the one-equation Spalart-Allmaras[54], the two-equations $k-\epsilon$ and $k-\omega$ models to the 6-equations Reynolds Stress Models (RSM). Menter [55] developed a model, the Shear Stress Transport (SST) $k-\omega$, that represented a blend of the $k-\epsilon$ and $k-\omega$ models, and included a shear stress transport term that improved the model's performance for adverse pressure gradient wall-bounded flows. The flow field around high lift devices has been computed using steady Reynolds-Averaged Navier-Stokes (RANS)[56] and unsteady RANS [15] [57] [16].

#### Hybrid RANS/LES or Detached Eddy Simulation (DES)

In this approach the flow is divided into two main regions; the RANS region ,which is close to the wall consisting of the boundary layer, and the LES region, which contains vorticity and turbulence at some point in the simulation such as the wake. The grid resolution requirements in the two regions are very different. In the RANS region close to the wall, the length scale is $d$ (the distance to the nearest wall) as in S-A model. Hence the grid is usually stretched in the flow direction and refined in the wall normal direction. In order to resolve the boundary layer, $y^+$ should be less than 2 (ideally $y^+ \approx 1$) and a grid stretching ratio of 1.25 in the wall normal direction [58]. In the LES region the length scale is the largest of the grid spacing. Therefore the grid spacing ideally needs to be the same in all three directions, thus resulting in cubic cells. DES is commonly based on the S-A turbulence model and offers a practical alternative to the more expensive LES for predicting the flow around the high-Reynolds number high-lift system. The flow field around the high lift devices has been computed using DES by Terracol *et al.* [59].

**Large Eddy Simulation**

In this approach only the large eddies are explicitly resolved in a time-dependent simulation, whereas the small eddies are modelled by a Sub-Grid Scale (SGS) model. Thus the error introduced by modelling all the turbulent length scales can be significantly reduced. The most commonly used SGS model is the Dynamic Smagorinsky model. In the Dynamic Smagorinsky subgrid model, the constant is dynamically computed based on information provided by the resolved length scales thus eliminates the need for users to specify the constant in advance. Filtering of the governing equations is performed to remove the small scale eddies by using the mesh size. This approach therefore places significant emphasis on the grid resolution. As a result, LES requires significantly more computational resources compared to URANS. The flow field around the HLDs has been computed using LES by Wang [60], Manoha *et al.* [61] and Kim *et al.* [43].

The turbulence models implemented in SotonCAA include S-A, DES(based on S-A turbulence model) and LES based on Smagorinsky sub-grid scale model.

#### 3.2.5.1 Spalart-Allmaras Turbulence Model

The S-A model solves a transport equation for the working variable $\hat{\nu}$ related to the turbulent viscosity, $\mu_t$. The following equation describes the transport of $\hat{\nu}$

$$\begin{aligned}\frac{\partial\hat{\nu}}{\partial t}+u_j\frac{\partial\hat{\nu}}{\partial x_j}&=c_{b1}\hat{S}\hat{\nu}-\frac{M_\infty}{Re_L}c_{w1}f_w\left(\frac{\hat{\nu}}{d}\right)^2\\&+\frac{M_\infty}{Re_L}\frac{1}{\sigma}\left[\frac{\partial}{\partial x_j}\left((\nu+\hat{\nu})\frac{\partial\hat{\nu}}{\partial x_j}\right)+c_{b2}\frac{\partial^2\hat{\nu}}{\partial x_j^2}\right],\end{aligned}\tag{3.39}$$

where $d$ is the distance to the nearest wall and $\hat{\nu}$ is the working variable. The turbulent eddy viscosity $\nu_t$ is obtained from

$$\nu_t=\rho\hat{\nu}f_{v1},\qquad f_{v1}=\frac{\chi^3}{\chi^3+c_{v1}^3},\qquad \chi\equiv\frac{\hat{\nu}}{\nu},\tag{3.40}$$

where $\nu$ is the kinematic molecular viscosity.

The first term in Equation 3.39 is the production term and is defined as follows:

$$\hat{S}=S+\frac{M_\infty}{Re_L}\frac{\hat{\nu}f_{v2}}{\kappa^2d^2},\qquad f_{v2}=1-\frac{\chi}{1+\chi f_{v1}},\tag{3.41}$$

where $S$ is the vorticity magnitude defines as

$$S = \sqrt{\Omega_{ij}\Omega_{ij}}, \qquad \Omega_{ij} = \frac{1}{2}\left(\frac{\partial u_i}{\partial x_j} - \frac{\partial u_j}{\partial x_i}\right). \tag{3.42}$$

$$\tag{3.43}$$

The second term in Equation 3.39 is the wall destruction term, which is defined as follows:

$$f_w = g\left[\frac{1+c_{w3}^6}{g^6+c_{w3}^6}\right]^{1/6}, \qquad g = r + c_{w2}\left(r^6 - r\right), \qquad r = \frac{M_\infty}{Re_L}\frac{\hat{\nu}}{\hat{S}\kappa^2 d^2}. \tag{3.44}$$

The third term in Equation 3.39 represents the diffusion of the modified turbulent viscosity $\hat{\nu}$. The flow is assumed to be fully turbulent thus the trip terms in the original S-A model are neglected. The rest of the constants are defined as follows:

$$\begin{aligned} c_{b1} = 0.1355, \qquad \sigma = 2/3, \qquad c_{b2} = 0.622, \\ \kappa = 0.41, \qquad c_{w3} = 2.0, \qquad c_{w2} = 0.3, \\ c_{v1} = 7.1, \qquad c_{t3} = 1.2, \qquad c_{t4} = 0.5. \end{aligned}$$

#### 3.2.5.2 Detached Eddy Simulation

Detached Eddy Simulation(DES) has been shown to be a useful approach to model massively separated flows. DES methodology has been successfully applied to the flow around high-lift devices [62], hence it is chosen for the present work. The DES model implemented in SotonCAA is based on the one-equation turbulence model of Spalart-Allmaras [54]. The motivation for DES is first highlighted by Spalart *et al.* [63] in 1997. The first true three-dimensional application, calibration of the $C_{DES}$ constant were conducted by Shur *et al.* [64].

In the S-A model the wall destruction term is proportional to $(\hat{\nu}/d^2)$. When the destruction term in balanced with the production term, the eddy viscosity is given by

$$\hat{\nu} \approx \hat{S}d^2, \tag{3.45}$$

where $\hat{S}$ is the local strain rate. In a LES, a sub-grid scale model is required to solve the turbulent stresses that are not resolved by the mesh. Following these arguments, Spalart *et al.* [63] suggested to replace $d$ with a new length $\tilde{d}$ given by

$$\tilde{d} = \min(d, C_{DES}\Delta), \tag{3.46}$$

where $\Delta = \max(\Delta x, \Delta y, \Delta z)$ is the computational mesh size. When the distance to the nearest wall is smaller than $C_{DES}\Delta$ the model behaves as a RANS model. When $d > C_{DES}\Delta$ the model behaves in LES mode. The transition between the RANS and LES models can be controlled by modifying the constant $C_{DES}$ and locally refining the grid.

The transition between RANS and LES models has been identified as a potential problematic region. In this zone the model needs to convert from fully modeled turbulence (attached boundary layer) to mostly resolved turbulence (massive separation). The problem occurs when the switching to LES mode occurs inside the boundary layer, for example, when the grid spacing parallel to the wall becomes less than the boundary-layer thickness, either as a result of grid refinement or boundary layer thickening. The grid spacing is then fine enough such that the $\tilde{d} = C_{DES}\Delta$ branch of Eq. 3.46 is active in the boundary layer. The result is weakened eddy viscosity, but not weak enough to allow LES eddies to develop, which yields lower Reynolds stress levels compared to those provided by the RANS model. The depleted stresses reduce the skin friction, which can lead to premature separation. These effects are referred to as Modeled-Stress Depletion(MSD) and Grid-Induced Separation(GIS) respectively [65]. In order to prevent MSB leading to GIS, Spalart *et al.* [65] introduced Delayed DES. To distinguish between the two DES formulations, the original DES as DES97 and the new version as DDES. The new formulation DDES uses a function to 'shield' the boundary layer, thus preserving RANS mode and delaying LES mode. For DDES, the parameter $r$ is slightly modified relative to the S-A definition, in order to apply to any eddy viscosity model, and be slightly more robust in irrotational regions:

$$r_d = \frac{\nu_t + \nu}{\sqrt{U_{i,j}U_{i,j}}\kappa^2 d^2}, \tag{3.47}$$

where $\nu_t$ is the kinematic eddy viscosity, $\nu$ is the molecular viscosity, $U_{i,j}$ is the velocity gradient, $\kappa$ is the von Karman constant, and $d$ is the distance to the nearest wall. It turns out that the parameter is equal to 1 in a logarithmic layer and falls to 0 gradually towards the edge of the boundary layer. The term $\nu$ is added to the numerator to correct the very near wall-behaviour of the model by ensuring that the parameter $r_d$ remains away from 0. In the S-A model, $\hat{\nu}$ can be used instead of $\nu_t + \nu$. The shield function is then defined as

$$f_d = 1.0 - \tanh([8r_d]^3), \tag{3.48}$$

which in the LES region is equal to 1 (where $r_d << 1$) and in the RANS region is

equal to 0. The DES length scale in Eq. 3.49 is redefined as

$$\tilde{d} = d - f_d \max(0, d - C_{DES}\Delta), \tag{3.49}$$

where $d$, $C_{DES}$, and $\Delta$ are as defined before. Thus when $f_d = 0$ then $\tilde{d} = d$ and RANS mode is active where as when $f_d = 1$ then $\tilde{d} = \min(d, C_{DES}\Delta)$ as in Eq. 3.49.

Another problem with the DES97 formulation is the premature activation of low-Reynolds number terms in the S-A RANS model. The low-Reynolds number terms in the S-A RANS model accounts for wall proximity, based on the ratio of the eddy viscosity and the molecular viscosity $\hat{\nu}/\nu$. However in the LES mode of DES, the subgrid eddy viscosity decreases with grid refinement and decrease of the flow Reynolds number. At some point, standard DES approach will mis-interpret the lower eddy viscosity as wall proximity effect and further lower the eddy viscosity. This problem is only evident at low Reynolds number and on very fine grids. A correction developed for DES97 formulation is as follow:

$$\tilde{d} = \min(d, \Psi C_{DES}\Delta), \tag{3.50}$$

where the function $\Psi$ is given by

$$\Psi^2 = \min\left[10^2, \frac{1 - \frac{c_{b1}}{c_{w1}\kappa^2 f_w^*}[f_{t2} + (1 - f_{t2})f_{v2}]}{f_{v1}\max(10^{-10}, 1 - f_{t2})}\right], \tag{3.51}$$

where all the functions are as defined in the S-A model equation and $f_w^* = 0.424$.

The DES formulations with the low-Reynolds number corrections are implemented by the author in SotonCAA solver. The present simulations employs the DDES formulation with the low-Reynolds number corrections.

### 3.2.6 Boundary Conditions

The no-slip condition is imposed by setting the cartesian velocity components to zero at the walls. The working variable $\hat{\nu}$ in the S-A turbulence model is set to zero. The temperature at the wall ($T_w$)is determined by the adiabatic conditions.

An explicit buffer zone method is used on the computational domain boundaries. The computational domain is extended to create an extra layer, the buffer zone, around it. In the buffer zone the solution vector is explicitly damped after each

time step using the following

$$\mathbf{Q}^{n+1} = \mathbf{Q}^{n+1} - \sigma_{bz}\left(\mathbf{Q}^{n+1} - \mathbf{Q}^{\text{target}}\right) \tag{3.52}$$

where $\mathbf{Q}^{n+1}$ is the solution vector after each time step and $\mathbf{Q}^{\text{target}}$ is the value at the outer boundary of the buffer zone. The damping coefficient $\sigma_{bz}$ varies smoothly according to the function

$$\sigma_{bz}(x_{bz}) = \alpha_{bz}\left(1 + \frac{x_{bz} - L_{bz}}{L_{bz}}\right)^{\beta_{bz}} \tag{3.53}$$

where $L_{bz}$ is the width of the buffer zone, $x_{bz}$ is the distance measured from the inner boundary of the buffer zone and $\alpha_{bz}$ and $\beta_{bz}$ are coefficients which determine the shape of the damping function. In the present study, $\alpha_{bz} = 1.0$, $\beta_{bz} = 1.5$ and $L_{bz} = 20$ grid points. The target values at the outer boundary of the buffer zone are set to the freestream values.

Grid singularity due to grid skew is a major problem for high-order finite difference schemes. Grid singularity can occur at inter-block boundaries where two or more grid lines meet at different angles. These regions give rise to errors due to the discontinuity in the compact central finite difference stencil. Skewed grid lines are often unavoidable especially for complex geometry such as the High-Lift geometry in this work. To overcome this problem the characteristics interface conditions (CIC) of Kim and Lee [66] are used. In this approach, the governing equations are cast in their characteristic form and the computational domain is decomposed into separate blocks. The biased stencil, outlined above in Equation 3.17, is used at the block boundaries so that the differencing stencils do not cross the block boundary, thereby avoiding the discontinuity. The central stencil is still used within the interior of each block. Interface conditions are then imposed at the block interfaces for communication between the blocks.

## 3.3 FW-H Solver

The far-field noise is computed using an integral solution to the FW-H equations. The implementation is based on Formulation 1A of Farassat [67]. The FW-H equation represents an exact rearrangement of the Navier-Stokes equation which can be used to compute acoustic field when solid boundaries are involved in the generation of sound. The FW-H solver has been previously used to compute far-

field noise from a slat [16, 29] and from an open cavity [68].

The solution to the FW-H equation consists of surface integrals and volume integrals. The surface integrals represent contributions from the monopole and dipole acoustic sources while the volume integrals represent the contributions from the quadrupole sources in the region outside the source surface. The volume source term consists of quadrupole sources in the flow, therefore the volume sources noise scales with the freestream velocity to the power of eight. Since the freestream Mach number is relatively small, the contribution from the volume source term is therefore very small hence can be neglected. Thus after dropping the volume integrals the pressure at the observer is given by

$$\acute{p}(\mathbf{x},t) = \acute{p}_T(\mathbf{x},t) + \acute{p}_L(\mathbf{x},t). \tag{3.54}$$

The two first terms on the right-hand side of Equation (3.54) are given by

$$4\pi\acute{p}_T(\mathbf{x},t) = \int_{f=0}\left[\frac{\rho_0(\dot{U}_n + U_n)}{r(1-M_r)^2}\right]_{ret} dS + \int_{f=0}\left[\frac{\rho_0 U_n\left\{r\dot{M}_r + c_0(M_r - M^2)\right\}}{r^2(1-M_r)^3}\right]_{ret} dS, \tag{3.55}$$

$$4\pi\acute{p}_L(\mathbf{x},t) = \frac{1}{c_0}\int_{f=0}\left[\frac{\dot{L}_r}{r(1-M_r)^2}\right]_{ret} dS + \int_{f=0}\left[\frac{L_r - L_M}{r^2(1-M_r)^2}\right]_{ret} dS + \frac{1}{c_0}\int_{f=0}\left[\frac{L_r\left\{r\dot{M}_r + c_0(M_r - M^2)\right\}}{r^2(1-M_r)^3}\right]_{ret} dS, \tag{3.56}$$

where

$$U_i = v_i + \frac{\rho}{\rho_0}(u_i - v_i), \tag{3.57}$$

and

$$L_i = P_{ij}\hat{n}_j + \rho u_i(u_n - v_n), \tag{3.58}$$

where $u_i$ and $u_n$ are the fluid velocity component in the $x_i$ direction and normal to the integration surface respectively. While $v_i$ and $v_n$ are the integration surface velocity component in the $x_i$ direction and in the normal direction respectively. The compressive stress tensor $P_ij = (p - p_0)\partial_{ij} - \sigma_{ij}$, $\rho$ is the air density at the integration surface and $\rho_0$ is the ambient air density. The square brackets ($[]_{ret}$) in Equations (3.55) and (3.56) denote that the kernels of the integrals are computed

at the corresponding retarded times, $\tau$, defined as follows

$$\tau = t - \frac{r}{c_\infty}, \tag{3.59}$$

where $t$ is the observer time and $r$ is the distance to the observer. The various subscripted quantities appearing in Equations (3.55) and (3.56) are the inner products of a vector and a unit vector implied by the subscript e.g. $L_r = \mathbf{L} \cdot .\hat{\mathbf{r}}$ and $U_n = \mathbf{U} \cdot \hat{\mathbf{n}}$ where $\hat{\mathbf{r}}$ and $\hat{\mathbf{n}}$ denote the unit vectors in the radiation and wall-normal directions respectively. The dot over the variable denotes source-time differentiation of the variable.

## 3.4 Low-Order CFD Solver

In addition to the high-order accurate solver SotonCAA, a low-order commercial CFD solver is employed to simulate the flow around more complex geometries for which a fully structured grid could not be constructed. The solver used is a cell-centered, finite volume commercial CFD code. Discrete values of the scalar quantities are stored at the cell centre and interpolated to determine face values for convective terms. The governing equations of continuity, momentum and energy are solved simultaneously in a coupled manner. The discretisation scheme for the flow was a second order upwind. The turbulent quantities are discretised using a second order upwind scheme. An implicit second order time marching scheme with dual time stepping is used. The one-equation Spalart-Allmaras [54] (here-on referred to as S-A) turbulence model is used to model the effects of turbulence. The reduced computational cost of solving only one equation and the ability to capture separated flow made it the best choice for this work.

The computations are performed in parallel on a Linux high performance cluster. The computational domain is divided into smaller subdomains or partitions which are then solved simultaneously using multiple computer nodes. Partitioning of the computational domain is carried out automatically into equal size partitions for even distribution over the computing nodes.

### 3.4.1 Governing Equations

The governing equations solved are the time accurate unsteady compressible Navier-Stokes equations. The instantaneous flow field variables are decomposed

into the ensemble-averaged component and the fluctuating component, such that $u_i = \bar{u}_i + u_i^{'}$. The governing equation for a variable-density flow are the Favre-averaged Navier-Stokes equations given in Equations (3.60) - (3.62):

$$\frac{\partial \bar{\rho}}{\partial t} + \frac{\partial \bar{\rho}\bar{u}_i}{\partial x_i} = 0, \tag{3.60}$$

$$\frac{\partial \bar{\rho}\bar{u}_i}{\partial t} + \frac{\partial \bar{\rho}\bar{u}_i\bar{u}_j}{\partial x_j} = \frac{\partial \bar{p}}{\partial x_i} + \frac{\partial}{\partial x_j}\left(-\overline{\rho u_i^{'} u_j^{'}} + \overline{\tau_{ij}}\right), \tag{3.61}$$

$$\begin{aligned}\frac{\partial \bar{\rho}\bar{E}}{\partial t} + \frac{\partial}{\partial x_j}\left\{\left(\bar{\rho}\bar{E} + \bar{p}\right)\bar{u}_j\right\} = -\frac{\partial}{\partial x_j}\left(\bar{q}_j + \overline{\rho u_j^{'} e^{'}}\right) \\ + \frac{\partial}{\partial x_j}\left\{\bar{u}_i\left(\bar{\tau}_{ij} - \overline{\rho u_i^{'} u_j^{'}}\right)\right\} + \frac{\partial}{\partial x_j}\left(\overline{\tau_{ij} u_i^{'}} - \frac{1}{2}\overline{\rho u_j^{'} u_i^{'} u_i^{'}}\right),\end{aligned} \tag{3.62}$$

where $u_i^{'}$ and $e^{'}$ are the unresolved turbulent fluctuations in flow velocity and specific internal energy respectively. The Favre-averaged total energy is given by

$$\bar{\rho}\bar{E} = \bar{\rho}\left(\bar{e} + \frac{1}{2}\bar{u}_i\bar{u}_i\right) + \frac{1}{2}\overline{\rho u_i^{'} u_i^{'}}, \tag{3.63}$$

where $\bar{e}$ is the Favre-averaged specific internal energy. The two additional terms compared to the instantaneous Navier-Stokes equations are $-\overline{\rho u_i^{'} u_j^{'}}$ and $\overline{\rho u_j^{'} \acute{e}}$, namely the Reynolds stress tensor and the turbulent heat flux respectively. The Reynolds stresses are related to the mean velocity by invoking the Boussinesq assumption,

$$-\overline{\rho u_i^{'} u_j^{'}} = \mu_t\left(\frac{\partial u_i}{\partial x_j} + \frac{\partial u_j}{\partial x_i}\right) - \frac{2}{3}\left(\rho k + \mu_t \frac{\partial u_i}{\partial x_i}\right)\delta_{ij}, \tag{3.64}$$

thus the viscous stress tensor is given by

$$\bar{\tau}_{ij} = (\mu + \mu_t)\left[\left(\frac{\partial \bar{u}_j}{\partial x_i} + \frac{\partial \bar{u}_i}{\partial x_j}\right) - \frac{2}{3}\frac{\partial \bar{u}_k}{\partial x_k}\delta_{ij}\right], \tag{3.65}$$

where $\mu_t$ is the turbulent viscosity. The heat flux vector is given by the following equation:

$$\bar{q}_{ij} = -\left(\frac{\mu}{Pr} + \frac{\mu_t}{Pr_t}\right) c_p \frac{\partial \bar{T}}{\partial x_j}, \tag{3.66}$$

where $Pr$ and $Pr_t$ are the Prandtl number and the turbulent Prandtl number respectively.

### 3.4.2 Turbulence Modelling

The S-A model solves one transport equation for the modified turbulent viscosity ($\tilde{\nu}$)

$$\frac{\partial(\rho\tilde{\nu})}{\partial t} + \frac{\partial(\rho\tilde{\nu}u_i)}{\partial x_j} = c_{b1}\rho\tilde{S}\tilde{\nu} + \frac{1}{\sigma}\left[\frac{\partial}{\partial x_j}\left\{(\mu+\rho\tilde{\nu})\frac{\partial\tilde{\nu}}{\partial x_j}\right\} + c_{b2}\rho\left(\frac{\partial\tilde{\nu}}{\partial x_j}\right)^2\right] - \left[c_{w1}\rho f_w\left(\frac{\tilde{\nu}}{d}\right)^2\right] \quad (3.67)$$

The modified turbulent viscosity ($\tilde{\nu}$) is related to the turbulent viscosity ($\mu_t$) by the following relationship

$$\mu_t = \rho\tilde{\nu}f_{v1} \quad (3.68)$$

where $f_{v1}$ is given by

$$f_{v1} = \frac{\chi^3}{\chi^3 + c_{v1}^3}, \qquad \chi \equiv \frac{\tilde{\nu}}{\nu}. \quad (3.69)$$

The first term on the right-hand side of Equation (3.67) represents the production of modified turbulent viscosity. The definitions of the functions are as follows:

$$\tilde{S} = S + \frac{\tilde{\nu}}{\kappa^2 d^2}f_{v2}, \qquad f_{v2} = 1 - \frac{\chi}{1+\chi f_{v1}}, \quad (3.70)$$

where $S$ is the magnitude of the vorticity,

$$S \equiv \sqrt{2\Omega_{ij}\Omega_{ij}}, \qquad \Omega_{ij} = \frac{1}{2}\left(\frac{\partial u_i}{\partial x_j} - \frac{\partial u_j}{\partial x_i}\right) \quad (3.71)$$

and $d$ is the distance to the closest wall. The second term of the right-hand side of Equation (3.67), models the diffusion of the modified turbulent viscosity, while the last term represents the destruction of the modified turbulent viscosity ($\tilde{\nu}$). The function $f_w$ is

$$f_w = g\left[\frac{1+c_{w3}^6}{g^6+c_{w3}^6}\right]^{1/6}, \qquad g = r + c_{w2}\left(r^6 - r\right), \qquad r = \frac{\tilde{\nu}}{\tilde{S}\kappa^2 d^2}. \quad (3.72)$$

The constants in the S-A model have the following values; $c_{b1} = 0.1355$, $c_{b2} = 0.622$, $\sigma = 2/3$, $c_{v1} = 7.1$, $c_{w1} = c_{b1}/\kappa^2 + (1+c_{b2})/\sigma$, $c_{w2} = 0.3$, $c_{w3} = 2.0$ and $\kappa = 0.4187$.

### 3.4.3 Boundary Conditions

The non-reflecting pressure far-field boundary condition is used on the domain edges. The pressure far-field boundary condition is based on Riemann invariants for a 1-D flow normal to the boundary. For subsonic flow, the two Riemann invariants corresponding to incoming and outgoing waves respectively are

$$R_\infty = u_{n,\infty} + \frac{2c_\infty}{\gamma - 1}, \tag{3.73}$$

and

$$R_i = u_{n,i} - \frac{2c_i}{\gamma - 1}, \tag{3.74}$$

where $u_n$ is the velocity normal to the boundary, and $c$ is the local speed of sound. The subscript $\infty$ refers to flow variables at infinity (the boundary condition) and the subscript $i$ refers to interior flow variables. Adding and subtracting the two Riemann invariants in Equation (3.73) and (3.74) results in the following equations for the velocity normal to the boundary and the local speed of sound respectively:

$$u_n = \frac{1}{2}\left(R_i + R_\infty\right), \tag{3.75}$$

and

$$c_i = \frac{\gamma - 1}{4}\left(R_i - R_\infty\right). \tag{3.76}$$

At the boundary, the values of tangential velocity and entropy are extrapolated from the interior. The flow variables at the boundary can be computed using the values for normal velocity and speed of sound applied to the boundary (given in Equations (3.75) and (3.76) respectively), the extrapolated values of tangential velocity and the entropy.

The freestream boundary conditions are summarised in Table 3.3.

Table 3.3: Pressure far-field boundary conditions

| **Parameter** | **Symbol** | **Value** |
|---|---|---|
| Freestream Mach Number | $M_\infty$ | 0.235 |
| Freestream static pressure | $p_\infty$ | 101325 N/m$^2$ |
| Freestream static temperature | $T_\infty$ | 288.16 K |
| Turbulent viscosity ratio | $\mu_t/\mu$ | 10 |
| Angle of attack | $\alpha$ | 5 degrees |

The no-slip wall boundary condition with the gradient of pressure normal to the wall set to zero is used on the wall. The wall boundary condition for the modified turbulent viscosity is $\tilde{\nu} = 0$. The density is computed using the ideal gas law. The molecular viscosity is computed using Sutherland's law with three coefficients

$$\mu = \mu_0 \left( \frac{T}{T_0} \right)^{3/2} \frac{T_0 + S}{T + S} \tag{3.77}$$

where $\mu_0$ is the reference value in kg/m-s, $T_0$ is the reference temperature in Kelvin and $S$ is an effective temperature in K (Sutherland constant).

## 3.5 Summary

The details of the computational methods employed in the current study have been discussed. The unsteady flow fields around the high-lift devices are obtained using a low-order and a high-order CFD solver. The low-order CFD solver employs second-order temporal and spatial schemes whereas the high-order CFD solver employs second-order temporal and 4th-order spatial schemes. The details of the governing equations, turbulence models and boundary conditions for the two CFD solvers have been presented.

The high-order CFD/CAA solver is used in the computation of the flow around the 2D and 3D HLDs in Chapter 4 and Chapter 5. Use of the high-order spatial scheme enables detailed flow structures to be captured that are responsible for noise generation. The 3D simulation of the flow around the HLD with a half-span spoiler, in Chapter 6, is performed using the low-order CFD solver. The low-order CFD solver is capable of handling unstructured mesh which is used due to the complexity of the geometry.

The S-A turbulence model is employed in all the 2D simulations whereas the 3D simulations employs S-A based DES turbulence model. The unsteady data is then used as input to a FW-H solver that computes the far-field noise.

# Chapter 4

# 2D Simulation of High-Lift Devices

## 4.1 Introduction

In this chapter the results of the 2D Unsteady Reynolds-Averaged Navier-Stokes(URANS) simulations of the conventional and steep HLDs are presented and discussed. The simulation of the near flow field is performed using high-order accurate spatial discretisation schemes. The unsteady CFD data obtained is used as input to an FW-H integral method to compute the far-field noise characteristics.

SotonCAA is used to compute the unsteady flow field around the HLDs. Details of the SotonCAA numerical schemes and the FW-H solver are presented in Chapter 3. The spatial discretisation is performed using a 4th-order optimized compact prefactored scheme of Ashcroft and Zhang [50]. This choice is driven by the need to capture fine details of the unsteady flow around the high-lift system without the added cost of very fine grids required when low-order spatial discretization schemes are used.

The chapter is divided into four sections. Section 4.2 contains details of the high-lift geometry, flow conditions, grid details and the solution methodology. Section 4.3 presents the results of the unsteady flow simulation around the high-lift devices with and without the spoiler deployed. In section 4.4, details of the near-field noise propagation and the far-field noise directivity and spectra are presented. Finally a summary of the main findings from the 2D computations is presented in section 4.5.

## 4.2 Geometry of HLDs and Flow Conditions

The high-lift model comprises of a slat, main-element and flap. The model stowed chord length is $C = 1.0$ m. The slat and flap chord lengths are 12% and 25% of the model stowed chord length respectively. The deflection angles for the slat and the flap are 30 and 38 degrees respectively. The *steep* configuration has a spoiler deployed at an angle of 20 degrees. Figure 4.1 shows the geometry of the *steep* high-lift configuration. The conventional high-lift configuration is identical to Fig. 4.1, except the spoiler is retracted to form the main-element trailing edge. The geometrical settings for the two HLDs are summarised in Table 4.1. The model angle of attack is set to 5.0 degrees which corresponds to a typical setting for approach to landing. The freestream Mach number is $M_\infty = 0.235$, which corresponds to a Reynolds number $Re = 5.47 \times 10^6$ based on the model stowed chord. All the HLD trailing edges are modeled as sharp edges except for the spoiler trailing edge which has a thickness of 0.33% of the model stowed chord. This is in order to focus on the noise sources around the spoiler.

Table 4.1: Geometrical settings for the HLDs.

| **Parameter** | **Symbol** | **Conventional** | **Steep** |
|---|---|---|---|
| Reference chord (m) | $C$ | 1.00 | 1.00 |
| Slat angle, degrees | $\delta_s$ | 30 | 30 |
| Slat gap, % $C$ | $g_s$ | 0.50 | 0.50 |
| Slat overhang, % $C$ | $o_s$ | 1.22 | 1.22 |
| Flap angle, degrees | $\delta_f$ | 38 | 38 |
| Flap gap, % $C$ | $g_f$ | 2.3 | 9.34 |
| Flap overhang, % $C$ | $o_f$ | 0.57 | 1.28 |
| Spoiler angle, degrees | $\delta_{sp}$ | 0 | 20 |

### 4.2.1 Computational Grid Details

A structured 2D grid is generated around the two high-lift models. The grid generation follows an iterative development path, where the grids are refined based on previous flow field results. The aim is to obtain grids that can resolve relatively small scale flow features but are computationally less expensive. Preliminary CFD results demonstrate that the spoiler has a global effect on the flow field around the entire high-lift model. Therefore to accurately capture the effect of deploying

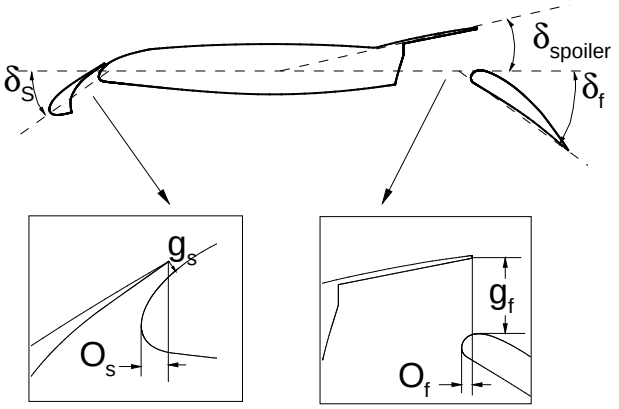


FIGURE 4.1: High-lift geometry for the *steep* configuration.

the spoiler, very fine grids are required around all three high-lift elements. Figure 4.2 shows the entire computational grid around the steep high-lift configuration.

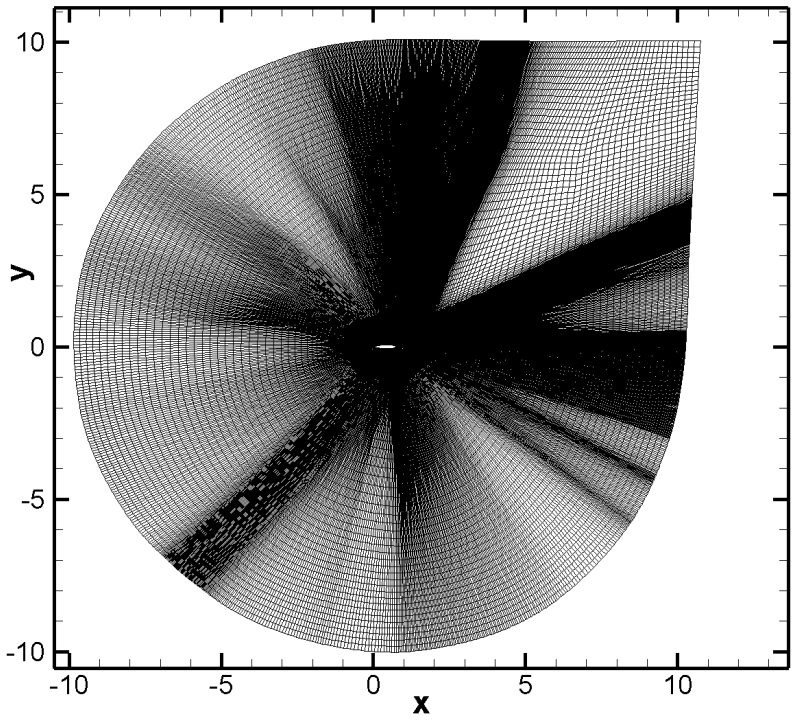


FIGURE 4.2: A view of the whole computational grid around the high-lift model.

The literature reviewed previously in Chapter 2 show that flow separation occurs on the slat in the slat cove, on the main-element in the cove region and on the flap suction surface near the trailing edge. Flow separation also occurs at the spoiler trailing edge. These regions of flow separation are associated with noise generation

from a high-lift wing, therefore extreme care is taken in constructing the grids in these key regions. Figure 4.3 shows the grid density in the slat cove, main-element cove, the spoiler trailing edge and around the flap. As noted previously, the slat and flap trailing edges are modeled as sharp edges, whereas the spoiler trailing edge thickness is modeled as with a finite thickness. The grid density around the spoiler trailing edge is important in order to capture the separated flow. On the finest grid, 40 grid points are used along the spoiler trailing edge in order to capture the the shedding of vortices from the edge.

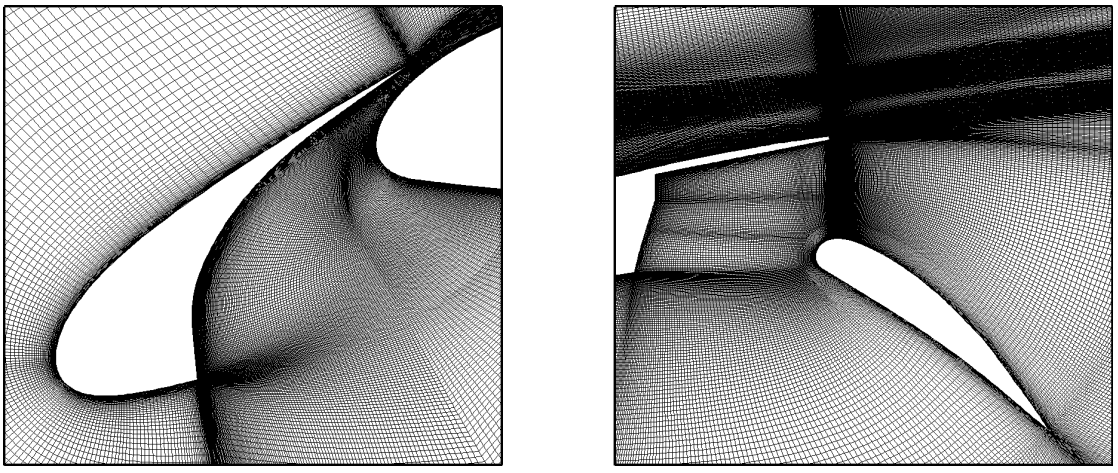

(a) Slat. (b) Flap.

FIGURE 4.3: Grid distribution in the vicinity of the slat and the flap.

In order to determine the appropriate grid resolution, three grid levels are generated for each high-lift configuration; a coarse, a medium and a fine grid. Successive grids are constructed by grid refinement in key regions of unsteady flow which includes the slat cove, main-element cove, and the wake of the spoiler and flap. Unlike a conventional grid convergence study, where the grid refinement is performed equally along all the grid directions, the aim of this task is to improve the grid resolution only in the key regions identified above. The grid sizes range from $2 \times 10^5$ grid points for the coarse grids to $6 \times 10^5$ grid points for the finest grids. The details of the coarse and fine grids are summarised in Table 4.2.

The pressure distribution around the conventional high-lift configuration obtained on the coarse, medium and fine grids is shown in Figure 4.4. The results show convergence of the pressure distribution with increased grid resolution. A similar trend is observed for the steep high-lift configuration. The finest grids are much better at capturing the unsteady flow structures in the region of flow separation. In addition, the finest grids are able to capture the propagation of sound waves

TABLE 4.2: Details of the grids for the conventional and steep HLDs.

| | **Conventional** | **Steep** |
|---|---|---|
| **Mesh** | Grid Size | Grid Size |
| Fine | $6.36 \times 10^5$ | $6.45 \times 10^5$ |
| Medium | $4.26 \times 10^5$ | $4.33 \times 10^5$ |
| Coarse | $2.19 \times 10^5$ | $2.95 \times 10^5$ |

generated by the unsteady flow field, as will be later shown. The results presented from here on are from simulations performed on the finest grids for both HLDs.

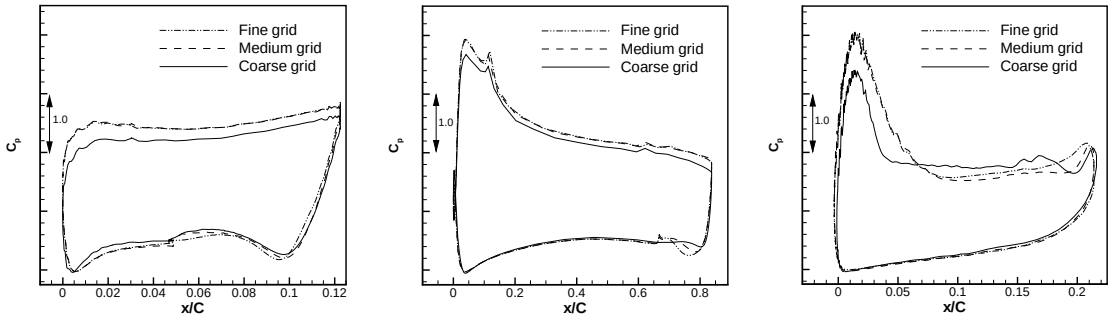


(a) Slat. (b) main-element. (c) Flap.

FIGURE 4.4: Comparison of the mean pressure distribution around the conventional high-lift configuration obtained using the coarse and fine grid.

The fine grids are designed to ensure $y^+ \approx 1$ along all solid walls. In order to achieve this, approximately 30 grid points are located in the boundary layers. A sample of the boundary layer velocity profile on the suction surface of the main-element at $x/C = 0.78$ is shown in Figure 4.5. A comparison is made with a typical turbulent boundary layer velocity profile in the viscous sublayer($y^+ < 5$) and the log-law region($y^+ > 30$). The log-law constants $\kappa$ and $B$ are set equal to 0.40 and 5.5 respectively. Reasonable agreement is obtained between the computed and the analytical velocity profiles in both the viscous sublayer and the log-law regions, which confirms that the wall normal grid resolution is sufficient to capture the boundary layer.

### 4.2.2 Computational Methodology

The governing equations are the compressible Navier-Stokes equations which are solved using a finite difference discretisation. Details of the numerical schemes

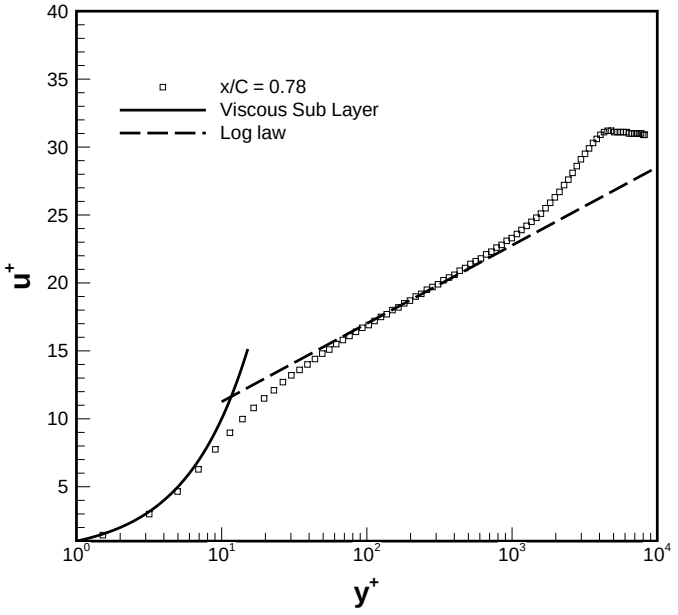


FIGURE 4.5: Comparison of the boundary layer velocity profile on the main-element at $x/C = 0.78$.

are outlined in Chapter 3. The solver employs a 4th-order spatial discretisation, using the optimised prefactored compact scheme of Ashcroft and Zhang [50]. The solver is limited to fully structured grids only due to the difficulty of extrapolating compact schemes to high-orders of accuracy on unstructured grids.

The computational domain is split into separate computational blocks in which the governing equations are solved separately. Due to the complexity of the high-lift geometry, grid singularities occur where an odd number of blocks of different orientations meet (such as in the slat cove). The derivatives calculated using the compact spatial stencils that cross over these block interfaces are in error and lead to instabilities in the computations. To overcome this problem, one-sided spatial stencils of reduced order are used at the block boundaries. The Characteristic Interface Condition(CIC) of Kim and Lee [66] is used to communicate flow information across the discontinuous block interface. The condition is implemented by solving the characteristic form of the Navier-Stokes equations separately on each side of the block interface. The characteristic waves are then communicated across the block interface. More details of the characteristic boundary condition can be found in the work of Kim and Lee [66]. The effectiveness of the characteristic interface condition is validated by simulating the propagation of a Gaussian pulse through the interface of 3 blocks, see Appendix B.2.

One of the main challenges of computational aeroacoustics is the setting of appropriate boundary conditions at the end of the computational domain. The requirement is for the boundary to allow all outgoing flow and acoustic disturbances to exit normally and to prevent any reflected flow and acoustic disturbances from contaminating the inner solution. To prevent any reflection from the boundaries, the simulations employ an explicit buffer zone boundary condition [69] at the computational domain extents. Details of the implementation of the buffer zone are outlined in Chapter 3. The effectiveness of the explicit buffer zone boundary condition in reducing reflections of acoustic perturbations from the domain boundaries is demonstrated using a test case in the Appendix B.3. In the 2D simulations, the explicit buffer zone is applied in a zone 20 grid points wide from the computational domain boundaries. The most effective damping coefficients are found to be $\sigma = 1.0$ and $\beta = 3.0$. In addition to the explicit buffer zone boundary condition, grid stretching is employed close to the computational domain boundary to help dampen any acoustic reflections. The no-slip boundary condition is imposed on the solid surfaces of the high-lift devices.

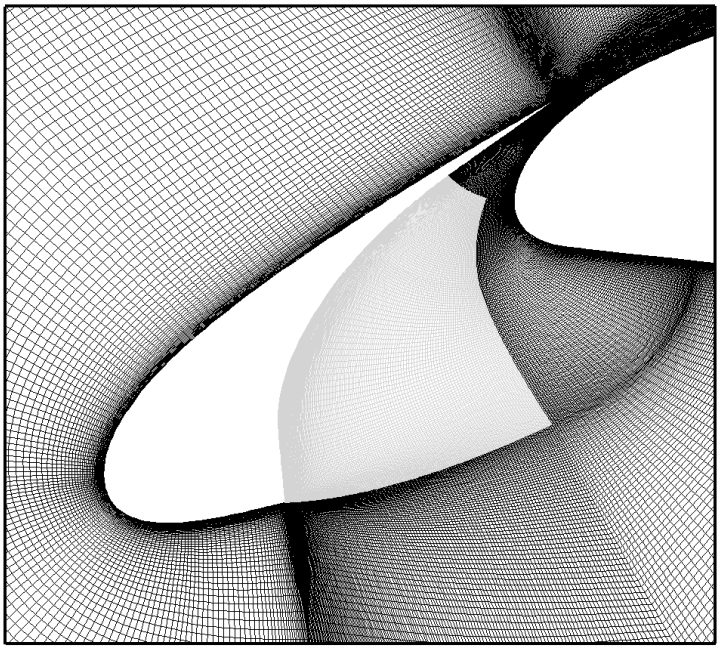

FIGURE 4.6: Grid around the slat showing the region, in gray, where the turbulence production is switched off.

The S-A turbulence model is used to model the effects of turbulence around the high-lift devices. Details of the implementation of the S-A turbulence model are outlined in Chapter 3. Based on recommendation by Khorrami *et al.* [19], the turbulence production term in the S-A model transport equation is switched off

in a region inside the slat cove. Figure 4.6 shows the region where the turbulence production is switched off. The turbulence model in its original form tends to have an excessively diffusive effect on the unsteady free shear layer that separates from the slat cusp. Turning the turbulence production off in this region reduces the level of turbulent viscosity and allows the free shear layer from the slat cusp to naturally roll up into vortices in the slat cove. For simulations at relatively low Reynolds numbers and at typical approach angle of attack, the distance between the stagnation point and the slat cusp is relatively small. Thus the boundary layer does not have enough time to develop to a fully turbulent boundary layer before it reaches the slat cove, where it can be considered to be 'quasi-laminar'.

A second order implicit LU scheme with Newton-like sub-iterations is employed for time integration. The simulations require 3 sub-iterations to drop the residuals by two orders of magnitude at each time step. Details of the time integration scheme are given in Chapter 3. The implicit time integration schemes have improved stability which allows larger time steps to be used in comparison to the Runge-Kutta explicit time integration schemes.

The non-dimensional time step is $\Delta t c_\infty / C = 1.0 \times 10^{-4}$ which yields a maximum Courant-Friedrichs-Lewy (CFL) number based on the freestream fasted characteristic velocity, $U_\infty + c_\infty$, equal to 10. The time step corresponds to a dimensional time step of $\Delta t = 2.9 \times 10^{-7}$ seconds, which results in a sampling frequency of 3.45 MHz. The flow-through time based on the reference chord and the freestream velocity is 43,100 time steps. The flow is run for 1 million time steps (equivalent to $\approx 23$ flow-through of the entire model stowed chord) before the flow data is sampled on the FW-H integration surfaces.

The computations are performed on a Linux cluster, Iridis 3, using 80 2.4 GHz Nehalem CPUs (with 8 CPUs per node) with 12GB of RAM and an Infiniband inter-communication network. The computational cost per time step is 0.4 seconds. Each 2D computation from start to end of sampling of data on FW-H integration surface requires approximately 12,000 CPU hours.

## 4.3 Aerodynamic Flow Field

In this section, the aerodynamic flow field obtained from the computations on the conventional and steep HLDs are analysed and discussed. The focus of the discussion is on the comparison between the two different flow fields around the

HLDs with and without the spoiler deployed. The changes in far-field noise level when the spoiler is deflected can then be related to the observed changes in the near-field caused by the spoiler deployment. This can help identify the most significant noise generating mechanisms for the steep high-lift configuration.

### 4.3.1 Time Averaged Flow Field

Figure 4.7 compares the time history of the lift and drag coefficients of the steep HLDs with the conventional HLDs. Deploying the spoiler increases the mean drag generated by the HLDs by a factor of 2 whereas the mean lift is reduced by approximately by a factor of 0.55. The increase in drag is a desirable effect for the purpose of slowing down the aircraft. However, the decrease in lift is undesirable since in order to meet the landing maximum lift requirements, an increase in approach speed and angle of attack is required. Since high-lift noise scales with the velocity, an increase in the approach speed would result in a further increase in aircraft noise level.

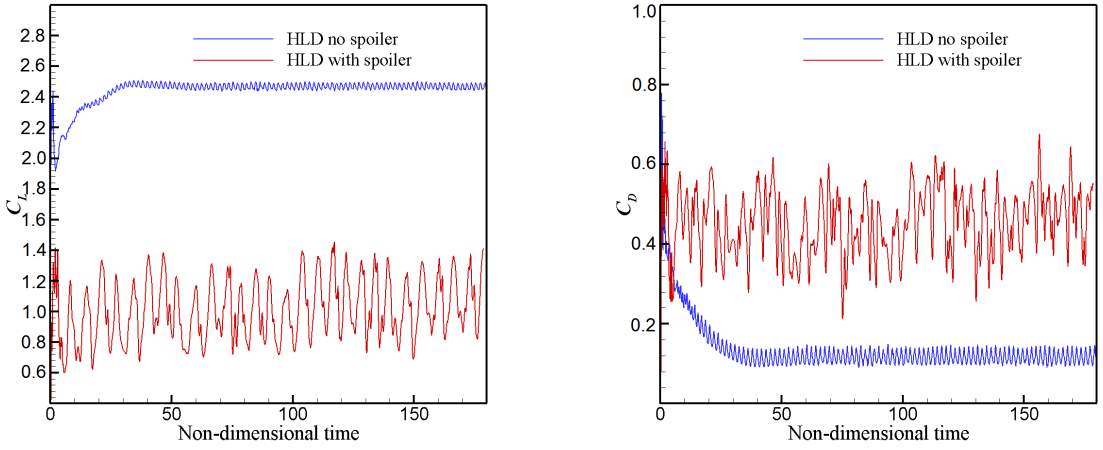


(a) Lift coefficient.

(b) Drag coefficient.

FIGURE 4.7: History of the lift and drag coefficients for the steep and conventional HLDs.

Deploying the spoiler increases the amplitude of the lift and drag fluctuations. The root mean square (RMS) of the lift and drag increases by an order of magnitude from $C_{L_{RMS}} = 0.0171$ to $C_{L_{RMS}} = 0.1944$ and $C_{D_{RMS}} = 0.0124$ to $C_{D_{RMS}} = 0.1085$ respectively. The lift and drag coefficients are related to the pressure distribution on the surface of the HLDs. The time derivative of the pressure fluctuations on the solid surfaces is proportional to the dipole noise term in the FW-H equation. Therefore an increase in the level of pressure fluctuations on the surface will lead

to a corresponding increase in the radiated noise from the surface. Figure 4.7 also shows that the frequency of the lift and drag fluctuation is reduced when the spoiler is deployed. For the conventional HLD, the frequency of the lift and drag fluctuation is $f = 100$ Hz, while for the steep high-lift configuration the frequency is $f = 52$ Hz.

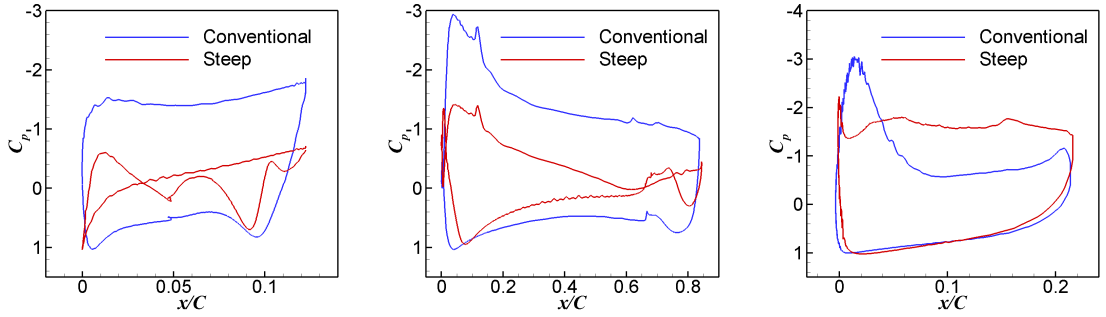


(a) Slat. (b) main-element. (c) Flap.

FIGURE 4.8: Distribution of the mean pressure coefficient around the steep and conventional HLDs.

Figure 4.8 shows the distribution of mean pressure on the surface of the steep and conventional HLDs. In Figure 4.8(a), the stagnation point on the slat has moved to the suction surface. Therefore deploying the spoiler has the effect of decreasing the angle of incidence on the slat. Comparison of the $C_p$ distribution on the main-element shows that, when the spoiler is deflected, the stagnation point moves downstream from $x/C_{main} = 0.02$ to $x/C_{main} = 0.04$. The magnitude of pressure suction peak on the main-element leading edge is reduced by half to $C_p = -1.5$. Figure 4.9 shows contours of time-averaged pressure around the conventional and steep HLDs respectively. In Figure 4.9(b) at the main-element trailing edge, the deflected spoiler causes a reduction in the pressure at the flap leading edge. The drop in pressure causes the flow to separate early. The separated flow region on the flap suction surface can be identified by the constant pressure plateau in the $C_p$ distribution of Figure 4.8(c).

The mean flow field around the conventional and steep HLDs is shown in Figure 4.10. Figures 4.10(a) and 4.10(b) show the time-averaged velocity field and streamlines around the slat for the conventional and steep high-lift configurations respectively. The streamlines clearly show the effect of deploying the spoiler on the flow around the slat. The flow incidence at the slat leading edge is reduced and the stagnation point has moved on to the slat suction surface. The slat cove flow recirculation expands when the spoiler is deployed. Figure 4.10(b) shows that when the spoiler is deflected, the flow separates at the main-element leading edge and

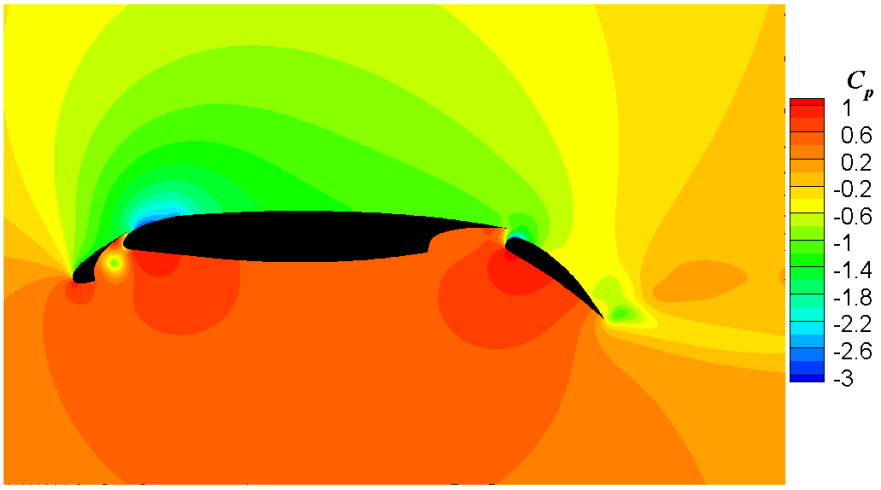


(a) Conventional configuration.

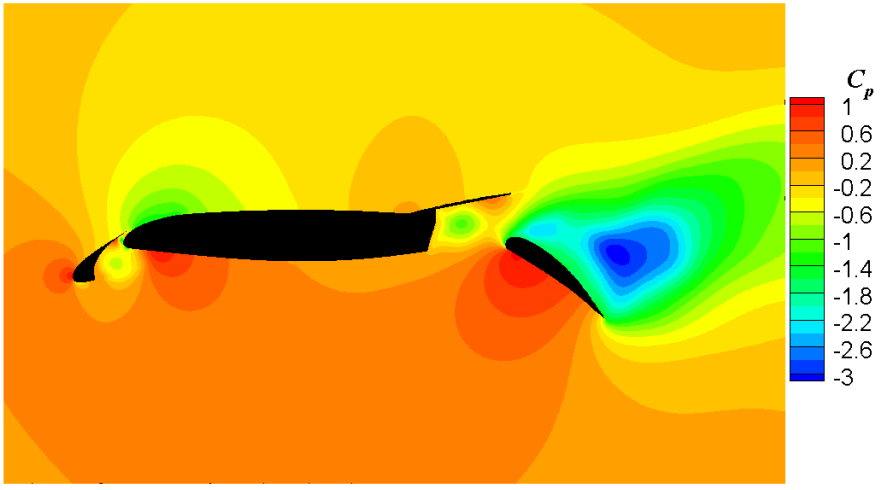


(b) Steep configuration.

FIGURE 4.9: Mean $C_p$ distribution around the steep and conventional HLDs.

reattaches to form a small separation bubble. Deflecting the spoiler reduces the effective flow incidence seen by the HLDs. The $C_p$ distribution in Figure 4.8(b) shows that this is accompanied by a significant reduction in the main-element leading edge suction peak pressure. When the spoiler is deployed, the boundary layer at the main-element leading edge cannot overcome the unfavourable pressure gradient on the main-element suction surface and thus flow separation occurs. The separated flow reattaches to the surface to form a small separation bubble.

The time averaged velocity field and streamlines around the flap region in Figure 4.10(d), clearly shows the large separated flow region on the flap suction surface caused by deploying the spoiler. In contrast when the spoiler is retracted, Figure 4.10(c), the flow separation is delayed and occurs approximately near the half-chord position.

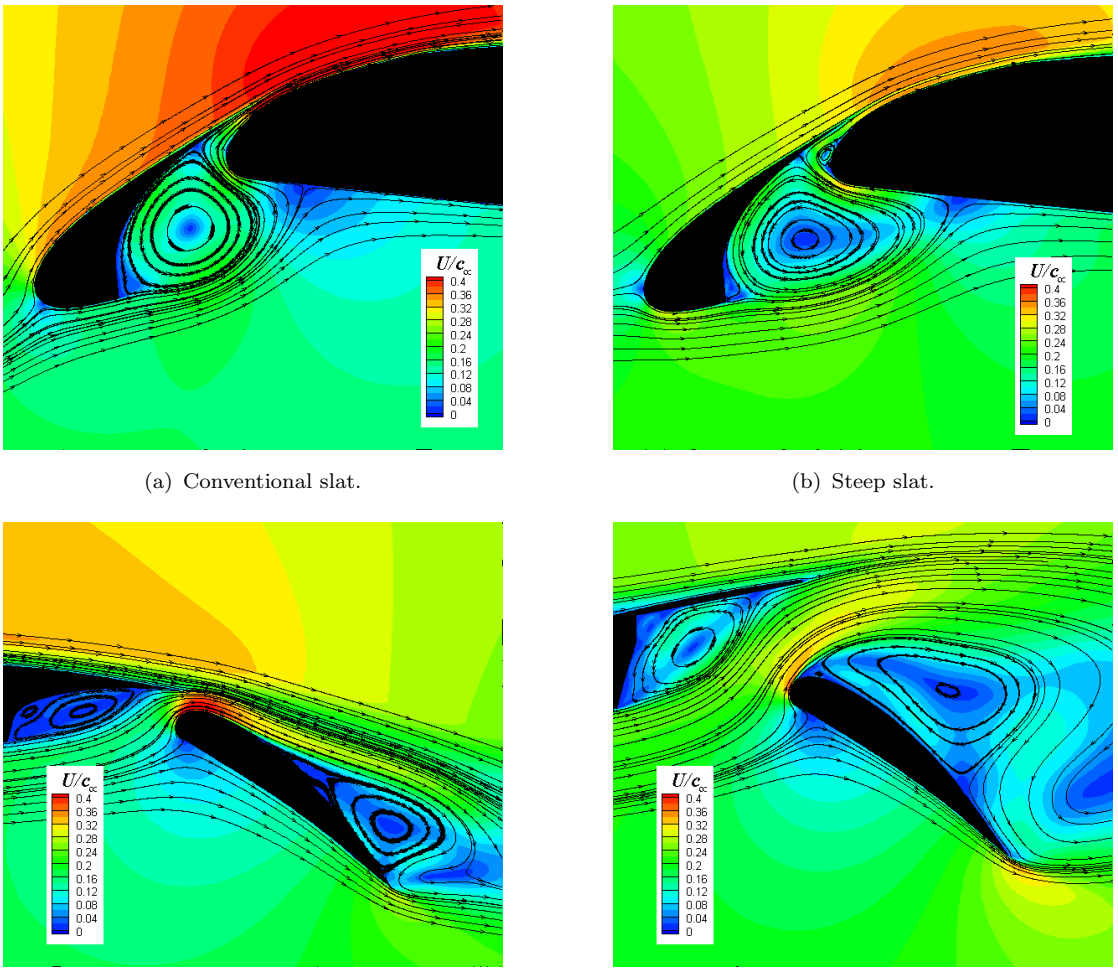


(a) Conventional slat.

(b) Steep slat.

(c) Conventional flap.

(d) Steep flap.

FIGURE 4.10: Mean velocity and flow streamlines around the slat and the flap.

### 4.3.2 Instantaneous Flow Field

A close-up snapshot of the instantaneous spanwise vorticity $\omega_z$ around the slat for the conventional and steep HLDs in Figures 4.11(a) and 4.11(b) respectively.

For both HLDs, a recirculating flow region occupies the slat cove. The boundary of the recirculation region is marked by a free shear layer that separates from the slat cusp. The separated free shear layer rolls up into discrete vortices in the slat cove. Figure 4.11(b) shows that deploying the spoiler causes the recirculation region to expand and the shear layer roll-up occurs further away from the slat cusp. This results in the formation of larger vortical structures in the slat cove. In both cases, the vortices formed by the free shear layer convect towards the reattachment point on the slat pressure surface. The vortices undergo distortions and stretching due to the flow deceleration at the reattachment point and subsequent acceleration through the slat gap.

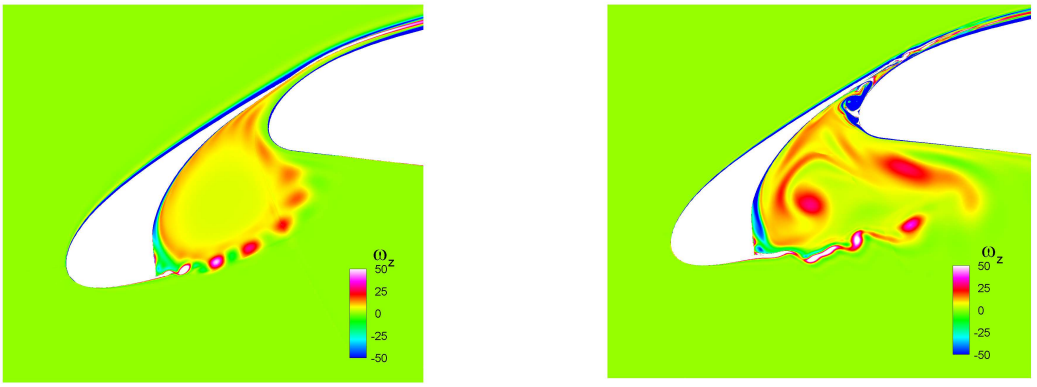


(a) Conventional configuration. (b) Steep configuration.

FIGURE 4.11: Instantaneous non-dimensional spanwise vorticity field around the slat.

The time series of the spanwise vorticity around the slat without the spoiler is shown in Figure 4.12. The shear layer from the slat cusp rolls into discrete spanwise vortices, that travel on the perimeter of the slat cove recirculation, towards the reattachment point on the pressure surface of the slat. At the slat reattachment point, the vortices are squashed due to the flow deceleration and then stretched as the flow accelerates towards the slat trailing edge.

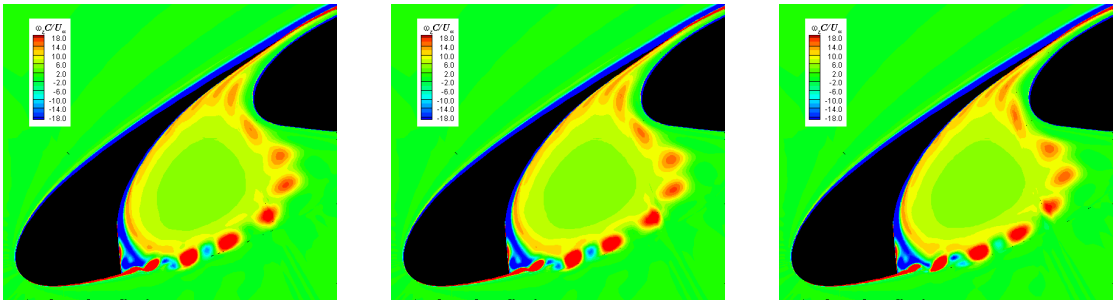

(a) (b) (c)

FIGURE 4.12: Time series of spanwise vorticity field around the slat without the spoiler.

Figure 4.13 shows a time sequence of the spanwise vorticity field around the slat when the spoiler is deployed. Examination of Figure 4.13 shows that, at the reattachment point, some vortices are trapped into the recirculation region. The vortices that remains in the slat cove convect towards the slat cusp, causing the flow to separate and forms vortices of opposite sign. Khorrami *et al.* [19] reported similar observations from their 2D simulation of the slat shear layer. The time series of the instantaneous flow field also shows that deploying the spoiler reduces

the vortex shedding frequency from the free shear layer that separates from the slat cusp.

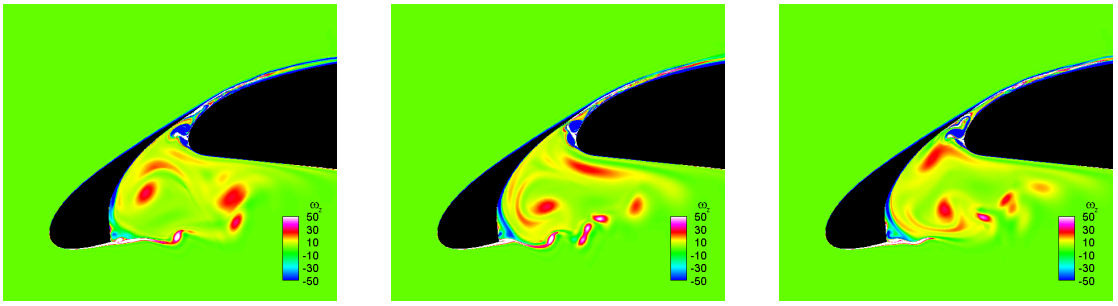


(a) (b) (c)

FIGURE 4.13: Time series of spanwise vorticity field around the slat with the spoiler deflected.

The time series of the spanwise vorticity field around the slat in Figure 4.13 shows the vortex shedding from the separated shear layer at the main-element leading edge into the slat gap. Only vortices of negative vorticity are shed from the main-element leading edge. The interaction of the vortices with the slat trailing edge is a potential noise source.

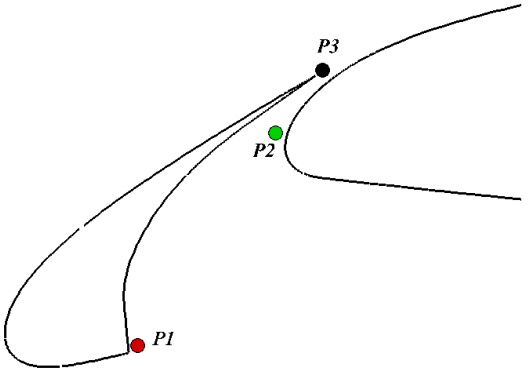


FIGURE 4.14: Location of pressure probes.

Pressure probes are located around the slat and main-element leading edge to monitor the fluctuating pressure field. Figure 4.14 shows the location of the pressure probes. The Power Spectral Density(PSD) of the pressure measured at the probes located at the slat cusp, slat trailing edge and main-element leading edge on the conventional and steep HLDs is presented in Figure 4.15. In the

absence of the spoiler, the pressure fluctuations in the slat cove are driven by the vortex shedding at the slat cusp. The power spectra in Figure 4.15(a) show a fundamental peak at $f = 2.5$ kHz ($St = 3.8$ based on the slat chord) and peaks at sub-harmonics frequencies for all three locations.

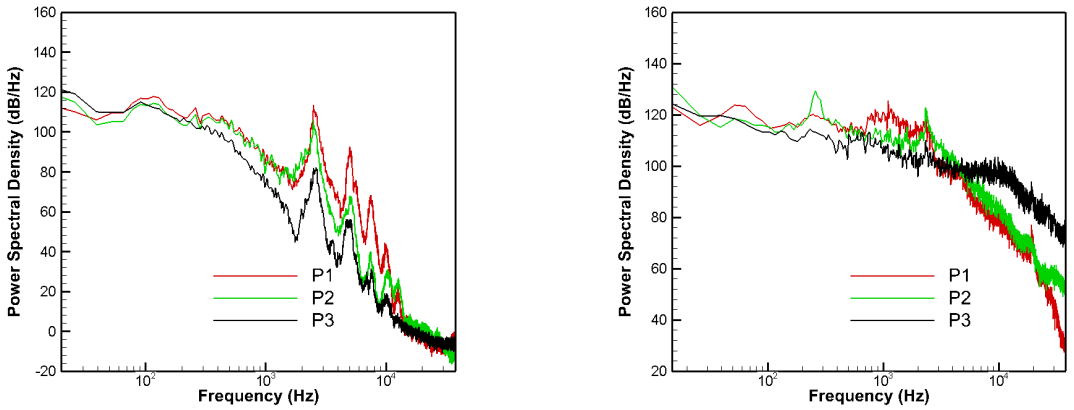


(a) Conventional HLDs.

(b) Steep HLDs.

FIGURE 4.15: The PSD of the pressure probes around the slat region.

When the spoiler is deployed, the power spectrum at the slat cusp has two prominent peaks at $f = 1.1$ and 2.3 kHz. The frequencies correspond to $St = 1.7$ and $St = 3.6$ based on the slat chord. The peaks are caused by the shedding of vortices from the shear layer that separates from the slat cusp. Therefore the deploying spoiler results in a reduction in the frequency of vortex shedding from the slat cusp. The power spectra of the probes located near the main-element leading edge and at the slat trailing edge both have a peak at $f = 2.3$ kHz. The frequency of vortex shedding from the main-element leading edge appears to lock onto the second harmonic frequency of the vortex shedding from the slat cusp. Close scrutiny of the time sequence of vorticity in Figure 4.13 shows that the formation and shedding of vortices at the main-element leading edge coincides with the passage of vortices that originate from the slat cusp.

The flow separation at the main-element when the spoiler is deployed is also observed in the simulations using the coarse and medium grids. Flow separation at the main-element leading edge for a three element wing without the spoiler was previously reported by Terracol *et al.* [59]. They performed a hybrid RANS/LES simulation of the flow around a 3D high-lift model. The hybrid RANS/LES computation captured the presence of a separation bubble at the leading edge of the main-element, which caused a small loss of lift. Corresponding RANS simulations were unable to capture the presence of the separation bubble at the

leading edge of the main-element. They attributed the difference in the flow field to the different turbulence models used. Further validation of the observed flow dynamics in the current work through experimental methods using PIV measurement technique would help shed more light on the flow phenomenon at the main-element leading edge.

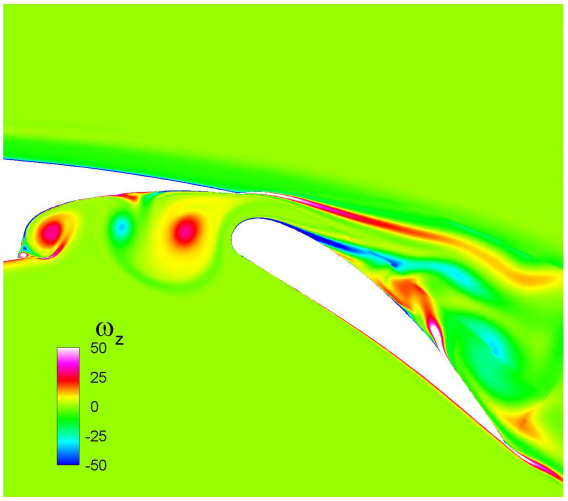


(a) Conventional configuration.

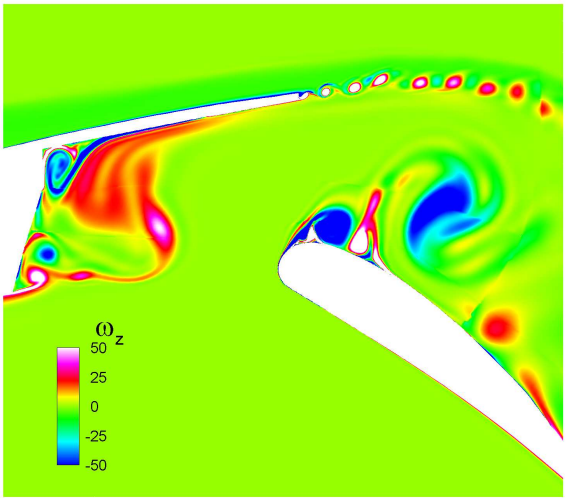


(b) Steep configuration.

FIGURE 4.16: Instantaneous non-dimensional spanwise vorticity field around the flap and spoiler.

The instantaneous spanwise vorticity, $\omega_z C/U$, around the flap for the conventional and steep HLDs is shown in Figures 4.16(a) and 4.16(b) respectively. Deploying the spoiler increases the flap gap from 2.3% to 9.3% of the reference stowed chord. The gap between the main-element/spoiler and the flap leading edge acts to accelerate the flow over the flap surface and thus prevent flow separation. The smaller the gap

size, the more effective the boundary layer acceleration effect. Therefore, when the spoiler is deflected, the boundary layer is unable to overcome the adverse pressure gradient over the flap leading edge. As a result, flow separation occurs. The separated shear layer rolls up into large vortical structures on the flap suction surface. For the conventional high-lift configuration, flow acceleration through the small gap re-energises the boundary layer, therefore the flow remains attached over the flap leading edge and separates further downstream along the flap at approximately 50% of the flap chord.

Figure 4.16(b) captures the roll-up and subsequent formation of large vortical structures from the free shear layer that separates from the flap leading edge. Figure 4.16(a) shows the formation of smaller vortical structures near the flap trailing edge. Pressure monitors are positioned downstream of the flap to measure the pressure fluctuations in the wake of the HLDs. The vortex shedding frequency from the flap for the conventional high-lift configuration occurs at a frequency $f = 103$ Hz, whereas the frequency of vortex shedding from the flap when the spoiler is deployed is $f = 52$ Hz. The corresponding non-dimensional frequency of the vortex shedding from the flap for the conventional and steep configuration is $St = 0.32$ and $St = 0.16$, where $St = fC_{flap}/U_\infty$ and $C_{flap}$ is the flap chord length. The frequency of vortex shedding from the flap matches the frequency of lift and drag fluctuations. This shows that the vortex shedding from the flap causes the lift and drag to fluctuate at the same frequency over the entire HLD.

Figure 4.16(b) also captures the shedding of vortices at the spoiler trailing edge. The vortex shedding occurs at a frequency $f = 4.3$ kHz, which corresponds to a Strouhal number of $St = 0.16$ based on the spoiler trailing edge thickness. The fact that the Strouhal frequency of the vortex shedding from the spoiler and flap agrees shows that there is a link between the unstead flow dynamics that the spoiler trailing edge and the global flow dynamics downstream of the flap.

Figure 4.17 shows the power spectra at the pressure probes located around the flap. The location of the probes are shown in Figure 4.17(a). Figure 4.17(b) shows that the probe at the spoiler trailing edge has a broadband peak centered at $f = 4.3$ kHz which is due to the vortex shedding. The power spectrum at the flap trailing edge shows that deploying the spoiler reduces the vortex shedding frequency behind the HLDs by a factor of 2 (from $f = 103$ Hz to $f = 52$ Hz).

A time sequence of the instantaneous spanwise vorticity field around the flap without the spoiler is shown in Figure 4.18. There is vortex shedding from the flap cove region into the gap between the main-element trailing edge and the flap.

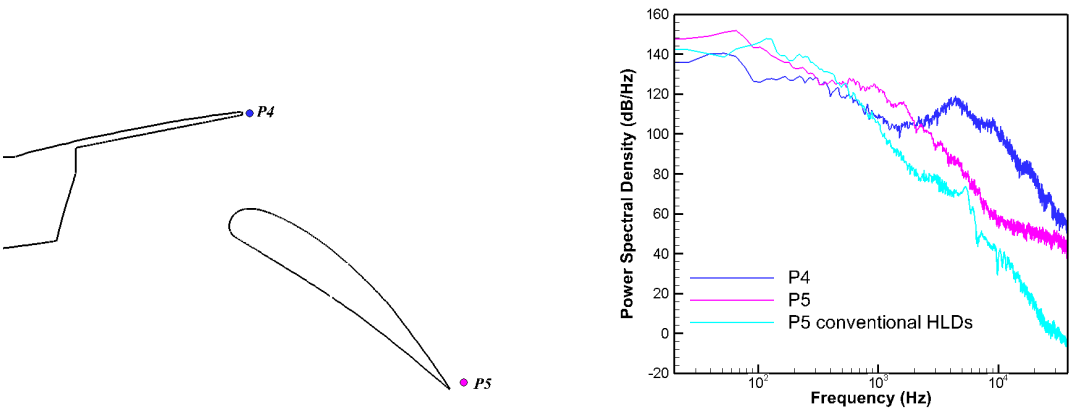


(a) Location of the pressure probes.

(b) PSD of the pressure probes.

FIGURE 4.17: The PSD of the pressure probes around the flap region.

The flap cove vortex grows in size with the addition of a separated shear layer from the flap cusp until later it sheds a large vortex downstream into the flap gap. The shedding of coherent vortices from the flap cove of a three-element high-lift aerofoil has been previously reported by Takeda *et al.* [70]. They preformed Laser Doppler Anemometry (LDA) and Particle Image Velocimetry (PIV) measurements of the flow around the flap cove.

Figure 4.19 shows a time sequence of the instantaneous spanwise vorticity field around the flap with the spoiler deployed. The shear layer that separates from the flap cusp rolls into large discrete vortical structures in the flap cove. The vortices, that are ejected from the flap cove recirculation, impinge on the lower surface of the spoiler and travel along the surface towards the spoiler trailing edge. The vortices impinging on the lower surface of the spoiler are a potential source of noise.

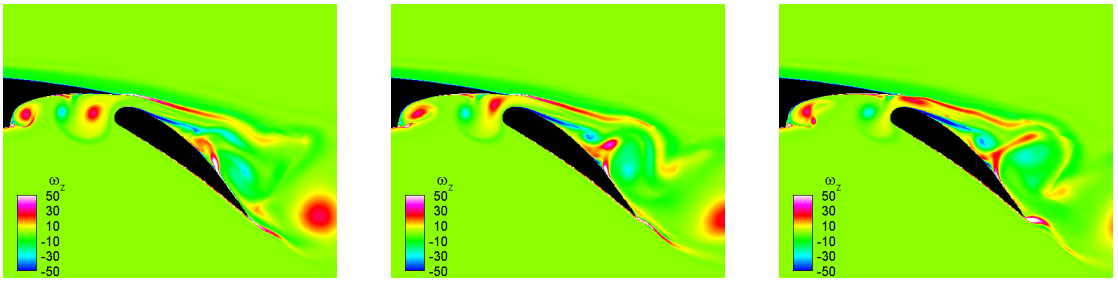

(a) (b) (c)

FIGURE 4.18: Time series of spanwise vorticity field around the flap without the spoiler.

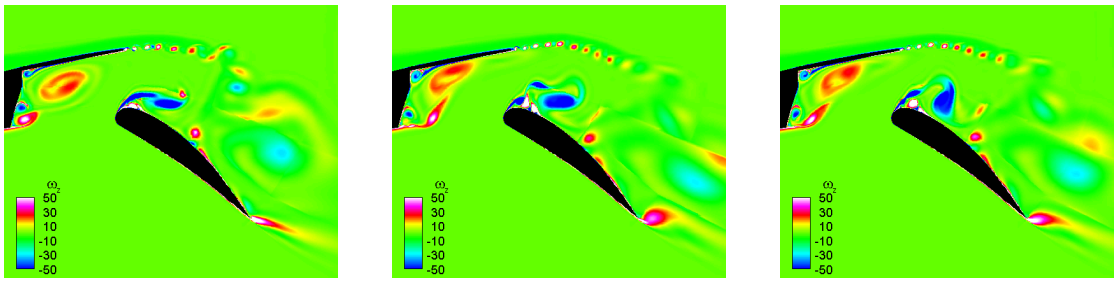


(a) (b) (c)

FIGURE 4.19: Time series of spanwise vorticity field around the flap with the spoiler deployed.

## 4.4 Acoustic Field

This section presents the results of the near-field and far-field noise radiation from the conventional and steep HLDs. Insights into the characterists of the far-field noise are provided by careful analysis of the near-field noise propagation.

### 4.4.1 Near-field Noise Propagation

In order to show the detail of the noise radiation in the near-field, the contours of the dilatation field are plotted around the HLDs. According to the continuity equation, dilatation is the time rate of change of density (or pressure in an isentropic acoustic field), $\nabla \cdot \mathrm{U} = \left(\frac{\partial u}{\partial x} + \frac{\partial v}{\partial y}\right)$. Thus contours of dilatation are suitable for showing acoustic wave propagation. The near-field noise radiation around the conventional and steep HLDs is shown in Figures 4.20(a) and 4.20(b) respectively.

Figure 4.20(a) shows the noise radiation from the conventional high-lift configuration. The acoustic wave pattern clearly shows that the noise originates from the slat region. A close look at the time sequence of dilatation plots around the slat region, in Figure 4.21, shows that the noise radiates from the slat trailing edge. The sequence of Figures 4.21(a) to 4.21(c) shows the acoustic waves traveling through the slat cove and over the slat suction surface. In Figures 4.21(b) and 4.21(c), the waves can be seen diffracting around the slat cusp. The acoustic wave generation coincides with the passage of turbulent structures into the slat gap. The turbulent structures originate upstream from the shear layer that separated from the slat cusp. The structures impinge onto the slat reattachment point on the slat lower surface before traveling past the trailing edge. The noise is generated when the turbulent structures are scattered by the slat sharp trailing edge.

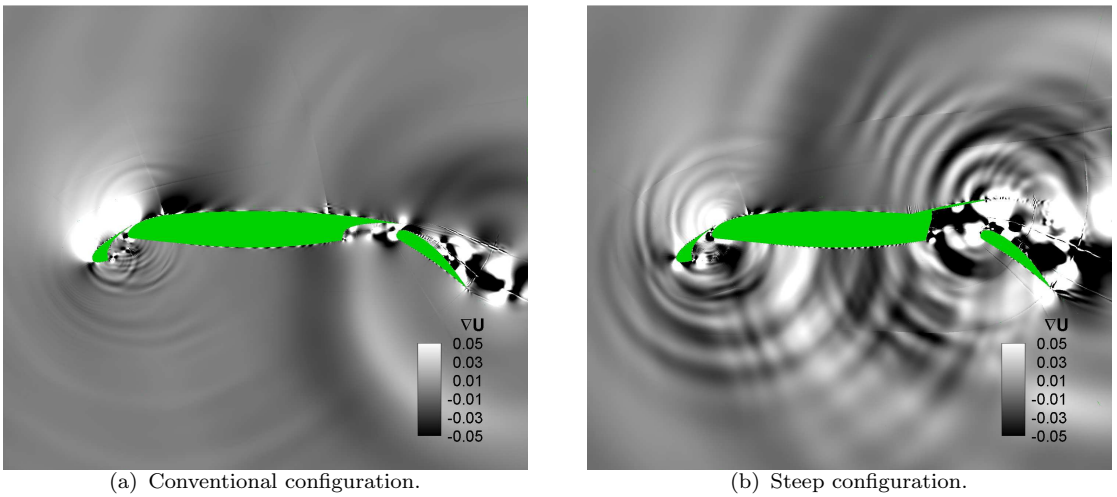


(a) Conventional configuration. (b) Steep configuration.

FIGURE 4.20: Instantaneous dilatation field around the HLDs (lighter contours: $\nabla \cdot \mathrm{U} = -0.05$ and darker contours: $\nabla \cdot \mathrm{U} = +0.05$).

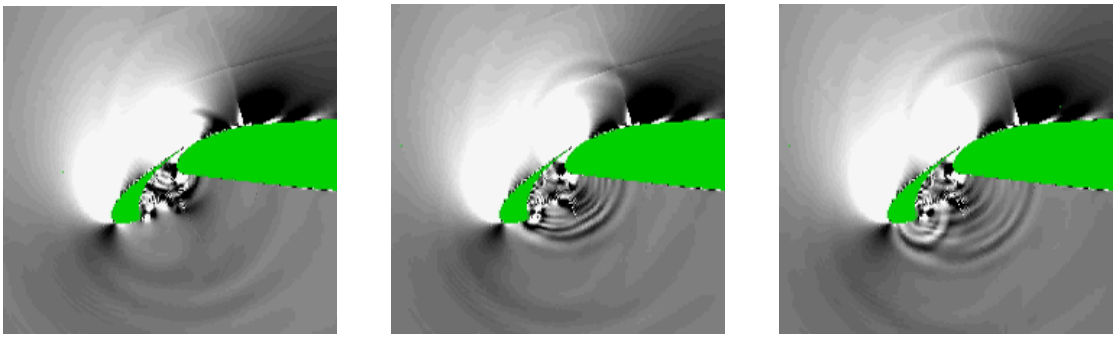

(a) (b) (c)

FIGURE 4.21: Sequence of instantaneous dilatation field around the slat in conventional HLD configuration (lighter contours: $\nabla \cdot \mathrm{U} = -0.05$ and darker contours: $\nabla \cdot \mathrm{U} = +0.05$).

The noise radiation from the steep high-lift configuration is shown in Figure 4.20(b). The wave pattern shows that the noise originates from the slat, spoiler and the flap. The slat noise radiation is increased significantly when the spoiler is deflected. Figure 4.22 shows a time sequence of snapshots of the dilatation field around the slat. The sequence of snapshots clearly shows acoustic waves generated at the slat trailing edge traveling over the slat suction surface upstream towards the slat leading edge. At the same time, the acoustic waves generated at the slat trailing edge travel through the slat cove and over the main-element leading edge surface. The time sequence of dilatation field plots in Figure 4.22 clearly show that the source of the noise from the slat is at the slat trailing edge. The noise appears to be generated by the interaction of the edge with the vortices shed from the separation bubble at the main-element leading edge.

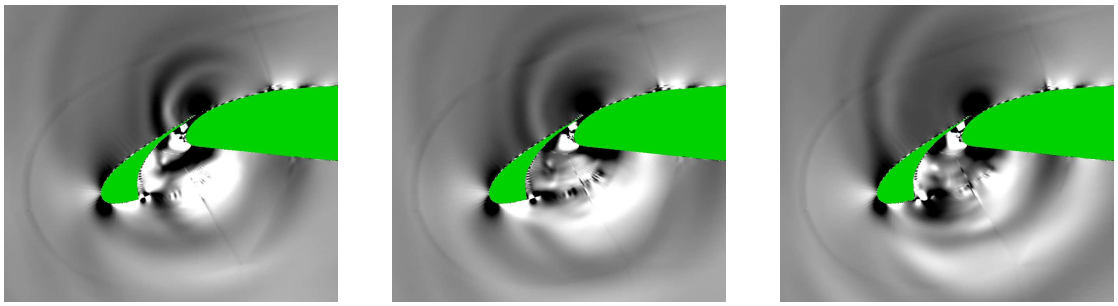

(a) (b) (c)

FIGURE 4.22: Sequence of instantaneous dilatation field around the slat in steep HLD configuration (lighter contours: $\nabla \cdot \mathrm{U} = -0.05$ and darker contours: $\nabla \cdot \mathrm{U} = +0.05$).

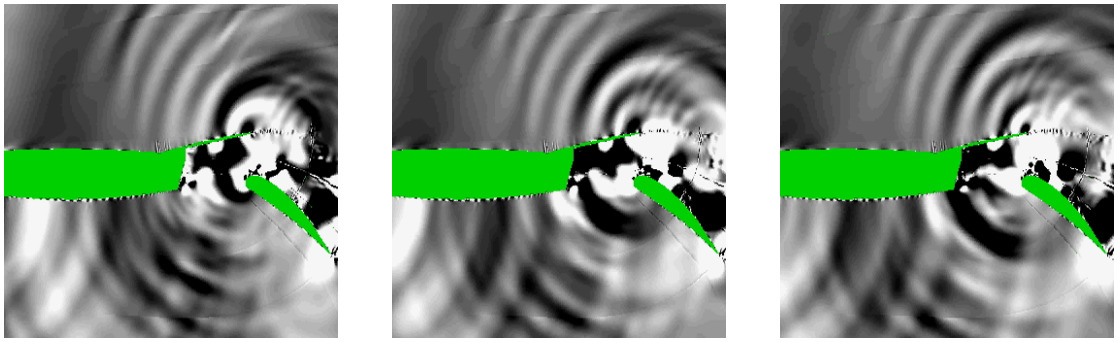

(a) (b) (c)

FIGURE 4.23: Sequence of instantaneous dilatation field around the flap region in steep HLD configuration (lighter contours: $\nabla \cdot \mathrm{U} = -0.05$ and darker contours: $\nabla \cdot \mathrm{U} = +0.05$).

Figure 4.23 shows a time sequence of dilatation contours around the flap region. The spoiler trailing edge is clearly a significant source of noise for the steep configuration. The noise from the spoiler trailing edge is observed to radiate downwards through the flap cove region towards the ground, therefore it is likely to contribute to an increase in the noise for observers at the overhead position. The noise radiation occurs simultaneously with the shedding of vortices from the spoiler trailing edge, confirming that this is the noise generation mechanism.

### 4.4.2 Far-field Noise Radiation

An integral solution of the FW-H equation is used to compute the far-field noise from the HLDs. The unsteady flow data is collected on the solid surface of the HLDs, hereon referred to as the *solid-body* integration surface, and on a permeable surface away from the solid surface of the HLDs, referred to as the *off-body*

integration surface.

The flow data is sampled on the surfaces after 23 flow-through of the reference stowed chord to allow the initial transient flow solution to wash out. The flow data is then sampled every 80 time steps, which corresponds to a sampling rate of 43 kHz based on a time step $\Delta t = 2.907 \times 10^{-7}$ seconds. The sampling rate yields a Nyquist frequency of $f_{max} = 21.5$ kHz. The sampling rate is chosen in order to focus the noise analysis on the range of frequencies that correspond to full scale aircraft noise ($20 < f < 20,000$ Hz). The effect of aliasing of high frequency features onto the low frequencies due to the chosen sampling rate is not investigated.

In total 10,000 samples are collected, which are divided into 3 blocks of 4096 samples each with a 50% overlap. The sample block size yields a frequency resolution of 10.5 Hz. A Hanning windowing function is used on each block before performing a Fast Fourier Transform (FFT). The results from the three blocks are averaged to obtain the far-field noise spectrum.

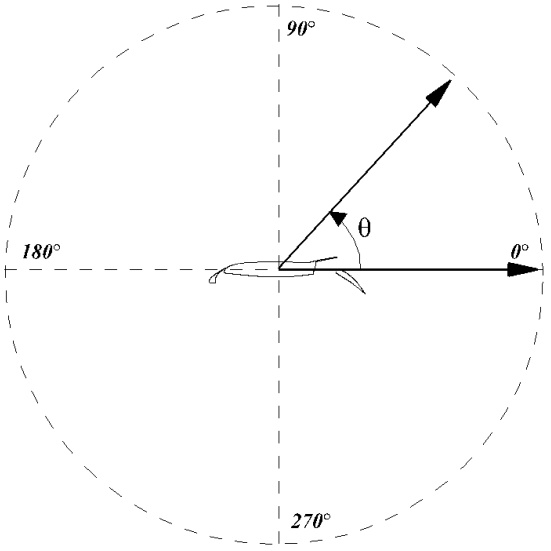


FIGURE 4.24: Definition of observer angle with respect to the HLD configuration.

The FW-H solver used in the current work requires 3D flow field data as input to compute the far-field noise. Therefore in order to compute the noise from a 2D simulation, the integration surfaces are extruded in the spanwise direction. The assumption is made that the flow is perfectly correlated over the chosen spanwise length. The predicted far-field pressure depends on the spanwise length of the FW-H integration surfaces. The spanwise extent of the 2D FW-H surfaces is set

to $0.15C$ based on the spanwise correlation measurements of Takeda *et al.* [16].

Observers are located on a circle of radius 100 chord lengths centered at the origin $(x, y) = (0, 0)$ in the frame of reference of the high-lift model. Each observer location is described by an observer angle, $\theta$, that is defined as shown in Figure 4.24.

Figure 4.25 compares the FW-H results obtained using a closed off-body FW-H surface with the solid-body FW-H surface. The position of the permeable surface in relation to the HLDs is shown in Figure 4.26(a). There are significant differences in both amplitude and directivity of the far-field pressure obtained using the off-body and the solid-body integration surfaces. There is a significant increase in noise in the downstream direction where the wake of the HLDs passes through the FW-H surface. A large peak in noise level is also observed in the upstream direction between observer angles 90 to 180 degrees. The far-field noise level from the solid-body FW-H surface is higher than that from the off-body FW-H surface for observer angles 210 to 260 degrees.

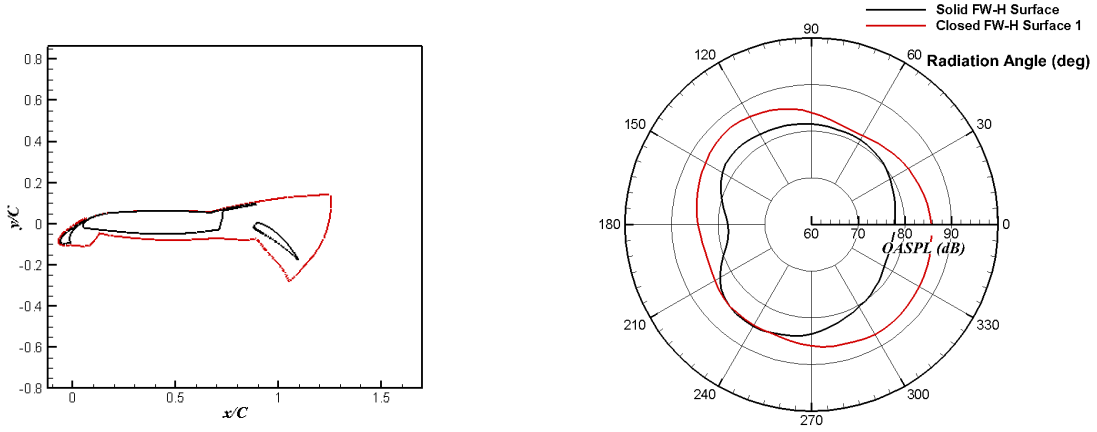


(a) Closed FW-H surface.

(b) Far-field acoustic signal from closed FW-H surface.

FIGURE 4.25: Comparison of the far-field noise from the closed off-body FW-H surfaces with the solid-body FW-H surface.

In order to reduce the impact of the wake passing through the off-body FW-H surface, the section of the surface in the wake is moved one chord length downstream, see Figure 4.26(a). Figure 4.26(b) shows that there are still significant differences in amplitude and directivity of the predicted far-field pressure. The disagreement between the far-field noise prediction from the off-body integration surface and the solid-body integration surface has previously been found by Casper et al [71]. They found that the wake passing through the off-body permeable

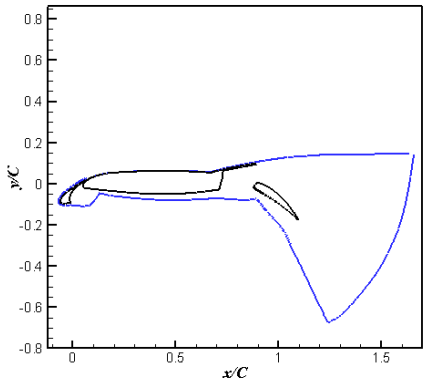


(a) Position of the off-body FW-H surface.

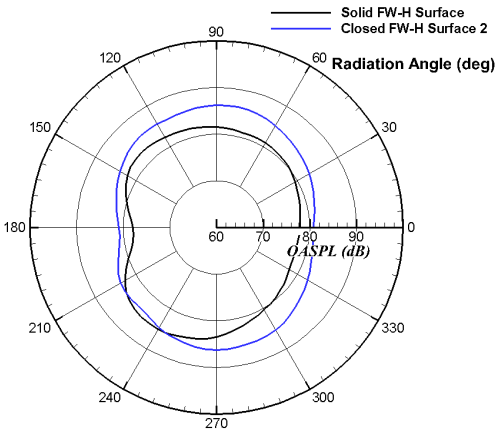


(b) Far-field pressure.

FIGURE 4.26: Comparison of the far-field noise from the closed off-body FW-H surfaces with the solid-body FW-H surface.

integration surface introduced errors in the far-field noise predictions.

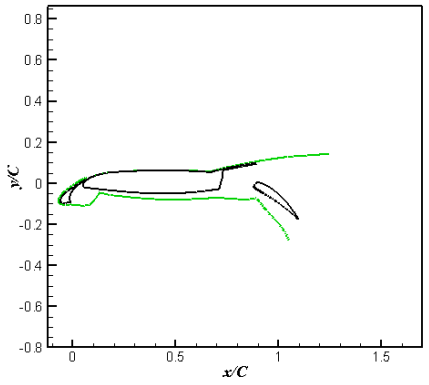


(a) Open FW-H surface.

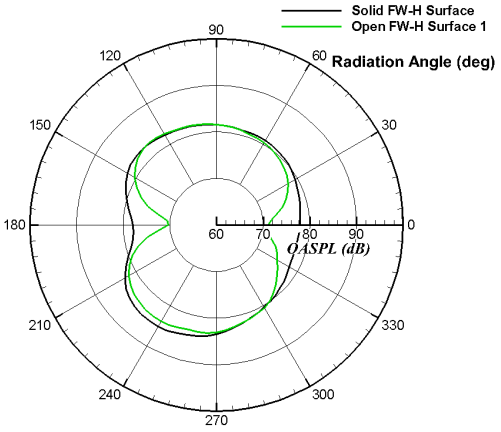


(b) Far-field acoustic signal from open FW-H surface.

FIGURE 4.27: Comparison of the far-field noise from the open off-body FW-H surfaces with the solid-body FW-H surface.

In order to eliminate the effects of the wake passing through the off-body FW-H surface, an open off-body integration surface is constructed by removing the section of the closed surface in Figure 4.25(a) that cuts through the wake of the wing. Figure 4.27 shows the comparison of the noise from the open off-body FW-H surface with the solid-body FW-H surface. When the downstream section of the off-body FW-H surface is removed, both the upstream and downstream noise peaks disappear. Figure 4.27(b) represents an improvement over the results from the closed off-body FW-H surface in Figure 4.25(b). However, using an open permeable FW-H surface leads to an underprediction in the upstream and

downstream direction. The results show that the position of the permeable FW-H integration surface has a significant effect on the predicted far-field noise level and directivity. Further work is required to mitigate the effects of the wake through a permeable surface. The results presented in this section are based on the solid-body FW-H surface only.

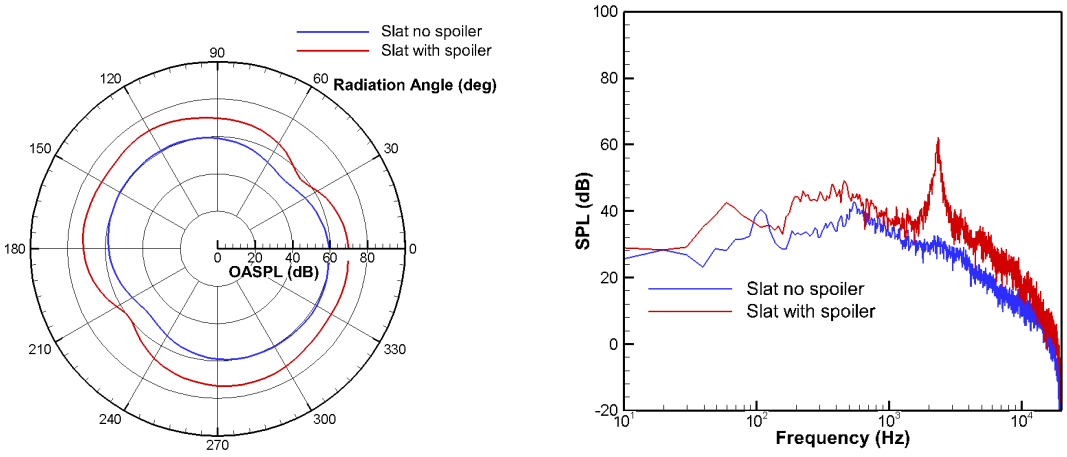


(a) Overall far-field noise directivity.

(b) Far-field noise spectra at $\theta = 270$ degrees.

FIGURE 4.28: Comparison of the far-field noise directivity and spectrum from the slat for observers at 100 chord length away.

The far-field slat noise directivity and spectra for the conventional and steep HLDs are presented in Figures 4.28. The slat far-field noise directivity resembles a dipole far-field noise pattern with the maximum noise radiation in the direction perpendicular to the slat chord. The maximum noise radiation is in the rearward direction to the flight trajectory. Similar noise directivity patterns are reported by Khorrami and Lockard [23]. Dobrzynski and Pott-Pollenske [11] also found that the slat noise directivity peaked in the rearward direction. Deploying the spoiler increases the slat noise level for all observer angles. Figure 4.28(b) compares the conventional and steep slat noise spectra at the overhead position. Deflecting the spoiler increases the noise for most frequencies. When the spoiler is deployed a noise peak appears at $f = 2.3$ kHz. The frequency of noise peak is close to the frequency of vortex shedding from the main-element leading edge separation bubble $f = 2.5$ kHz. The near-field dilatation plot shows that the noise originates from the interaction of vortices from the main-element leading edge with the slat trailing edge. There is another noise peak at $f = 52$ Hz which corresponds to the frequency of the vortex shedding from behind the flap and the spoiler. When the spoiler is retracted, the slat noise spectra has a peak at $f = 100$ Hz, which matches the frequency of the vortex shedding from the flap.

Figure 4.29 shows the noise directivity and far-field spectra from the main-element (including the spoiler). The main-element noise spectra when the spoiler is deployed has similar tonal noise components at $f = 52$ Hz and $f = 2.3$ kHz as the slat noise spectra (see Figure 4.28(b)). The fact that the main-element noise spectra has a noise peak at $f = 2.3$ kHz confirms that the source of the noise at this frequency is common to both the slat and the main-element. In addition to the two noise peaks, there is a narrowband noise hump centered at $f = 4.4$ kHz. The frequency is very close to the vortex shedding frequency from the spoiler trailing edge $f = 4.3$ kHz.

Figure 4.30 shows the dilatation level along a line AB. The wavelength of the noise radiating from the spoiler can be approximated to $\lambda \approx 0.07$ m. The wavelength corresponds to an acoustic frequency of $f = c_\infty/\lambda \approx 4.7$ kHz.

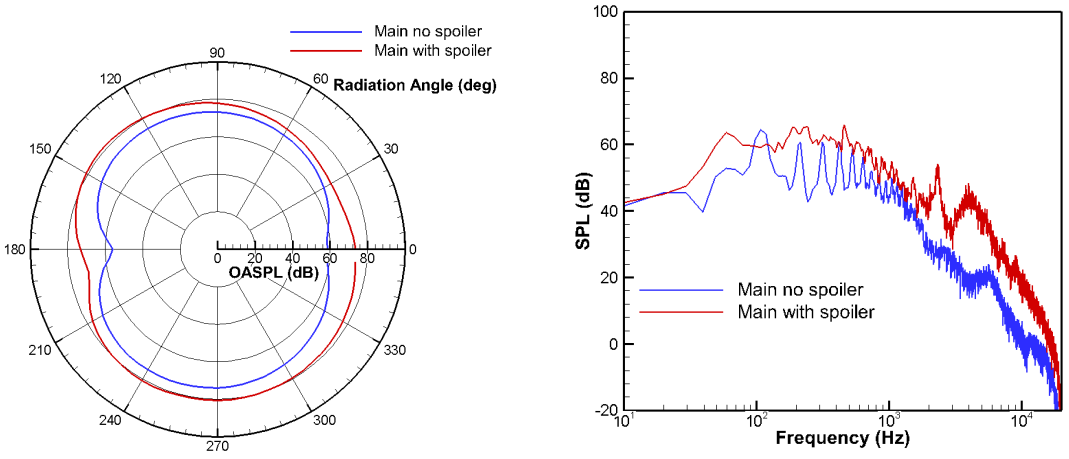


(a) Overall far-field noise directivity.

(b) Far-field noise spectra at $\theta = 270$ degrees.

FIGURE 4.29: Comparison of the far-field noise directivity and spectrum from the main-element for observers at 100 chord length away.

Figure 4.31(a) shows that deploying the spoiler increases the noise from the flap for all observer angles. The flap noise spectrum at $\theta = 270$ degrees is shown in Figure 4.31(b). The flap noise increases for all frequencies when the spoiler is deployed. The flap noise peaks at $f = 4.4$ kHz, similar to the peak found in the main-element spectra. The near-field dilatation plot showed that the sound waves radiating from the spoiler trailing edge travel over the flap and main-element surfaces.

Figure 4.32(a) shows a comparison of the overall far-field noise directivity from conventional and steep HLDs. Deploying the spoiler results in a noise level increase for all observer angles. Figure 4.32(b) compares the far-field noise spectra from the conventional and steep HLDs for an observer at the overhead position $\theta = 270$

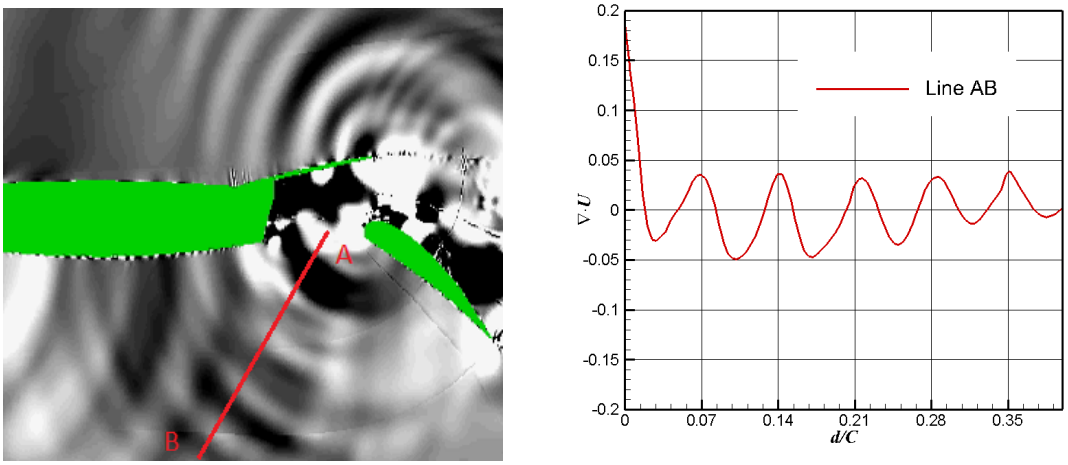


(a) Dilatation field around the steep spoiler and flap

(b) Dilatation amplitude along the line AB.

FIGURE 4.30: Estimation of the acoustic wavelength of the noise radiating from the spoiler trailing edge.

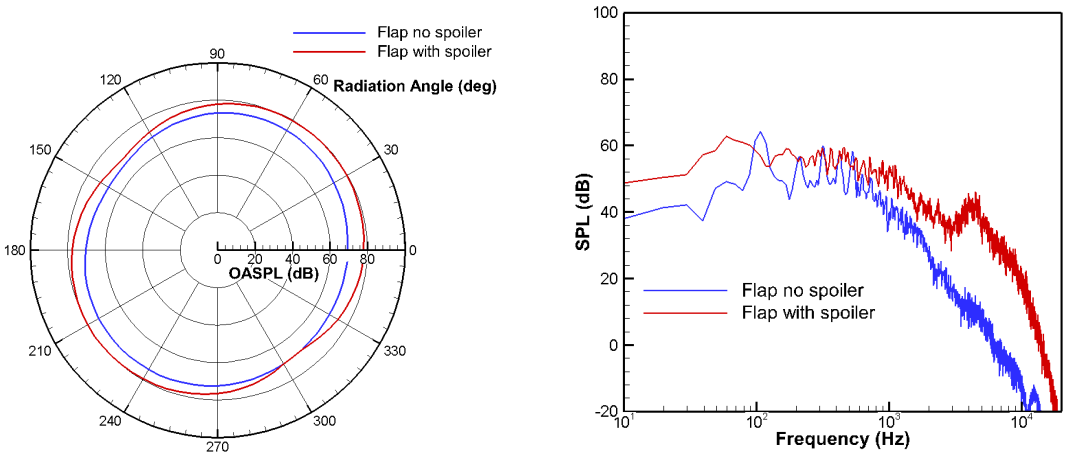


(a) Overall far-field noise directivity.

(b) Far-field noise spectra at $\theta = 270$ degrees.

FIGURE 4.31: Far-field noise directivity and spectrum for the flap for observers at 100 chord length away.

degrees. Deflecting the spoiler increases the noise level for all frequencies. When the spoiler is deployed the noise spectrum from the HLDs has noise peaks at: $f = 52$ Hz due to the vortex shedding from behind the flap; $f = 2.3$ kHz due to the vortices from the main-element interacting with the slat trailing edge; and $f = 4.4$ kHz due to the vortex shedding from the spoiler trailing edge. The noise spectrum from the conventional HLDs has a fundamental peak at $f = 100$ Hz and 4 sub-harmonic peaks.

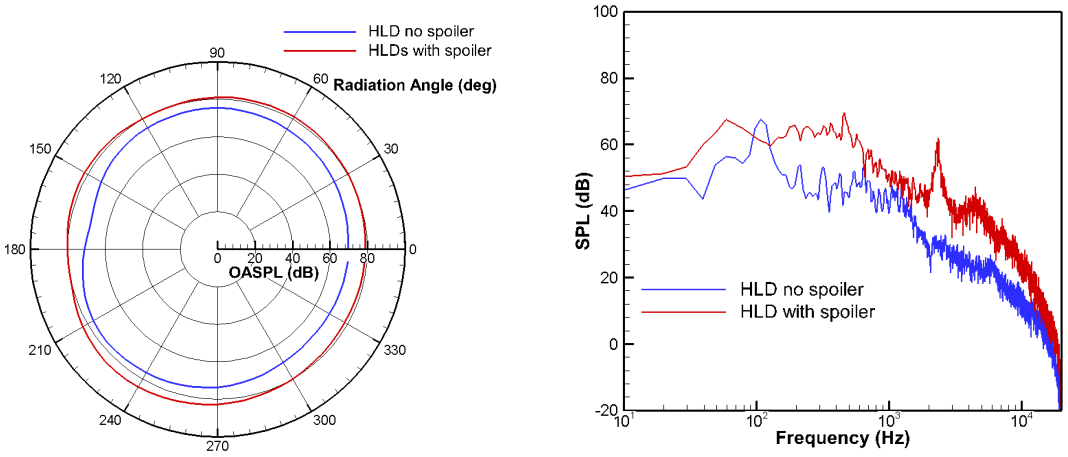


(a) Overall far-field noise directivity.

(b) Far-field noise spectra at $\theta = 270$ degrees.

FIGURE 4.32: Comparison of the far-field noise directivity and spectrum from the HLDs for observers at 100 chord length away.

## 4.5 Summary

Simulations of the flow around the 2D conventional and steep HLDs have been performed using SotonCAA. The unsteady flow field is used to calculate the far-field noise using an integral solution of the FW-H equation. The resulting flow field and acoustic field has shown the effects the spoiler has on the aerodynamics and acoustics of the HLDs.

The flow field results show that deploying the spoiler causes a reduction in circulation around the HLDs. Deflecting the spoiler reduces the lift by approximately one half and increases the drag by a factor of 2. The fluctuations in lift and drag increase when the spoiler is deployed due to the shedding of large vortical structures behind the flap. The flow separates at the flap leading edge when the spoiler is deployed.

In the absence of the spoiler, flow separation is delayed and occurs near the mid-chord of the flap. Deploying the spoiler reduces the frequency of the vortex shedding from the behind the flap from $f = 100$ Hz to $f = 52$ Hz. The frequency of vortex shedding correspond to $St = 0.32$ and $St = 0.16$ based on the flap chord length. The far-field noise from the conventional and steep HLDs have peaks at same frequencies which is a result of the vortex shedding.

On the slat, the incoming flow incidence at the slat leading edge is reduced, causing an expansion of the slat cove vortex. The larger slat cove vortex pushes the stagnation point on the main-element further downstream. The flow separates

from the main-element leading edge on the suction surface and sheds vortices into the gap between the main-element and the slat trailing edge. Contours of dilatation show that the interaction of the turbulent structures originating from the main-element separation bubble with the slat trailing edge is responsible for the generation of noise from the slat when the spoiler is deployed.

The dilatation contours show that noise from the slat trailing edge travels through the slat cove and over the slat suction surface. The far-field noise from the slat when the spoiler is deployed has a tonal peak at $f = 2.3$ kHz ($St = 3.6$ based on the slat chord length). This frequency agrees very well with the frequency of the vortex shedding from the main-element separation bubble. The frequency of vortex shedding from the main-element leading edge is linked to the frequency of vortex shedding from the slat cusp. The vortices from the slat cusp caused the shedding of vortices as they passed close to the main-element leading edge. The vortex shedding from the slat cusp occurs at a frequency of equal $f = 1.1$ kHz ($St = 1.7$), which is approximately half the vortex shedding frequency from the main-element leading edge.

At the spoiler trailing edge, the flow separates due to the discontinuity of the spoiler surface. The separated shear layer at the spoiler trailing edge sheds vortices at a frequency of $f = 4.3$ kHz ($St = 0.16$ based on the blunt spoiler trailing edge thickness). The far-field noise spectrum from the steep HLDs has a peak at $f = 4.4$ kHz that is due to the vortex shedding from the spoiler trailing edge.

Results of far-field noise directivity show that the overall noise level increases for all observer angles when the spoiler is deflected. The maximum overall noise increase occurs at a frequency of $f = 52$ Hz ($St = 0.16$ based on the flap chord length), which corresponds to the vortex shedding from behind the flap and spoiler. The spoiler also contributes to tonal noise components, due to the vortex shedding from the separation bubble at the main-element leading edge and due to the vortex shedding from the spoiler trailing edge

The current 2D simulations do not capture the variation of the flow field in the spanwise direction. In the next chapter, 3D simulations are performed to take into account the effects of the spanwise flow on the far-field noise. The simulations also serve to confirm the results obtained from the current 2D simulations.

# Chapter 5

# 3D Simulation of High-Lift Devices

## 5.1 Introduction

In this Chapter the results of the 3D simulations of flow around the conventional and steep HLDs are presented and discussed. The 3D simulations improve upon the results from the 2D simulations of Chapter 4. Simulations of 2D flow around HLDs have been shown to predict excessively energetic vorticity structures compared to measurements from PIV [20]. The 3D simulations take into account the effects of the three-dimensionality of the local turbulent flow field around the HLDs, therefore improving the far-field acoustic noise prediction. The DES turbulence model is used to model the effect of turbulence in the 3D simulations. The choice of DES turbulence model is driven by the low computational cost in comparison to LES. DES employs a RANS model near the wall, thus avoiding the excessively fine grids required by LES. Away from the wall, a fine grid spacing is employed that provides better resolution of turbulent structures in comparison to a URANS simulation.

## 5.2 Geometry and Flow Conditions

The high-lift geometry used in the DES simulation is based on the 2D geometry presented in Chapter 4. The conventional and steep HLDs consist of a slat with a chord of 12% of the model stowed chord, a flap with a chord of 25% of the model

stowed chord and a main-element. The deflection angle for the slat and flap is 30 and 38 degrees respectively. The steep high-lift configuration has a spoiler of length $11\%C$, deployed at an angle of 20 degrees.

The current 3D simulations employ the same freestream conditions as used in the 2D simulations, Mach number $M = 0.235$, which corresponds to a Reynolds number $Re = 5.4 \times 10^6$ (based on the model stowed chord) and a 5 degrees angle of attack.

### 5.2.1 3D Grid of HLD with a Full Span Spoiler

The 3D grids are generated by uniformly extruding the respective 2D grid profile along the spanwise ($z$) direction. The 2D grids are based on the grids presented in Chapter 4. However, in order to maintain manageable grid sizes, the number of grid points is reduced away from the important regions of interest. The details of the grids for the conventional and steep HLDs are summarised in Table 5.1. According to Rumsey and Ying [72] a minimum of $5 \times 10^5$ grid points are required for accurate prediction of surface pressures and $1 \times 10^5$ to $2 \times 10^5$ grid points for accurate prediction of velocity profiles using steady RANS computations [72]. The 2D grid profiles consist of approximately $2.6 \times 10^5$ grid points for both conventional and steep HLDs.

The spanwise width of the computational domain is chosen based on measurements by Takeda et al [16]. They found that the spanwise correlation length on a 1/5th scale National High-Lift (NHL) model is 15% of the model chord length. The spanwise length is divided into 62 grid points, which results in a uniform spanwise grid spacing of $\Delta z = 0.0025C$.

In the LES region, the streamwise spacing $\Delta x$ is close to $\Delta z$ as recommended by Spalart [58]. The total grid points for the 3D grids are 16.25 and 16.28 million for the conventional and steep HLD configuration respectively. A fully comprehensive grid-convergence study is not feasible for the 3D time accurate simulations of the HLDs. The high computational expenses of such a grid-convergence study is too prohibitive, due to the large grid sizes required coupled with the necessity to simulate the flow for a longer time period for statistical convergence.

Following the recommendation of Spalart [58], in the boundary layer region the grids are designed to ensure $y^+ \approx 1$ along the solid walls and at least the first 25 points are located inside the boundary layer. Figure 5.2 compares the boundary

TABLE 5.1: Grid details for DES simulations

| Config. | 2D grid size | Spanwise grid points | Total grid points |
|---|---|---|---|
| Conventional | 262,068 | 62 | $16.25 \times 10^6$ |
| Steep | 262,568 | 62 | $16.28 \times 10^6$ |

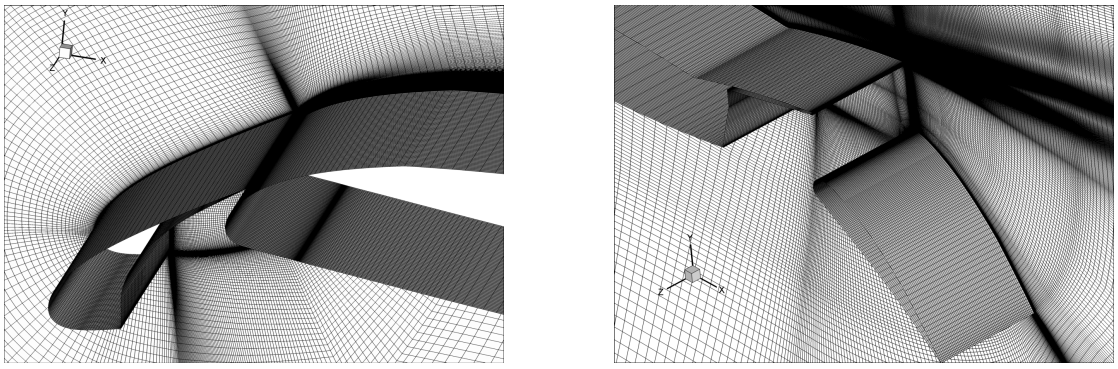

(a) Slat. (b) Spoiler and flap.

FIGURE 5.1: Grid distribution in the vicinity of the slat and the spoiler.

layer velocity profile at a station, $x/C = 0.49$ on the suction surface of the main-element on the steep high-lift configuration with the velocity profile in the viscous sublayer and the log law region of a turbulent boundary layer. The computed velocity profile agrees reasonably well with the turbulent boundary layer velocity profile for a flat plate. The early departure of the computational velocity profile from the log-law line can be attributed to the adverse pressure gradient created by the deflected spoiler.

#### 5.2.1.1 Simulation Methodology

The simulation methodology employed in the 2D simulations is also used for the 3D simulations. The high-order solver SotonCAA is used to perform the flow computations. The $4^{\text{th}}$-order optimised prefactored compact scheme of Ashcroft and Zhang [50] is used for spatial discretisation whereas the $2^{\text{nd}}$-order implicit temporal integration with Newton-like sub-iterations [73] is used for time integration. The simulations require 5 sub-iterations to drop the residuals by two orders of magnitude at each time step.

The simulations employ explicit buffer zone boundary conditions [69] at the computational domain extents. Details of the implementation of the buffer zone are outlined in Section 3.2.6 of Chapter 3. The explicit buffer zone is

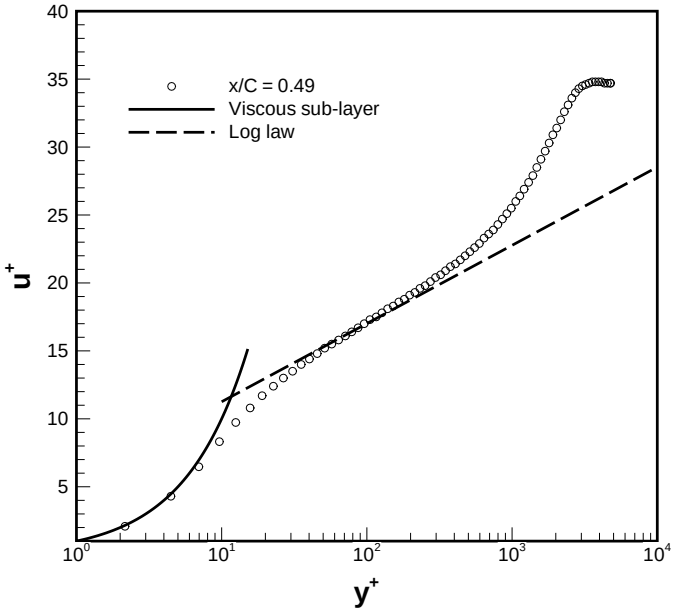


FIGURE 5.2: Turbulent boundary layer velocity profile at $x/C = 0.49$ on the suction surface of the main-element on the steep high-lift configuration.

applied in a zone 20 grid points wide from the streamwise computational domain extents. The damping coefficients are set to $\sigma = 1.0$ and $\beta = 3.0$ as in the 2D simulations. In addition to the explicit buffer zone boundary conditions, grid stretching is employed close to the computational domain extent to eliminate any acoustic reflections. Periodic boundary conditions are applied at the spanwise computational domain extent and the no-slip boundary conditions are imposed on the solid surfaces of the high-lift devices.

The effects of turbulence are modeled using the Delayed Detached Eddy Simulation(DDES) turbulence model. The turbulence model is based on the one-equation turbulence model of Spalart-Allmaras. The DDES formulation resolves the issues of Modeled-Stress Depletion and Grid-Induced Separation. The Delayed DES formulation along with the low-Reynolds number corrections of Spalart *et al.* [65] are implemented in SotonCAA by the author and used in the present simulations. DDES incorporates a function that 'shields' the boundary layer from the LES mode. A low-Reynolds number correction is employed to stop the premature activation of the wall proximity function in the S-A model equation as a result of the low eddy viscosity in LES mode.

The non-dimensional time step size is fixed to $\Delta t c_\infty / C = 1 \times 10^{-4}$ with 5 Newton-like sub-iterations, yielding a maximum local Courant-Friedrichs-Lewy(CFL)

number of 12.5 based on the acoustic velocity ($U_\infty + c_\infty$). The corresponding dimensional time step is $\Delta t = 2.94 \times 10^{-7}$ seconds, which is equivalent to a sampling frequency of 3.45 MHz, or a temporal resolution of 1000 time steps over one period of a 3.45 kHz signal. The flow-through time scale based on the stowed chord of the high-lift model and the freestream velocity corresponds to 43,100 time steps. The simulations are run over 10 flow-through time units to wash-out the transient feature and obtain a statistically convergent flow field.

The simulations are performed on the University of Southampton Iridis 3 High Performance Computing(HPC) cluster, using 96 Nehalem Intel 2.27GHz processors. The CPU cost per time step is 4 seconds. Approximately 60 hours (2.5 days) on 96 CPUs are required to compute one flow-through based on the stowed chord, $C = 1$ m. When taking into account the time taken for the job to queue on the HPC cluster, the total time taken to run one flow-through requires between 3 to 4 days to complete.

## 5.3 Aerodynamic Flow Field

This section presents the results of the 3D time averaged and instantaneous flow field around the conventional and steep HLDs. The results from the current 3D simulations are compared with the results from the 2D simulation from Chapter 4.

### 5.3.1 Aerodynamic Forces

Figure 5.3 shows the history of the lift and drag coefficient obtained from the 3D simulation of the two HLD configurations. Table 5.2 shows the comparison of the mean lift and drag coefficients from the 2D and 3D simulations. The percentage change in the value of $C_L$ and $C_D$ from 2D to 3D is shown in brackets. The $C_L$ and $C_D$ values obtained from the 3D simulations are up to 2.5% less than the 2D simulations. However, the difference in $C_L$ and $C_D$ between the conventional and steep HLDs is in good agreement. The 3D simulations predicts a 55% reduction in lift and a 95% increase in drag when the spoiler is deployed. The 2D simulations predicts a 55% reduction in lift and a 100% increase in drag when the spoiler is deflected.

Figure 5.4(a) compares the mean pressure distribution around the conventional

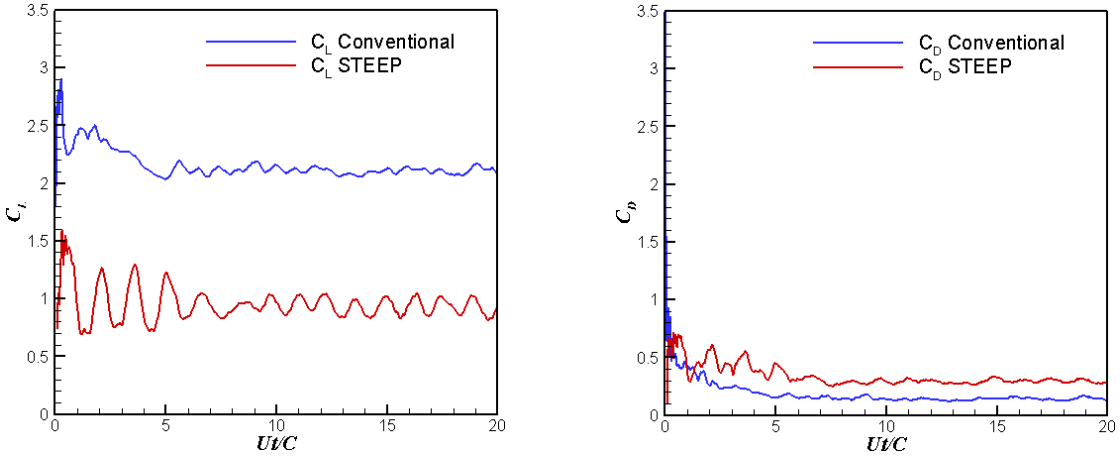


(a) Lift Coefficient.

(b) Drag Coefficient.

FIGURE 5.3: Convergence history of the lift and drag coefficient of the conventional and steep HLD configuration.

TABLE 5.2: Comparison of the aerodynamic coefficient of the 2D and 3D simulations.

| **Configuration** | $C_L$ | $C_D$ |
|---|---|---|
| 2D Conventional | 2.22 | 0.20 |
| 3D Conventional | 2.18 (-1.8%) | 0.20 (0%) |
| 2D Steep | 1.00 | 0.40 |
| 3D Steep | 0.98 (-2%) | 0.39 (-2.5%) |

HLDs obtained from the 2D and 3D simulations. The pressure coefficient from the 3D simulations are averaged in time as well as in space across the spanwise length of the model. Comparison of the pressures on the lower surface of the HLDs shows that the position of the stagnation points on the slat and the flap are in good agreement. However on the main-element, the stagnation point in the 3D simulation has moved downstream from $x/C = 0.09$ to $x/C = 0.11$.

The pressure over the upper surface of the HLDs obtained from the 3D simulations is reduced compared to the 2D simulations. The 3D simulation predicts lower pressure at the suction peak on all three elements compared to the 2D simulation. The reduction in the pressure on the suction surface of the HLDs may be attributed to the reduction in the grid resolution. Similar trends are observed in the 2D simulations presented in Figure 4.4. The 2D simulation on the coarse grids predicts a lower pressure on the suction surface in comparison to the 2D simulation on the fine grids. The 2D grid profiles used to generate the current 3D grids have approximately the same number of grid points as the 2D coarse grids ( $\approx 2.6 \times 10^5$

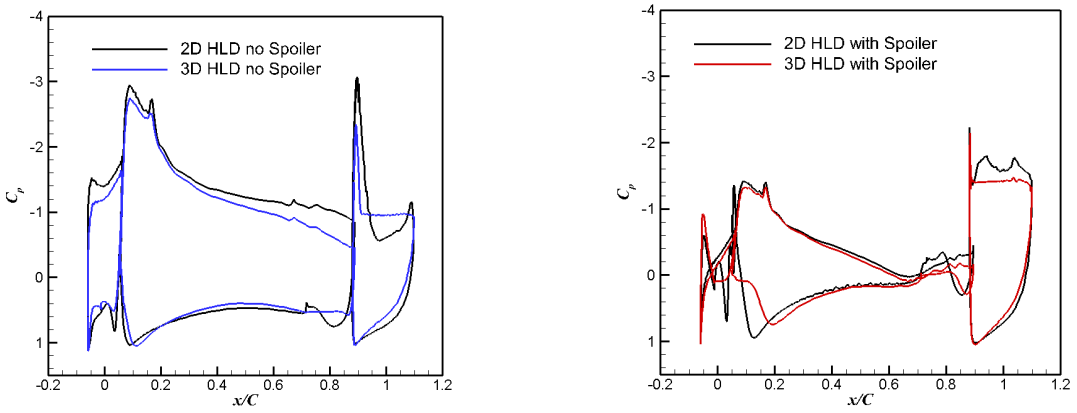


(a) Conventional HLDs.

(b) Steep HLDs.

FIGURE 5.4: Comparison of the pressure distribution obtained from the 2D and 3D simulations over the HLD configuration.

grid points). The lower grid resolution is used for the 3D grids in order to keep the computational requirements at a manageable level.

Figure 5.4(b) compares the pressure distribution over the 2D and 3D steep HLDs. The pressure on the upper surface of the HLDs is in reasonable agreement for all three elements. The 2D and 3D $C_p$ plots show that the stagnation point on the main-element is located at $x/C = 0.13$ and $x/C = 0.20$ respectively. The pressure at the main-element stagnation point in the 3D simulation reduced compared with the pressure predicted from the 2D simulation. Both the 2D and 3D simulations predict a $C_p < 1$ at the main-element stagnation position.

### 5.3.2 Time Averaged Flow Field

Figure 5.5 shows the comparison of the mean streamlines and velocity contours around the 2D and 3D slat for the conventional configurations. The 2D velocity field shows rapid flow acceleration over the slat suction surface compared with the 3D velocity field. The streamlines around the 3D slat leading edge show a reduced flow incidence compared to the flow field around the 2D slat.

Figure 5.6 compares the 2D and 3D mean flow field around the slat when the spoiler is deflected. Comparison of Figure 5.6(a) and 5.6(b) shows that the 3D mean flow stagnation point on the main-element is located further downstream in comparison to the 2D mean flow.

The 3D simulation does not predict the flow separation at the main-element leading

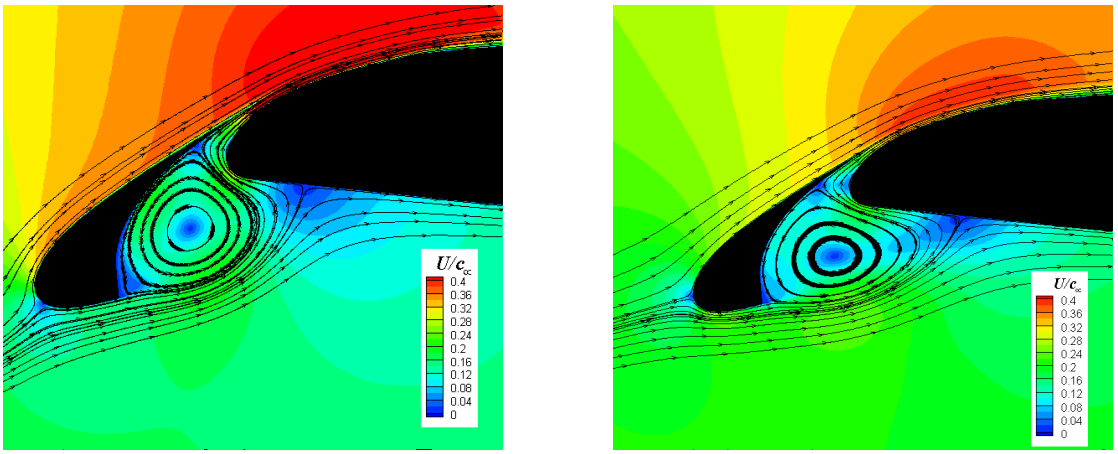


(a) 2D slat conventional configuration.

(b) 3D slat conventional configuration.

FIGURE 5.5: Mean velocity field and streamlines around the 2D and 3D slat without the spoiler.

edge, as predicted in the 2D simulation, when the spoiler is deployed. The velocity contours around the 2D slat (Figure 5.5(a)) show the high velocity at the main-element leading edge compared to flow around the 3D slat (Figure 5.5(b)). The flow acceleration is caused by a strong pressure gradient around the leading edge. Examining Figure 5.4 shows that the $C_p$ distribution plateaus around the main-element leading edge for the 3D simulation, while the pressure distribution around the 2D HLDs shows a strong pressure gradient over the main-element. The strong pressure gradient that is present in the 2D flow field may be responsible for the predicted flow separation.

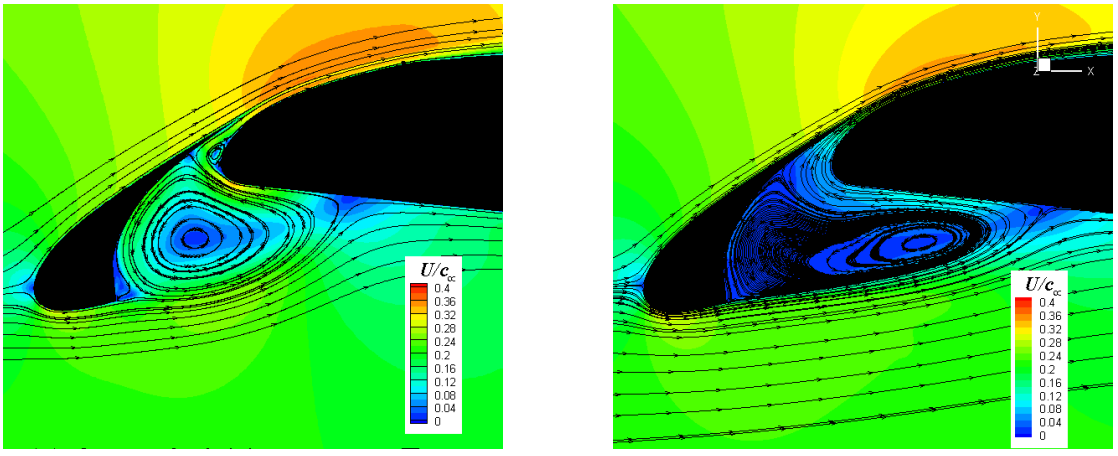


(a) 2D slat steep configuration.

(b) 3D slat steep configuration.

FIGURE 5.6: Mean velocity field and streamlines around the 2D and 3D slat with the spoiler deployed.

Figure 5.7 and Figure 5.8 shows the comparison of the mean streamlines and velocity contours around the 2D and 3D flap for the conventional and steep HLDs

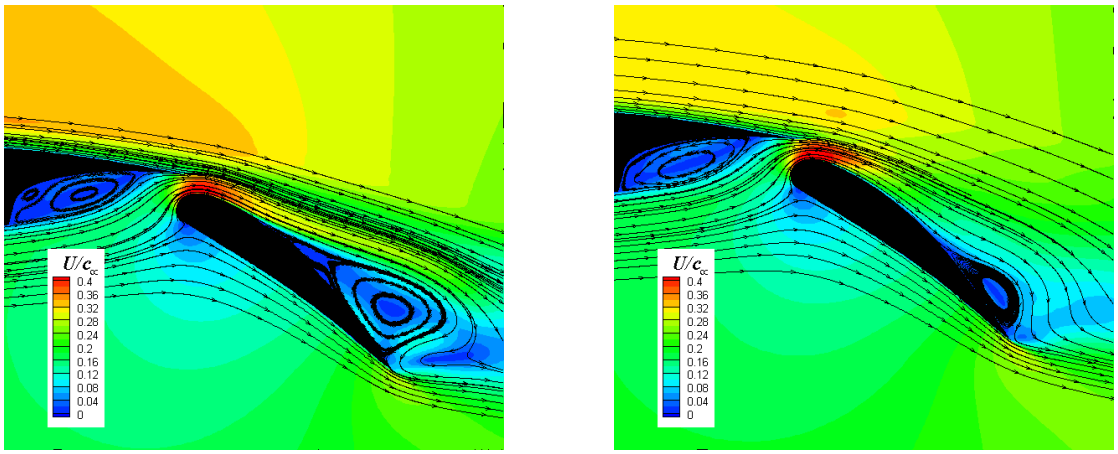


(a) 2D flap conventional configuration.

(b) 3D flap conventional configuration.

FIGURE 5.7: Mean velocity field and streamlines around the 2D and 3D flap for conventional HLD configurations.

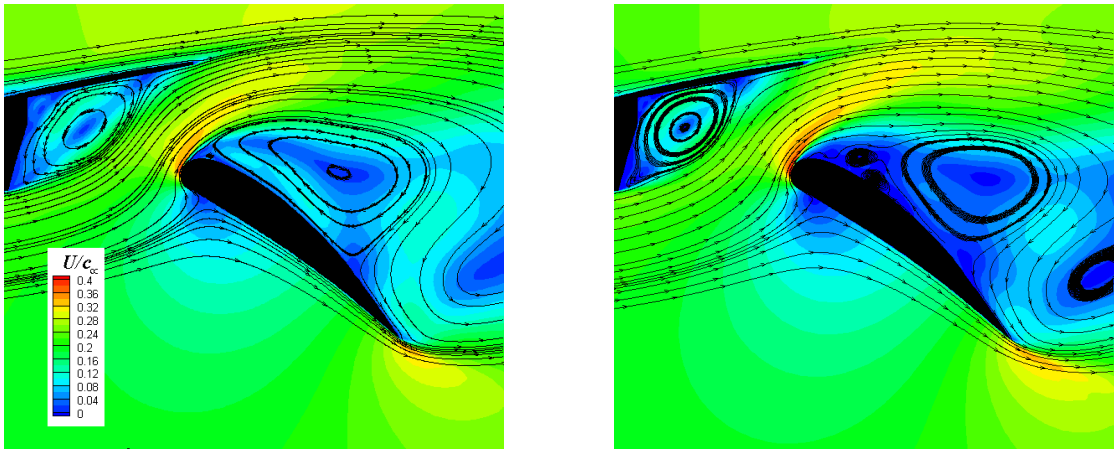


(a) 2D flap steep configuration.

(b) 3D flap steep configuration.

FIGURE 5.8: Mean velocity field and streamlines around the 2D and 3D flap with the spoiler deployed.

respectively. Comparison of Figure 5.7(a) and 5.7(b) shows that the 3D flow separates further downstream on the flap suction surface compared to the 2D flow. The 3D simulation predicts a smaller region of flow separation at the flap trailing edge, whereas the 2D simulations predict a large region of separated flow. Both 2D and 3D flow field around the flap, when the spoiler is deployed ( Figure 5.8(a) and 5.8(b) respectively) show that the flow separates at the flap leading edge to form a large region of slow moving air above the flap suction surface. The predicted extent of the separate region on the flap suction surface from the 2D and 3D simulations are in good agreement.

The difference in the mean flow field around the HLDs can be attributed to two factors. Firstly, the difference in the turbulence modeling - this will affect the

location of flow separation and the level of fluctuations in the separated shear layer. Secondly, the difference in grid resolution between the 2D and 3D grids. Due to constraints of computational resources and computational time, the 2D grid profiles used to generate the 3D grids have approximately 60% fewer grid points.

### 5.3.3 Instantaneous Flow Field

Figure 5.9 shows the instantaneous 3D flow field around the conventional and steep slat. The turbulent structures are shown by positive iso-surfaces of the $Q$-criterion, $Q = -\frac{1}{2}\left(S_{ij}S_{ij} - \Omega_{ij}\Omega_{ij}\right)$, coloured by the vorticity magnitude. The $S_{ij}$ and $\Omega_{ij}$ are the mean strain rate and the mean rate-of-rotation tensors respectively. A positive value of the $Q$-criterion represents regions of the flow where the rate-of-rotation exceeds the rate of strain i.e. inside a vortex. In the absence of the spoiler, the

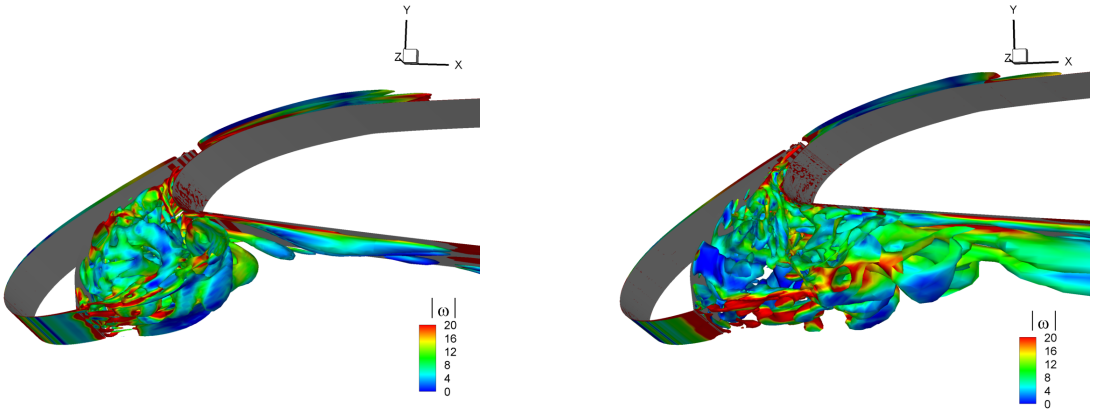


(a) Conventional configuration.

(b) Steep configuration.

FIGURE 5.9: Iso-surface of instantaneous second invariant of velocity gradient tensor coloured by non-dimensional vorticity magnitude around the slat region.

separated shear layer from the slat cusp rolls into spanwise vortices immediately after separating from the slat cusp, see Figure 5.10(a). When the spoiler is deflected, the separated shear layer rolls into spanwise vortices further away from the slat cusp. The spanwise vortices travel further downstream, hitting the main-element leading edge near the stagnation point. The interaction of the spanwise vortices with the main-element surface induces strong pressure fluctuations on the surface which can radiate to the far-field as noise. Comparison of Figures 5.9(a) and 5.9(b) shows that the slat cove vortex increases in size when the spoiler is deployed. The instantaneous 3D flow field around the flap on the conventional and

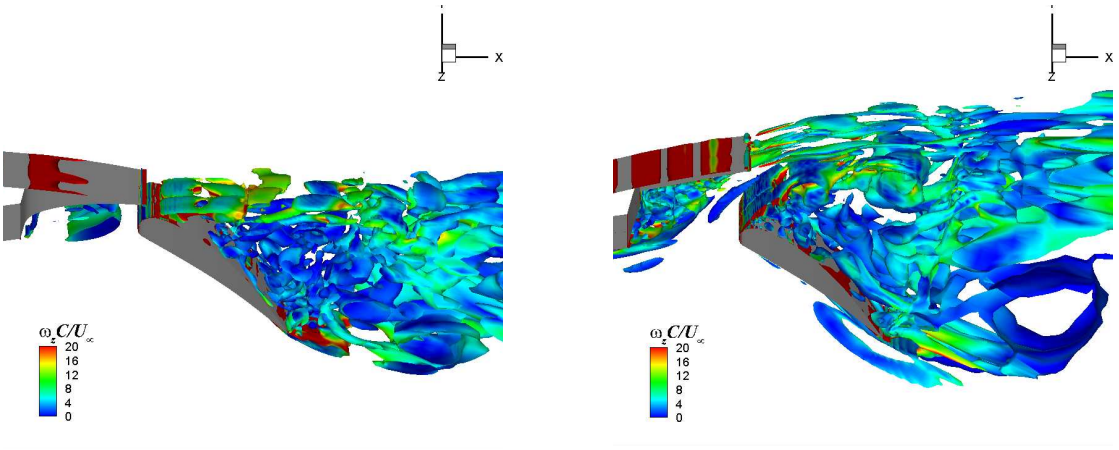


(a) Conventional configuration.

(b) Steep configuration.

FIGURE 5.10: Iso-surface of instantaneous second invariant of velocity gradient tensor coloured by non-dimensional vorticity magnitude around the flap region.

steep HLDs is presented in Figure 5.10. The turbulent structures are shown by the positive iso-surfaces of the $Q$-criterion coloured by the vorticity magnitude. The flow field around the conventional and steep HLDs show that the flow separates on the flap suction surface. When the spoiler is deflected, the separation occurs near the leading edge (Figure 5.10(a)), whereas when the spoiler is retracted, the flow separates around mid-chord (Figure 5.10(b)).

Figure 5.10(b) shows that when the spoiler is deployed, the shear layer that separates from the flap leading edge rolls into spanwise vortices downstream of clockwise rotation. Two such spanwise vortices can be seen above the flap in Figure 5.10(b). The frequency of the vortex shedding behind the flap is $St = 0.18$ ($f = 60$ Hz), where Strouhal number $St$ is based on the flap chord. The vortex shedding frequency is in good agreement with the frequency of vortex shedding predicted from the 2D computations. The fluctuating surface pressure caused by the shedding of vortices contributes to the dipole noise source on the surfaces of all three elements. The 3D flow field around the spoiler trailing edge does not show any evidence of the vortex shedding which is predicted in the 2D simulation. The reason for the absence of vortex shedding at the spoiler trailing edge for the 3D simulation may be linked to the reduction in the grid resolution at the trailing edge.

## 5.4 Acoustic Field

This section presents results of the near-field and far-field acoustics obtained from the 3D simulations. The far-field noise directivity and spectra from the conventional and steep HLDs are compared in order to gain insights into the impact of the spoiler. Trends obtained from the 3D simulations are also compared with the trends from the 2D simulations.

### 5.4.1 Near-field Noise Generation

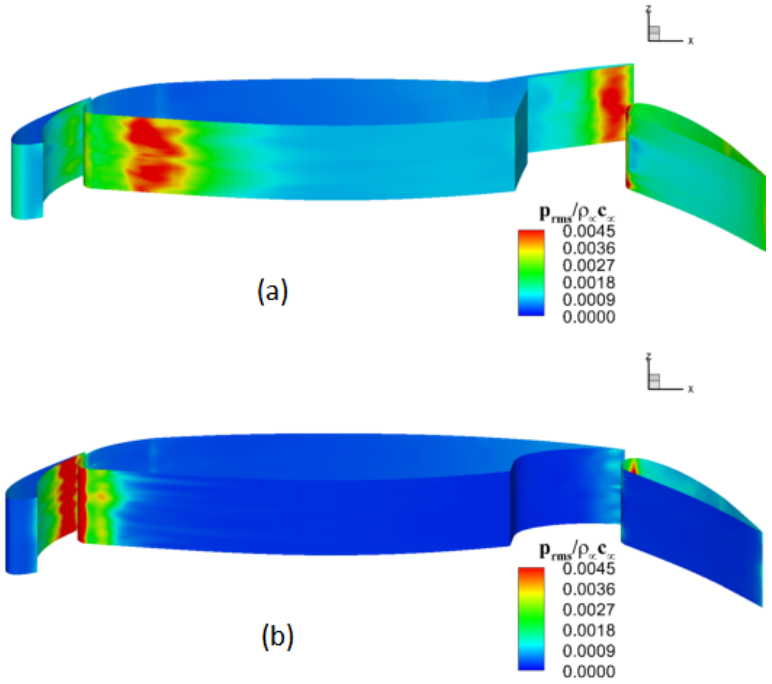


FIGURE 5.11: Comparison of the pressure fluctuations on the surface of the (a): steep HLDs and (b): conventional HLDs.

The surface pressure fluctuations on the conventional and steep HLDs are plotted in Figure 5.11. Since the pressure fluctuations exerted by an unsteady flow over the surface can radiate to the far-field as noise, the distribution and level of pressure fluctuations in Figure 5.11 give an indication of the location and strength of the noise sources. In the absence of the spoiler (Figure 5.11(b)), the highest pressure fluctuations occur on the slat lower surface at the reattachment point and on the main-element leading edge. When the spoiler is deflected, the highest pressure fluctuations occur near the main-element stagnation point and on the lower surface of the deflected spoiler where the flow reattaches. The high pressure fluctuations

on the slat observed in the absence of the spoiler are significantly reduced when the spoiler is deflected.

The non-dimensional turbulent kinetic energy $\mathrm{TKE}_{3D} = 0.5\left(\langle uu\rangle + \langle vv\rangle + \langle ww\rangle\right)/U_\infty^2$, around the slat in conventional and steep configurations is shown in Figure 5.12. Figure 5.12(a) shows a region of high turbulent kinetic energy near the slat reattachment point. This is where the separated shear layer from the slat cusp impinges onto the lower surface of the slat before accelerating towards the slat trailing edge. In Figure 5.12(b), when the spoiler is deployed, the turbulent kinetic energy is significantly reduced near the slat reattachment point. A region of high TKE occurs over the main-element stagnation point, where the separated shear layer from the slat cusp impinges on the main-element pressure surface. The trends observed agree with Figure 5.11, which shows the reduction in pressure fluctuations near the slat reattachment point and the increased level of pressure fluctuations at the main-element stagnation point, when the spoiler is deployed.

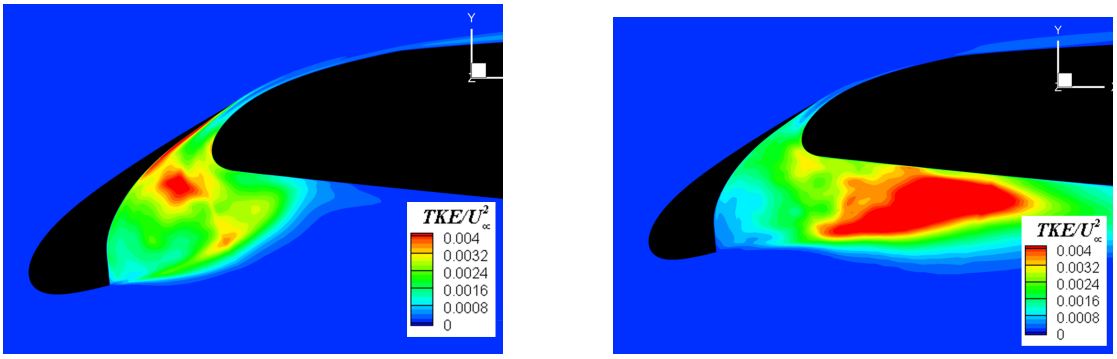


(a) Conventional slat.

(b) Steep slat.

FIGURE 5.12: Non-dimensional turbulent kinetic energy distribution in the slat cove region).

Figure 5.13 shows contours of turbulent kinetic energy around the flap for the conventional and steep HLDs. For both HLD configurations the wake downstream of the flap has the highest level of turbulent kinetic energy. When the spoiler is deflected, high levels of turbulent kinetic energy are observed at the reattachment location on the lower surface of the spoiler. The separated shear layer from the flap cusp impinges on the lower surface of the spoiler which creates high levels of turbulence. Figure 5.11 shows that the impingement of the shear layer causes strong pressure fluctuations at the reattachment point. This is a potential source of noise when the spoiler is deployed.

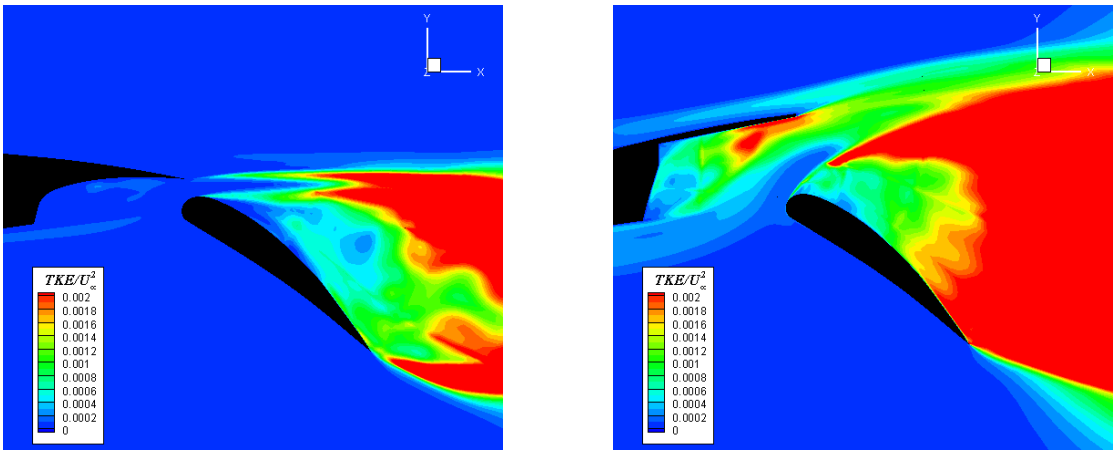


(a) Conventional flap. (b) Steep flap.

FIGURE 5.13: Non-dimensional turbulent kinetic energy distribution around the flap.

### 5.4.2 Far-field Noise Radiation

The 3D simulations are run for over 10 flow-through of the stowed chord before sampling data from the FW-H surface. The simulation are then run for a further 15 flow-through of the stowed chord, where data is sampled every 80 time steps, yielding a sampling rate of 43 kHz. Similar to the 2D computations in the previous chapter, a total of 72 receivers are positioned at 100 m radius from the HLDs at 5 degrees interval. At each receiver station, a total of approximately 10,000 samples are collected which are divided into 3 blocks of 4096 samples each with 50% overlap. A Hanning window function is applied on the pressure signal in each block before computing the FFT to obtain the far field noise spectra.

Only solid-body FW-H surfaces are used for the far-field noise computation. The spanwise length of the FW-H surfaces is set equal to the spanwise length of the CFD model. This is in contrast with the 2D simulations, where the spanwise length was extruded to 1 chord length. The far-field pressure calculated from the 3D simulations is normalised by the spanwise length of the FW-H surface for comparison with the 2D far-field noise levels.

Figure 5.14(a) compares the far-field overall noise directivity from the slat for observers at 100 m radius from the conventional and steep HLDs. Similar to the results from the 2D simulations, the far-field slat noise directivity resembles a dipole source pattern where the dipole axis is perpendicular to the slat chord (see Figure 4.28 for comparison). The overall noise directivity shows that deploying the spoiler results in a small reduction in the overall noise level from the slat. The

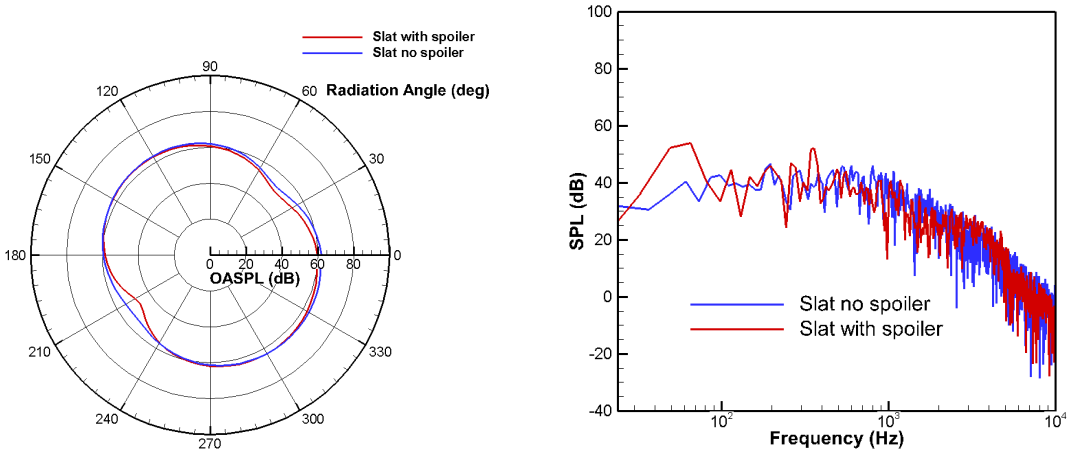


(a) Overall far-field noise directivity.

(b) Far-field noise spectra at $\theta = 270$ degrees.

FIGURE 5.14: Comparison of the far-field overall noise directivity and spectra from the slat.

2D far-field noise directivity shows that deploying the spoiler increases the slat noise level for all observer angles. The reason for the discrepancy becomes clear when the noise spectra at the overhead position are examined.

Figure 5.14(b) presents a comparison of the narrowband noise spectra from the slat at the overhead position for the conventional and steep HLDs. when the spoiler is deployed, the slat noise spectrum features prominent noise peaks at $f = 60$ Hz and at $f = 300$ Hz. For frequencies $f > 500$ Hz, the noise from the slat is slightly reduced when the spoiler is deflected. Both the far-field noise spectra obtained from the 3D simulation and the 2D simulation have a noise peak at $f \approx 60$. However the 2D slat noise spectra has a prominent tonal peak at $f = 2.3$ kHz, which is missing from the 3D noise spectrum. The origin of the noise peak in the 2D simulation is the vortex shedding from the separated shear layer from the main-element leading edge. In the 3D simulation, the flow does not separate at the main-element leading edge. The source of the noise peak at $f = 300$ Hz is not clear.

The reduction in the slat noise level when the spoiler is deployed has been previously observed in tests performed on a scaled aircraft model in a wind tunnel [74]. A microphone array was used to locate and measure the strength of noise sources on a high-lift wing. The microphone array noise map shown in Figure 5.15 shows the local slat noise reduction when spoiler number 6 was deflected by 20 degrees [4].

Figure 5.16 shows the noise directivity and spectra from the flap. Deploying the

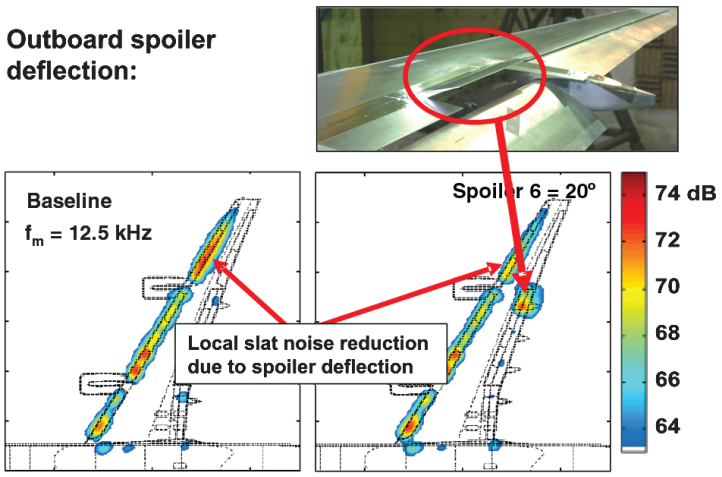


FIGURE 5.15: Noise reduction effect of spoiler deflection on the slat on a scale model high-lift wing.

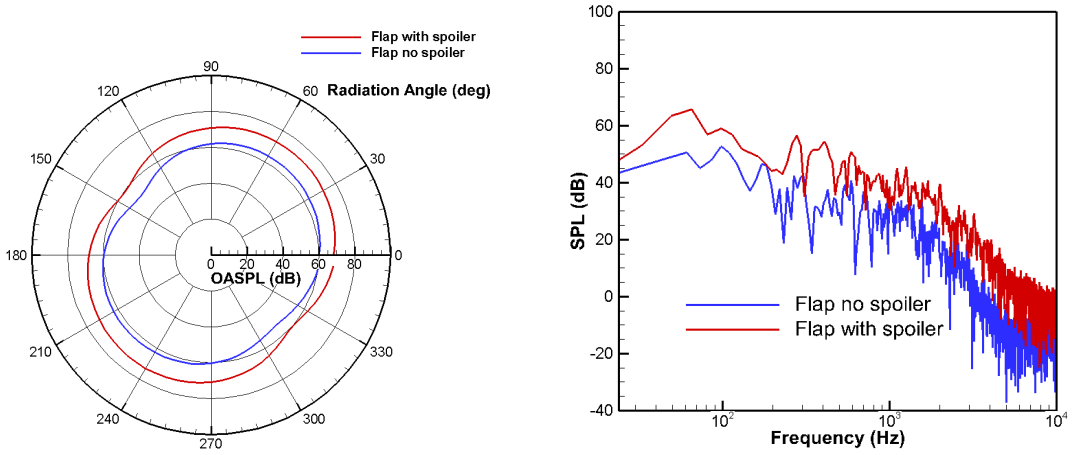


(a) Overall far-field noise directivity.

(b) Far-field noise spectra at $\theta = 270$ degrees.

FIGURE 5.16: Comparison of the far-field overall noise directivity and spectra from the flap.

spoiler increases the noise from the flap for all observer angles (Figure 5.16(a)). Figure 5.16(b) compares the narrowband noise spectra from the flap at the overhead position. The noise spectra show that the maximum noise increase occurs at the same frequency as the vortex shedding downstream of the flap and the spoiler. The absence of the noise peak at $f = 300$ Hz in the flap spectrum with the spoiler deployed suggests that the flap is not the source of the noise at this frequency.

The far-field noise from the main-element in the conventional and steep configurations is presented in Figure 5.17. For the steep configuration, the main-element includes the spoiler. The spoiler increases the overall noise from the main-

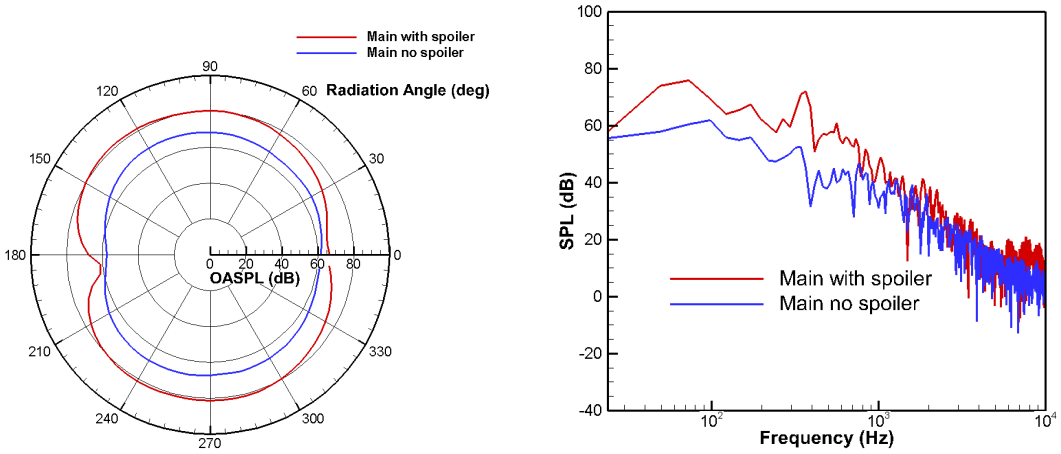


(a) Overall far-field noise directivity.

(b) Far-field noise spectra at $\theta = 270$ degrees.

FIGURE 5.17: Comparison of the far-field overall noise directivity and spectra from the main-element.

element for all observer angles. The narrowband noise spectrum (Figure 5.17(b)) shows two prominent noise peaks at $f = 60$ Hz and $f = 300$ Hz. The level of the noise peaks at $f = 300$ Hz is higher from the main-element compared to that from the slat and the flap in Figures 5.14(b) and 5.16(b) respectively. This suggests that noise at this frequency is generated from the main-element (including the spoiler).

The far-field noise spectra from the main-element(including spoiler) and the spoiler alone are presented in Figure 5.18. The spoiler noise spectrum has a strong peak at $f = 300$ Hz, which has the same level as the peak from the main-element. The evidence suggests that the source of the noise peak at $f = 300$ Hz is on the surface of the spoiler. One possible source of the peak is the impingement of the separated shear layer on the lower surface of the spoiler (see Figure 5.11).

The noise peak at $f = 300$ Hz also occurs in the spectrum from the slat in steep configuration. It is not clear how the contribution from a noise source on the spoiler is also present in the slat far-field noise spectrum.

The overall noise from the conventional and steep HLDs is presented in Figure 5.19(a). Deploying the spoiler increases the overall noise levels from the HLDs for all observers. The noise spectra for the observer at the overhead position are shown in Figure 5.19(b). The spoiler increases the noise from the HLDs for all frequencies. The noise spectrum from the HLDs when the spoiler is deployed has two prominent peaks at $f = 60$ Hz and $f = 300$ Hz. The peak are due to the vortex shedding from the flap and due to a noise source on the spoiler.

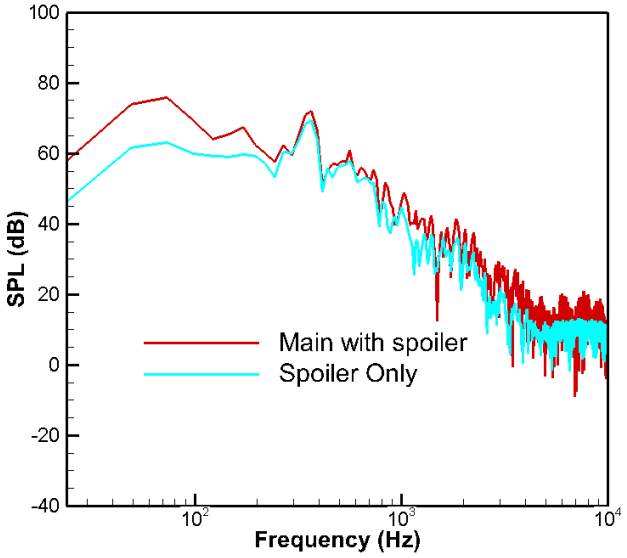


FIGURE 5.18: Comparison of the far-field noise spectra from the main-element and the isolated spoiler for an observer at the overhead position.

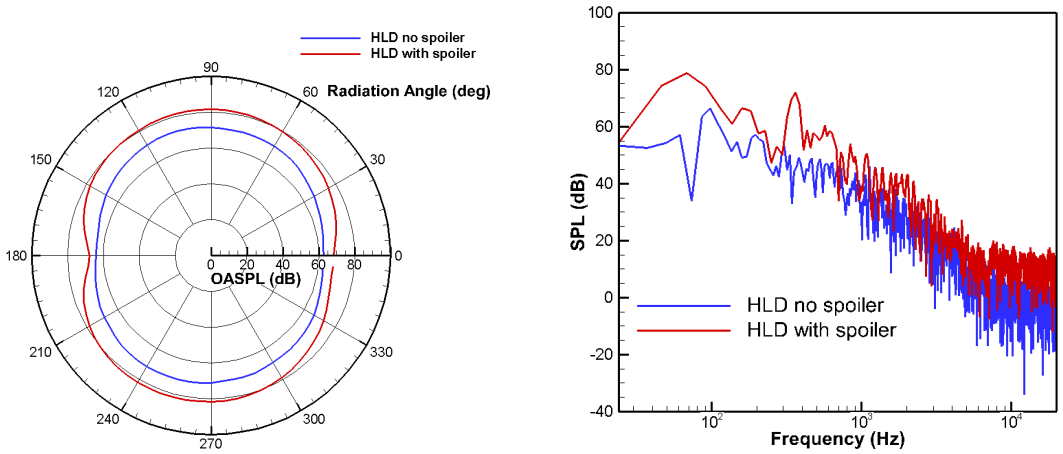


(a) Overall far-field noise directivity.

(b) Far-field noise spectra at $\theta = 270$ degrees.

FIGURE 5.19: Comparison of the far-field overall noise directivity and spectra from the HLDs.

Figure 5.20 presents all of the noise spectra from the individual HLDs in steep configuration. The noise peak at $f = 60$ Hz appears in all the noise spectra. The most significant contribution to the noise at this frequency appears to be from the main-element (including the spoiler). The noise peak at $f = 300$ Hz appears in the noise spectra from the slat, the main-element and the isolated spoiler. The most significant contribution to the noise at $f = 300$ Hz is from the isolated spoiler.

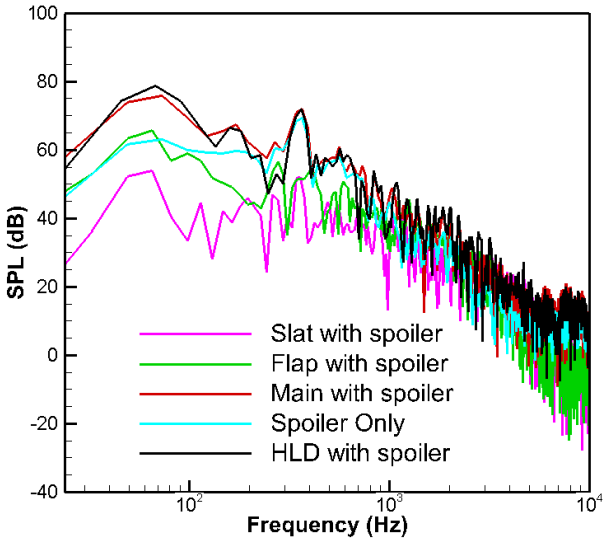


FIGURE 5.20: Narrowband noise spectra from individual HLDs for the observer at $\theta = 270$ degrees.

## 5.5 Summary

Three dimensional DES simulations are performed on the conventional and steep HLD configurations. The general flow physics obtained using the 3D simulations are in agreement with the 2D simulations. The 3D results show that deploying the spoiler results in the expansion of the slat cove vortex. The flow separation from the main-element leading edge is not captured in the 3D simulations. In both the 2D and the 3D simulations, when the spoiler is deployed, the flow separates early at the flap leading edge and forms a large recirculation over a large portion of the flap suction surface. When the spoiler is retracted, the flow separation occurs approximately at half-chord location along the suction surface of the flap. Both 2D and 3D simulations predict the same frequency of vortex shedding behind the flap with and without the spoiler deployed.

Comparison of the far-field noise spectra from the 3D steep HLDs shows a noise peak at $f = 60$ Hz and $f = 300$ Hz. The noise peak at $f = 60$ Hz is caused by the large scale vortex shedding from the flap when the spoiler is deployed. The tonal peak at $f = 300$ Hz is found to originate from the spoiler surface. The precise generation mechanism is not clear as there is not evidence of vortex shedding from the instantaneous flow field. Due to the different flow details obtained from the 2D and 3D simulations, the far-field noise spectra differ somewhat. The 2D noise spectra did not have a peak at $f = 300$ Hz while the 3D noise spectra were missing the tonal peaks at $f = 2.3$ and 4.3 kHz, due to the vortex shedding from

the main-element leading edge and the spoiler trailing edge respectively, which are predicted by the 2D simulations.

The results obtained from the 3D simulation do not completely agree with the 2D results. The cause of the disagreement is the change in the $x$-$y$ profile grid resolution. Due to the constraints of the computational resources, the grid resolution is reduced significantly. The number of grid points in the 2D grid profile is reduced by up to 60%. The current study has highlighted the importance of utilising a sufficient grid resolution in the $x$-$y$ grid profile for 3D simulations.

In the current 3D computations, the spoiler is modeled with the same span as the main wing, thus the effect of the flow field at the spoiler spanwise edge is ignored. The effects of including the spoiler spanwise edge on the near-field and far-field noise of the steep approach high-lift configuration are investigated in the Chapter 6. Aerodynamic and acoustic results from a simulation of the HLDs with a half-span spoiler using the low-order solver are presented.

# Chapter 6

# 3D Simulation of HLD with Half-Span Spoiler

## 6.1 Introduction

In this Chapter the results of the DES of the high-lift system with a half-span spoiler are presented and discussed. The aims of this chapter are to investigate the flow around the side-edge of the spoiler and to investigate the noise contribution from the side-edge to the far-field noise. The discontinuity of the spoiler surface at the side-edge introduces sharp corners to the unsteady flow in this region. Interaction of the unsteady flow with the sharp edges is one of the most efficient noise source mechanisms.

The 3D simulation is performed using a second-order finite volume solver. The low-order solver is also used to perform a simulation of the flow around the high-lift wing with a full-span spoiler, in order to provide a baseline for comparison with the results from the high-order solver from the Chapter 5.

## 6.2 Geometry and Flow Conditions

The high-lift geometry used in the current 3D simulation is the same as the geometry in the previous chapter. The deflection angles for the slat and flap are 30 and 38 degrees respectively. The same freestream conditions are used namely, Mach number is $M_\infty = 0.235$, which corresponds to a Reynolds number $Re = 5.4 \times 10^6$ based on the model stowed chord, and a 5 degrees angle of attack.

### 6.2.1 3D Grid around the HLD with Half-Span Spoiler

Figure 6.1 shows the grid on the surface of the HLD with the half-span spoiler. The total high-lift model span is chosen to be 50% of the stowed chord length of the model. The span is chosen such that the spanwise boundaries would have no effect on the flow at the midspan, while at the same time keeping the number of grid points to a manageable level. The grid is clustered around the spoiler side-

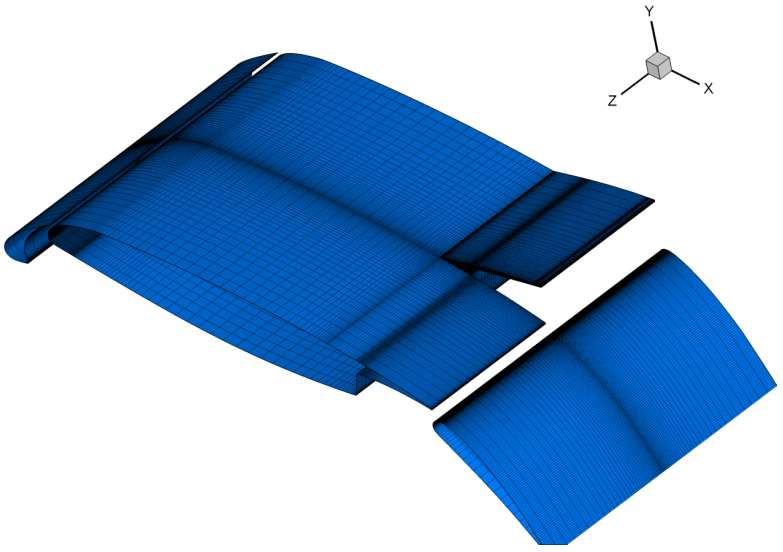


FIGURE 6.1: Overview of the grid on the surface of the steep HLDs configuration with a half-span spoiler.

edge to capture the flow structures in this region. The spanwise spacing at the first point away from the spoiler side-edge is set to $\Delta z/C = 0.001$. The grid spacing increases slowly away from the spoiler side-edge. At the spanwise boundaries, the grid spacing stretches to $\Delta z/C = 0.02$. A total of 100 grid points are used along the span of the model to obtain the required grid resolution. In order to accurately resolve the unsteady flow, a structured grid is employed in the region close to the high-lift model which includes: the side-edge of the spoiler, the slat cove, flap cove and the wake behind the HLDs. Outside the region close to the HLDs, an unstructured grid is employed. A fully structured grid all the way to the computational domain extent would incur very high computational costs. Patching the region further away from the surface of the HLDs with an unstructured grid greatly reduces the total number of grid points needed to simulate the entire flow field. The final grid for the HLDs with half-span spoiler configuration consists of $10.3 \times 10^6$ cells.

TABLE 6.1: Grid details for the low-order and high-order 3D simulations.

| **Grid Parameter** | **Low-Order Grid** | **High-Order Grid** |
|---|---|---|
| Type of cells | Mixed(Tet & Hex) | Hex |
| 2D profile grid size | $1.37 \times 10^5$ | $2.63 \times 10^5$ |
| Spanwise grid points | 62 | 62 |
| Total grid points | $8.5 \times 10^6$ | $16.28 \times 10^6$ |

### 6.2.2 3D Grid around HLD with Full-Span Spoiler

The details of the 3D grid for the HLDs with a full span spoiler are presented. Table 6.1 compares the 3D grid used in the low-order simulation to the grid used in the high-order simulation of the previous chapter. The low-order simulation employs tetrahedral and hexahedral meshes whereas a hexahedral mesh is employed in the high-order simulation. The low-order simulation uses half the number of cells compared to the high-order simulation. The 2D spanwise grid used in the low-order simulation is made up of 92% structured cells. The same number of grid points are used across the span of the HLDs for both the low- and high-order simulation.

A close-up of the low-order grid is shown in Figure 6.2. Structured hexahedral cells are used on the surface of the HLDs and in the near-field, where the flow is expected to be separated from the surface. The wake of the HLDs is meshed using hexahedral cells in order to capture the details of the separated shear layers and the vortex shedding from the flap and the spoiler (Figure 6.2(b)). Unstructured tetrahedral cells are utilised in the regions of the computational domain that are far away from the HLD surfaces and wake.

### 6.2.3 Boundary Conditions

The boundary conditions employed in the two simulations are shown in Figure 6.3. The no-slip boundary condition is imposed on the solid surface of the high-lift devices. The non-reflecting pressure far-field boundary condition is used at the streamwise computational domain boundaries. The boundary conditions prevent the reflection of outgoing waves from the computational boundary. Details of the non-reflecting pressure far-field boundary conditions are presented in Chapter 3.

A symmetry boundary condition is applied to the spanwise extents of the

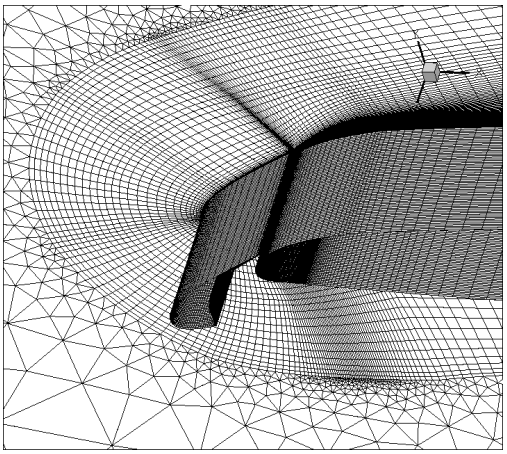

(a) Grid around slat used in low-order simulation

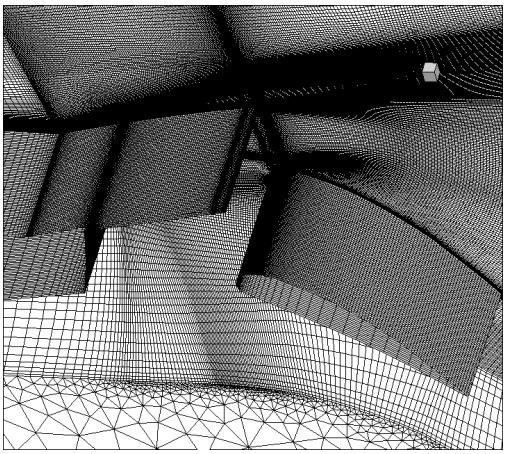

(b) Grid around flap and spoiler used in low-order simulation

FIGURE 6.2: Details of the 3D grid around the HLD with full-span spoiler for the low-order simulation.

computational domain for the HLD with the half-span spoiler. The physical flow conditions set at these boundaries are no convective flux and no diffusive flux across the symmetry boundary. Thus the normal velocity at the symmetry plane is set to zero and the normal gradients of all variables are also set to zero. In the case of the simulation of the HLD with a full-span spoiler, a periodic boundary condition is applied on the spanwise boundaries.

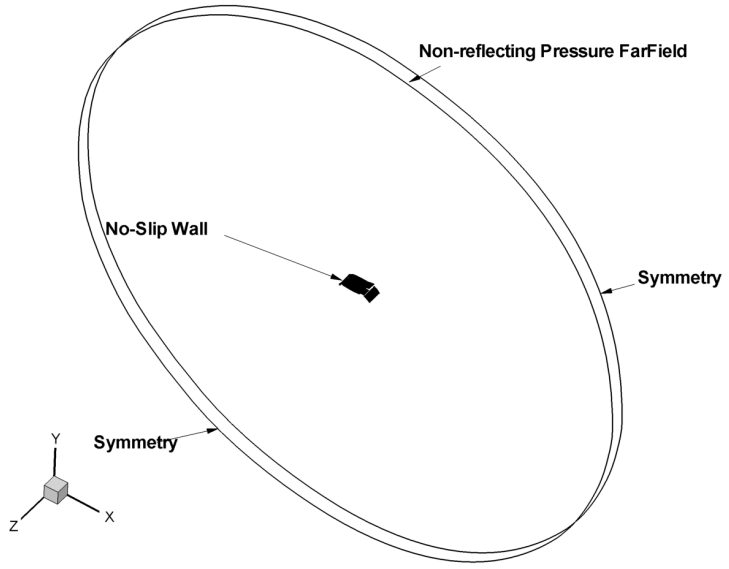


FIGURE 6.3: Sketch of the boundary conditions imposed on the computational domain.

### 6.2.4 Solution Methodology

The low-order commercial solver used is a cell-centred finite volume CFD code. The code solves a pressure-velocity correction equation to achieve mass conservation of the velocity field. The pressure equation is derived from the continuity and the momentum equations in such a way that the velocity field, corrected by the pressure, satisfies the continuity equation. The SIMPLE (Semi-Implicit Method of Pressure Linked Equation) pressure-velocity correction algorithm is used. The discretisation scheme for the pressure is second-order. A second-order upwind discretisation is employed for solving the continuity and energy equations. The momentum equation and the transport equation for the turbulent viscosity in the S-A model are solved using a second-order central differencing scheme. For time advancement, an implicit second-order time integration scheme with dual time stepping is used. The simulations are performed using a non-dimensional time step of $\Delta tC/U_\infty = 6.25 \times 10^{-7}$ and 20 sub-iterations are required to reduce the residuals by $10^{-3}$ at every time step.

The computations are performed in parallel on the University of Southampton Iridis 3 high performance computing cluster using 32 CPUs. The computational cost per time step is approximately 170 seconds, equivalent to 8.5 seconds per iteration. The simulation of 1 flow-through of the stowed chord required 250 time steps. This corresponds to 378 CPU-hrs per flow-through.

The rest of this chapter is divided into two main sections. The results from the simulation of the flow around the HLD with full-span spoiler are discussed in Section 6.3. Section 6.4 presents the results from the simulation of the flow around the HLD with half-span spoiler.

## 6.3 Simulation of HLD with Full-Span Spoiler

The low-order solver is used to perform a simulation of the flow around the 3D steep HLDs with a full-span spoiler. The near-field flow and far-field acoustic results are compared with the results from the high-order simulation of the previous chapter. The purpose of this section is to provide a baseline for comparison with the results from the simulation of the HLD with the half-span spoiler and to provide a consistency check of the low-order to high-order simulation strategy.

### 6.3.1 Time Averaged Flow Field

Figure 6.4 compares the mean pressure distribution over the HLD with a full-span spoiler obtained from the low- and high-order simulations. The surface pressure is averaged in time and in space over the spanwise length of the model. The two pressure distributions compare reasonably well over the surface of the HLDs. Both the low-order and high-order simulations predict the flow stagnation at the same position on all three elements. However, the low-order simulation predict a higher positive pressure at the main-element stagnation point compared to the high-order simulation. The low-order simulation also predicts a significantly higher suction pressure over the flap leading edge compared to the high-order simulation. The difference between the predicted pressure using the low-order and high-order simulation can be attributed to the different meshes resolution around the HLDs.

The mean flow field around the HLDs obtained using the low-order and the high-order simulations are compared in Figures 6.5 and 6.6. The flow field around the slat obtained low-order and high-order 3D simulations agree reasonably well, considering the different mesh resolution and the different spatial order of accuracy of the two solvers. The mean flow field obtained from the low-order and high-order simulations show that there is no flow separation at the main-element leading edge.

Figure 6.6 compares the mean flow field around the flap obtained from the low- and high-order simulations. Both simulations predict the flow separation at the flap leading edge and the formation of the large recirculation region over the suction surface of the flap. The size of the separated flow region of the the flap is the same for the two simulations. On the spoiler, the reattachment point obtained from the low-order simulation is closer to the spoiler trailing edge compared to the high-order simulation.

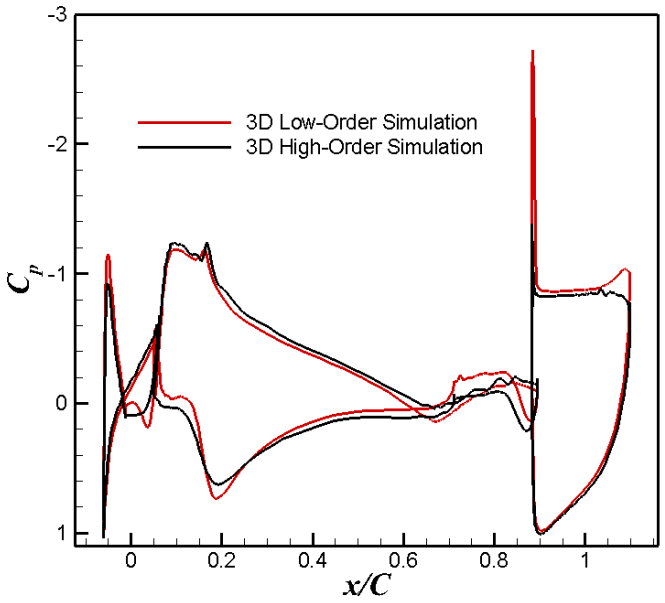


FIGURE 6.4: Comparison of the surface pressure distribution on the HLD with full-span spoiler obtained from the low- and high-order simulations.

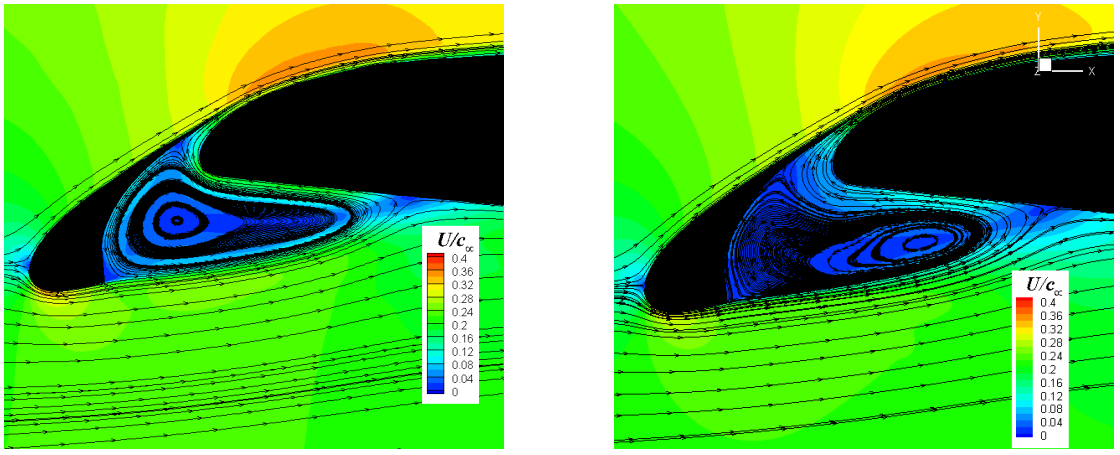


(a) Low-order simulation

(b) High-order simulation

FIGURE 6.5: Comparison of the mean flow around the slat in the low- and high-order simulations.

### 6.3.2 Instantaneous Flow Field

In this section, a comparison of the instantaneous flow field around the HLD obtained using the low-order and high-order solvers is presented. The aim is to give a qualitative comparison of the unsteady flow field obtained from the two simulations. In order to capture the three-dimensional structures in the flow, iso-surfaces of the Q-criterion (coloured by vorticity magnitude contours) are shown.

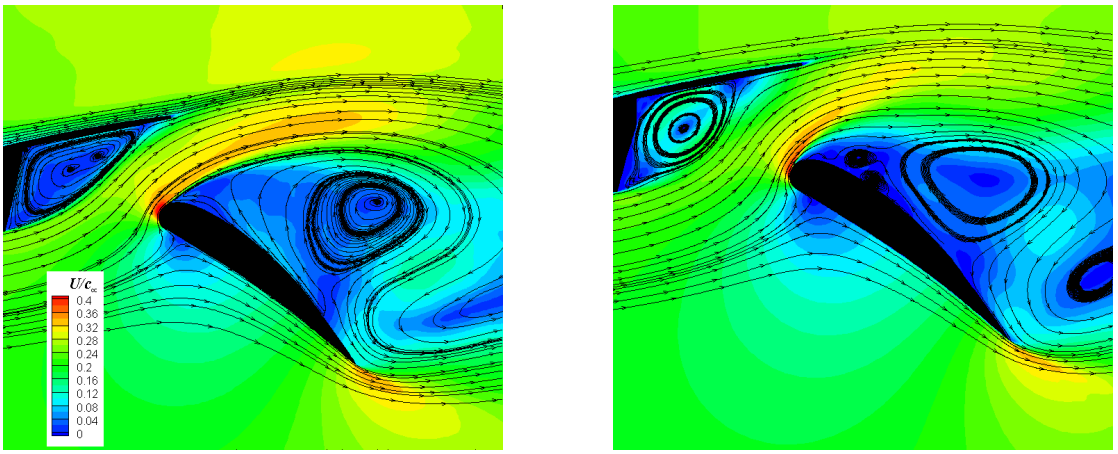


(a) Low-order simulation (b) High-order simulation

FIGURE 6.6: Comparison of the mean flow around the flap in the low- and high-order simulations.

Figure 6.7 shows the instantaneous flow around the slat region obtained using the low-order and high-order solvers. Both simulations captured the roll-up of the shear layer from the slat cusp into large spanwise vortices. The spanwise vortices convect towards the stagnation point on the main-element where they undergo distortions to become predominantly streamwise vortices.

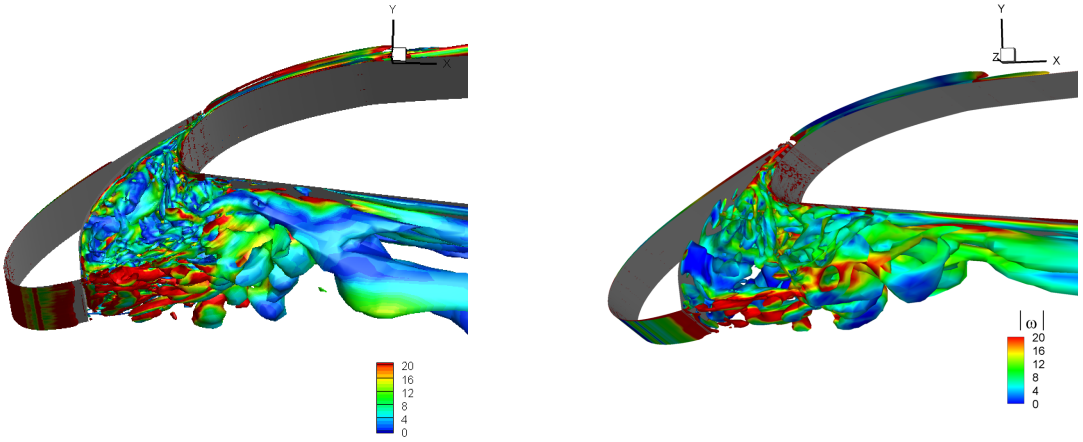


(a) Low-order simulation (b) High-order simulation

FIGURE 6.7: Comparison of the instantaneous flow field around the slat in the low- and high-order simulations.

Figure 6.8 presents the instantaneous flow around the flap from the low- and high-order simulation respectively. Both simulations capture the formation of clockwise spanwise vortices from the free shear layer from the flap leading edge and the large counter-clockwise spanwise vortex at the flap trailing edge. The low-order simulation captures the roll-up of spanwise vortices from the flap cusp and the

vortex shedding at the spoiler trailing edge. The high-order simulation does not clear capture the flow in the flap cove and there is no clear evidence of spanwise vortices emanating from the spoiler trailing edge.

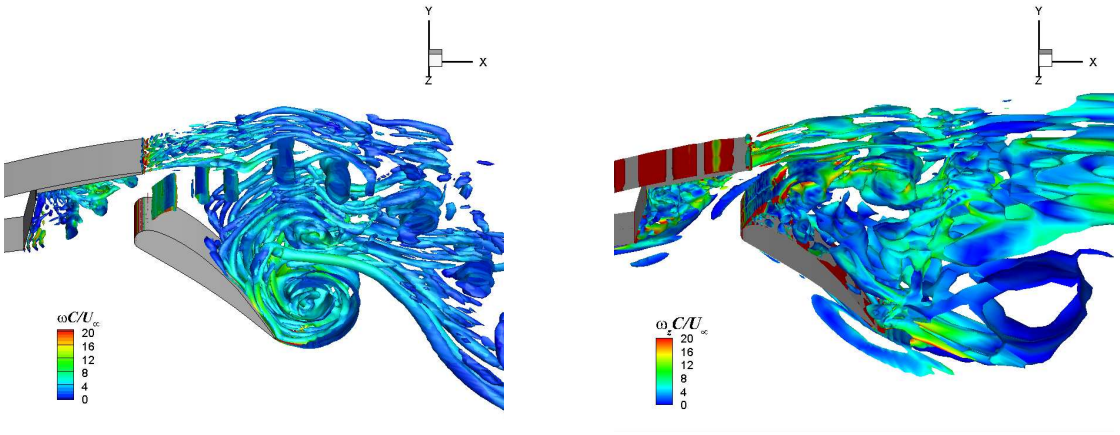


(a) Low-order simulation

(b) High-order simulation

FIGURE 6.8: Comparison of the instantaneous flow field around the flap in the low- and high-order simulations.

The flow structures obtained from the low-order simulation are further analysed in Figure 6.9 and Figure 6.10. The iso-surfaces of $Q$-criterion are coloured by contours of the streamwise and spanwise vorticity. The shear layer that separates from the flap leading edge forms spanwise vortices of clockwise rotation while the shear layer that separates from the flap trailing edge forms spanwise vortices of counter-clockwise rotation.

Figure 6.10(a) shows that the low-order simulation captures the shedding of spanwise vortices from the spoiler trailing edge. The turbulent flow inside the flap cove is presented in Figure 6.10(b). The shear layer that separates from the flap cusp rolls into coherent spanwise vortices. The vortices convect with the flap cove recirculation flow and impinges on the spoiler lower surface at the reattachment point. The vortices then undergo distortion at the reattachment point and emerge with a strong streamwise vorticity component.

### 6.3.3 Acoustic Field

In this section, the results of the comparison of the near-field and far-field noise predicted by the low- and high-order simulations are presented. In Section 6.3.3.1, a comparison is made of the surface pressure fluctuations and the distribution of

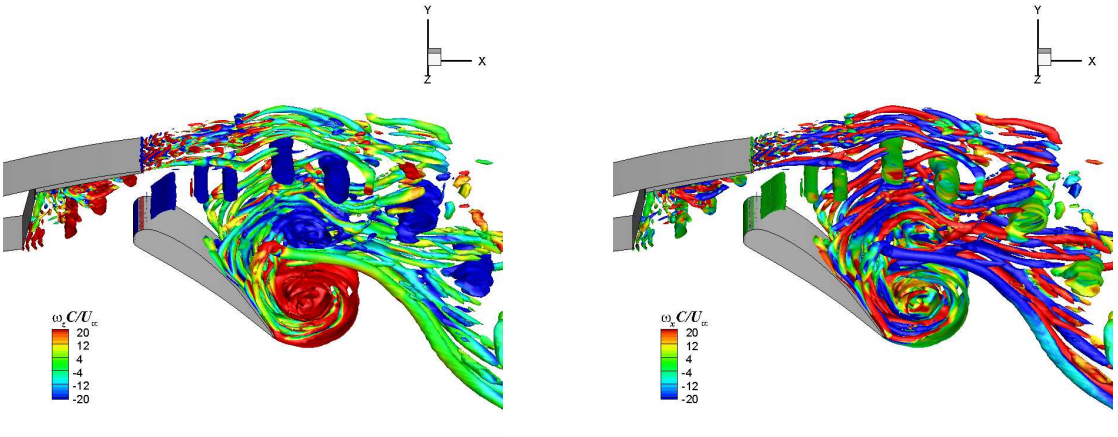


(a) Contours of spanwise vorticity.

(b) Contours of streamwise vorticity.

FIGURE 6.9: Instantaneous vorticity field around the flap obtained from the low-order simulations.

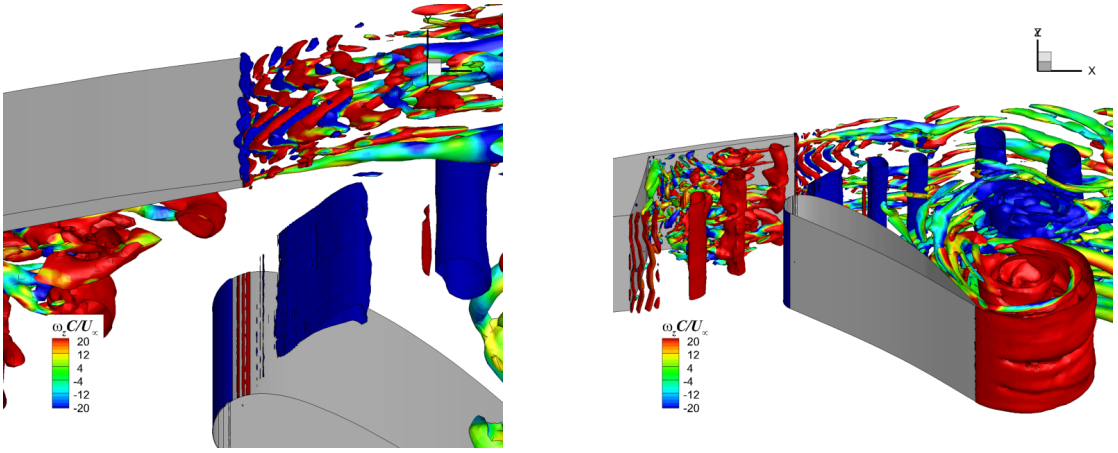


(a) Flow structures at the spoiler trailing edge.

(b) Flow structures inside the flap cove.

FIGURE 6.10: Turbulent flow structures around the spoiler and flap from the low-order simulation.

the turbulent kinetic energy around the HLDs to gain insight into the noise source mechanisms. Finally, in Section 6.3.3.2, a comparison of the calculated far-field noise is presented.

#### 6.3.3.1 Near-Field Noise Generation

Figure 6.11 presents a comparison of the contours of RMS of surface pressure on the lower surface of the HLDs obtained from the low-order and high-order simulations. The magnitude and location of the high pressure fluctuations are in good agreement between the two results. The high pressure fluctuations at the main-element stagnation point are due to the impingement of vortices formed as

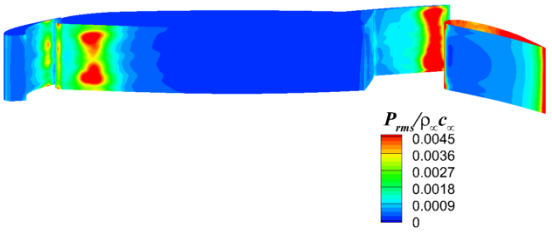


(a) Low-order simulation

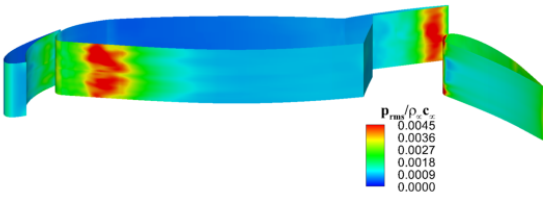


(b) High-order simulation

FIGURE 6.11: Comparison of the surface pressure fluctuations on the HLDs obtained from the low- and high-order simulations.

a result of the roll up of the shear layer from the slat cusp. Similar mechanism produce the high pressure fluctuations at the lower surface of the spoiler where the shear layer from the flap cove attaches to the spoiler surface. The reduction in the pressure fluctuations on the surface of the slat cove is captured in both the low-order simulation and the high-order simulation.

The contours of TKE distribution around the slat is presented in Figure 6.12. In both simulation, the highest TKE levels occur near the main-element leading edge.

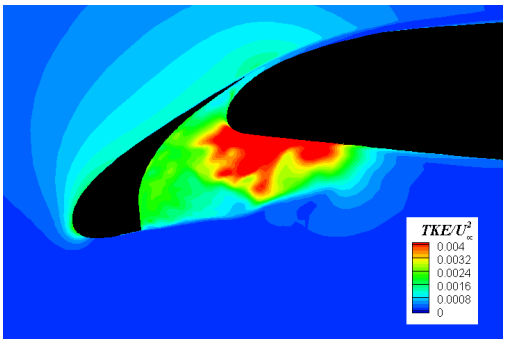


(a) Low-order simulation

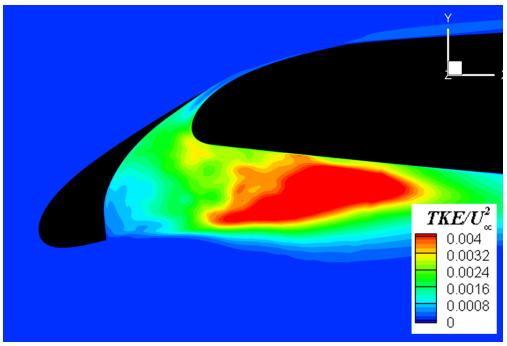


(b) High-order simulation

FIGURE 6.12: Comparison of the time-averaged turbulent kinetic energy distribution around the slat obtained from the low- and high-order simulations.

The contours of TKE distribution around the flap predicted by the low-order and

high-order simulations is shown in Figure 6.13. The highest TKE levels occur in the wake of the HLDs in both simulations. The high-order simulation predicts low TKE levels compared with the low-order simulation, particularly in the flap cove. Figure 6.13(a) shows that the separated shear layer from the flap cusp, impinging on the lower surface of the spoiler, generates high TKE levels. The high TKE levels also occur at the spoiler trailing edge. Figure 6.11 shows corresponding high level of pressure fluctuations at the location where the shear layer from the flap cusp attaches to the spoiler lower surface.

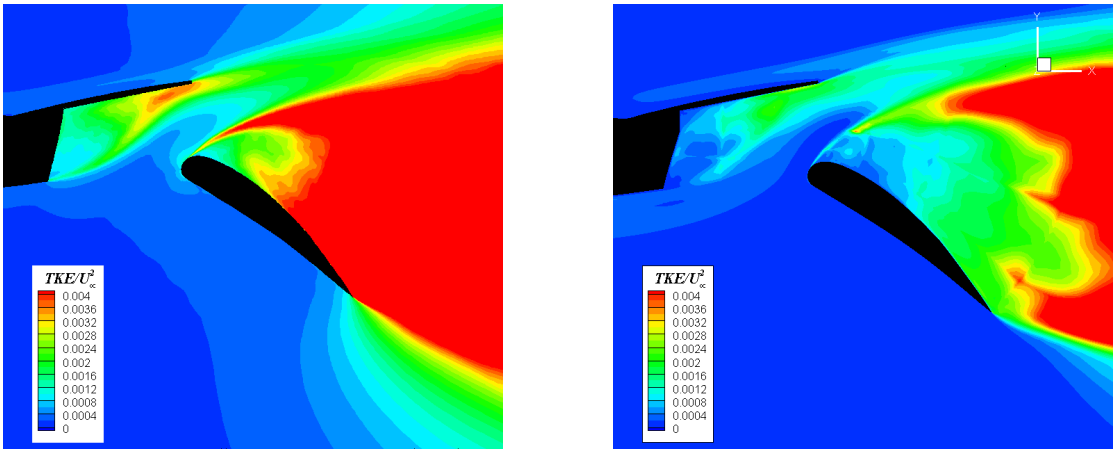


(a) Low-order simulation

(b) High-order simulation

FIGURE 6.13: Comparison of the time-averaged turbulent kinetic energy distribution around the flap from the low- and high-order simulations.

#### 6.3.3.2 Far-field Noise Radiation

For the far-field noise computation, the unsteady data is collected from the solid-body FW-H integration surfaces that include all three high-lift elements. The data is sampled every time step, yielding a sampling rate of 50 kHz (Nyquist frequency $f = 25$ kHz). Similar to the high-order simulations of Chapter 5, a total of 72 observers are located on a circle of radius 100 m away from the HLDs at a 5 degree interval apart. At each receiver location, a total of 8000 samples are collected, which are divided into 2 blocks of 4096 samples each with an overlap of 50%. A Hanning window function is applied on the pressure signal in each block before computing the FFT to obtain the far-field noise spectra.

Figure 6.14 shows the overall noise directivity and the noise spectra from the slat for an observer at the overhead location predicted by the low-order and the high-order simulations. The overall noise level and directivity pattern predicted in the

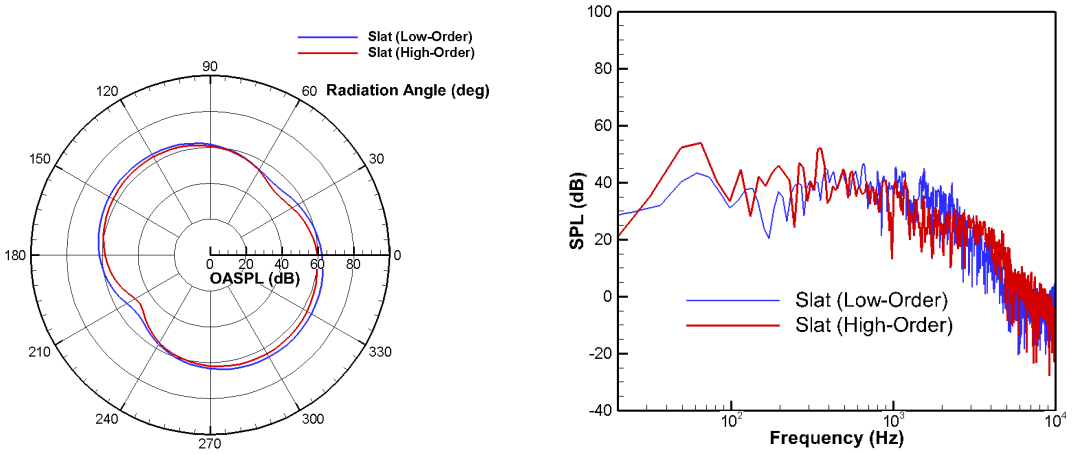


(a) Overall far-field noise directivity.

(b) Far-field noise spectra at $\theta = 270$ degrees.

FIGURE 6.14: Comparison of the far-field overall noise directivity and spectra from the slat.

low-order simulation agree well with the high-order prediction. The predicted noise levels from the low-order simulation are less than 1 dB louder than the predicted noise levels from the high-order simulation.

The noise spectra, Figure 6.14(b), show that the high-order simulation predicts higher noise level at low frequencies ($f < 400$ Hz) while the low-order simulation predicts higher noise levels in the frequency range $1.0 < f < 3$ kHz. Overall the spectra look very similar and the difference may be down to the difference in the size of the data sample collected from the low-order and high-order simulations.

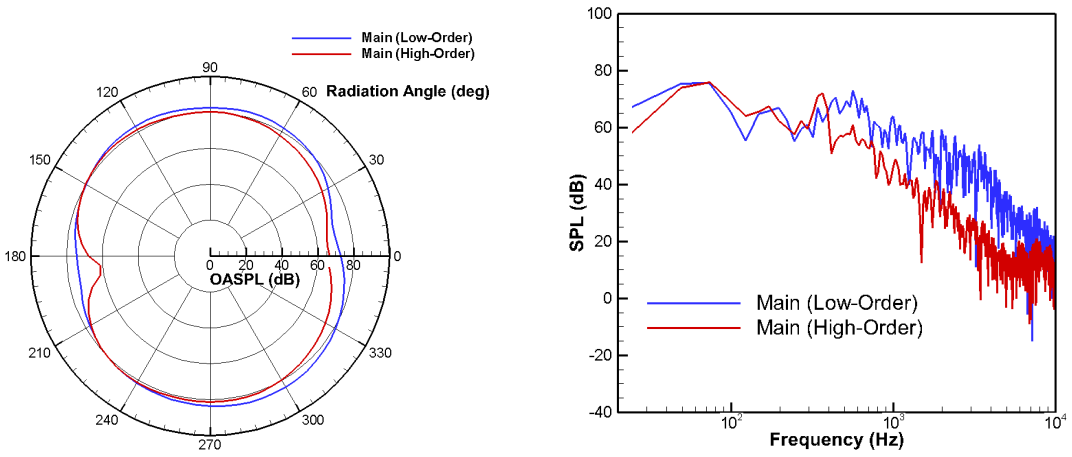


(a) Overall far-field noise directivity.

(b) Far-field noise spectra at $\theta = 270$ degrees.

FIGURE 6.15: Comparison of the far-field overall noise directivity and spectra from the main-element.

Figure 6.15 compares the overall noise directivity and the noise spectra from the main-element predicted by the low-order and high-order simulations. Similar to the slat, the overall noise directivity from the main-element predicted using the low-order solver agrees closely with the predicted noise level from the high-order solver. The noise spectrum from the low-order simulation shows higher noise level for frequencies above approximately 400 Hz compared to the noise spectrum from the high-order simulation.

The overall noise directivity and noise spectra from the flap are compared in Figure 6.16. The low-order simulation predicts higher overall noise level at each observer location compared to the high-order simulation. The noise spectra from the flap, Figure 6.16(b), show that the low-order simulation predicts higher noise levels at all frequencies.

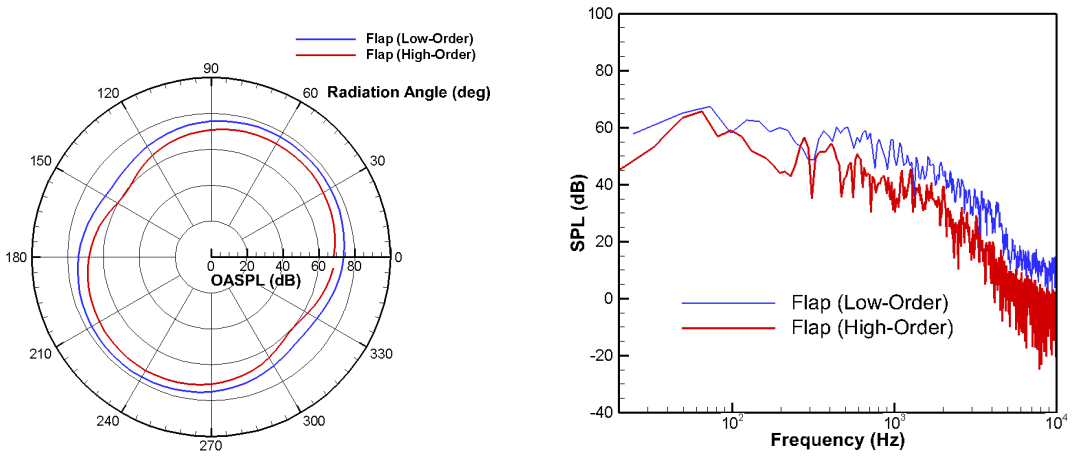


(a) Overall far-field noise directivity.

(b) Far-field noise spectra at $\theta = 270$ degrees.

FIGURE 6.16: Comparison of the far-field overall noise directivity and spectra from the flap.

Figure 6.17 compares the overall noise directivity and spectra from the HLDs predicted by the low-order and high-order simulations. As expected the low-order simulation predicts higher overall noise levels compared with the high-order simulation. The shape of the noise directivity patterns from the two simulations agree very well. Similar to the individual high-lift elements, the low-order simulation predicts higher noise levels at frequencies above 400 Hz.

For the low-order mesh, by using an unstructured mesh away from the HLDs, the number of grids used in the region away from the HLDs is significantly reduced. This allows a finer structured grid to be used in the region of interest close to

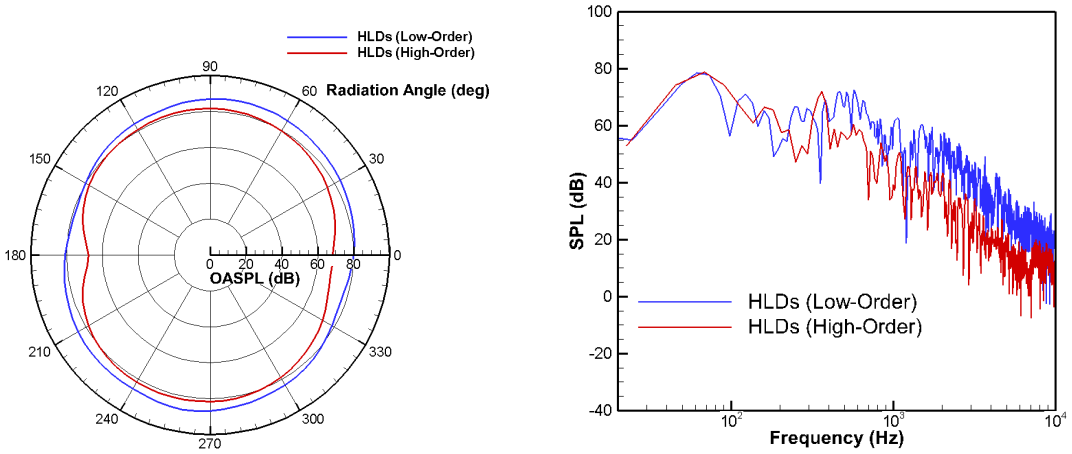


(a) Overall far-field noise directivity.

(b) Far-field noise spectra at $\theta = 270$ degrees.

FIGURE 6.17: Comparison of the far-field overall noise directivity and spectra from the HLDs.

the HLDs, for example around the slat, flap and spoiler. With increased grid resolution, the low-order simulation is able to resolve smaller scale turbulent structures. This explains why the low-order simulation predicts higher noise levels particularly at high frequencies compared with the high-order simulation.

### 6.3.4 Summary

The simulation of the flow around the steep HLD with a full-span spoiler is performed using the low-order CFD solver. The flow field results show that the low-order simulation is able to capture more small scale turbulent structures compared to the high-order simulation of the previous chapter. The improved flow resolution is down to the use of unstructured cells in regions of the computation domain further away from the HLDs. This allows finer structured grids to be applied to the region of interest close to the HLDs to capture the small scale details of the unsteady flow.

The instantaneous flow field predicted using the low-order simulation captures: the three-dimensional shear layer roll-up in the slat and flap cove; the spanwise vortices in the slat and flap cove; the vortex shedding at the spoiler trailing edge; the vortex shedding from the flap leading and trailing edges and the small scale structures in the wake of the HLDs. Compared to the high-order simulation of the previous chapter, the above flow features are not well captured. The low-order and high-order simulations do not capture the flow separation at the main-element

leading edge that is predicted by the 2D simulations.

Comparison of the instantaneous and time-averaged flow field shows good agreement with the results from the high-order simulation. The acoustic results show that the low-order simulation predicts higher overall noise levels compared to the high-order simulation. The far-field noise spectra from the low-order simulations are shown to contain more high frequency content compared to the corresponding spectra from the high-order simulation. This is a result of the improved flow resolution from the low-order simulation due to the fine grids used in regions of the computation domain close to the HLDs. This highlights the importance of using adequate resolution in the 2D spanwise grid profile in order to capture the details of the unsteady flow.

In the next section, the results of the 3D simulation of the steep HLDs with half-span spoiler using the low- and high-order solvers are presented. The purpose of this section is to asses the impact of a finite span spoiler on the near flow field and far-field acoustics of the steep HLDs.

## 6.4 Simulation of HLDs with Half-Span Spoiler

In this section, the results from the low-order simulation of the flow around the steep HLD with a half-span spoiler are presented. The results from the low-order simulation of the HLD with a half-span spoiler are compared with the results from the 3D low-order and high-order simulations of the HLD with a full-span spoiler. The aim of the analysis is to identify the effects on the near-field flow and far-field acoustics from the finite span spoiler.

### 6.4.1 Time Averaged Flow Field

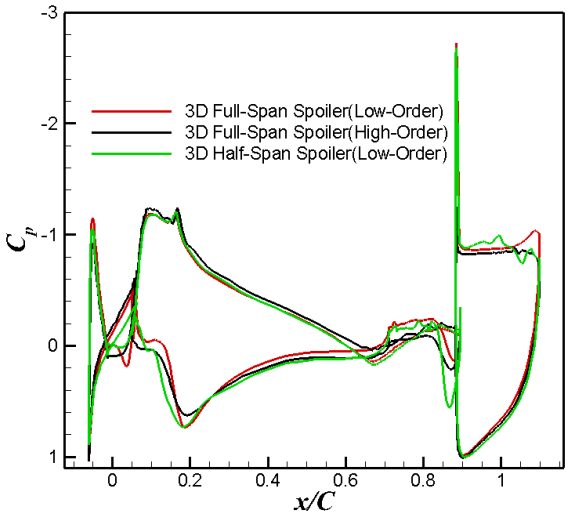


FIGURE 6.18: Comparison of the surface pressure distribution on the HLD configuration with the half-span spoiler and the full-span spoiler.

Figure 6.18 shows a comparison of the surface pressure distribution on the HLDs with the half-span spoiler and the full-span spoiler. The surface pressure on the HLD with the half-span spoiler is averaged in the spanwise direction over the spanwise length of the spoiler. The pressure distribution for the three configurations are in good agreement over all three elements. The magnitude and location of the stagnation point on the main-element predicted by the low-order simulation around the HLD with the half- and full-span spoilers are in very good agreement. The high-order simulation predicts a lower pressure at the stagnation point on the main-element compared to the low-order simulation. The pressure distribution, obtained using the low-order solver, on the flap with the half-span spoiler is the same as that of the flap with the full-span spoiler. However, the

high-order simulation predicts a lower suction peak pressure on the flap leading edge compared with the low-order simulations.

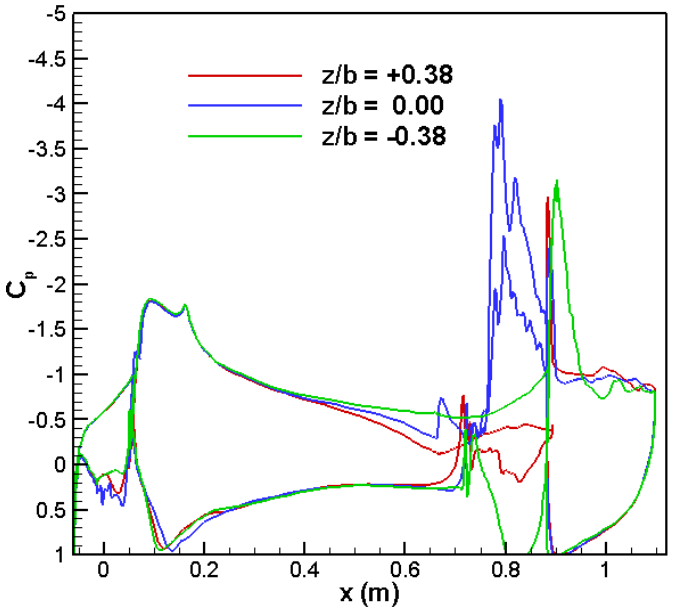


FIGURE 6.19: Distribution of the pressure coefficient around the high-lift configuration with a half-span spoiler.

Figure 6.19 shows the streamwise pressure distribution at three spanwise stations on the high-lift configuration with the half-span spoiler. The position of stations is defined such that: $z/C = 0$ corresponds to the mid-span of the HLD ,at the spoiler side-edge; $z/C > 0$ corresponds to locations inboard of the deflected spoiler and $z/C < 0$ corresponds to locations outboard of the spoiler side-edge.

The peak suction pressure observed on the main-element at the trailing edge location $x/C \approx 0.8$ for the station $z/C = 0$ is caused by the side-edge vortex that sits on the suction surface of the main-element. The vortex forms as the flow from the suction surface of the main-element trailing edge moves onto the pressure surface.

The pressure distribution on the flap shows the different flow regimes along the span of the flap. For the flap spanwise section downstream of the deflected spoiler, at station $z/C = +0.38$, the flow separates at the flap leading edge, indicated by the flat section of the pressure coefficient curve in Figure 6.19. For the the flap spanwise section that is not behind the spoiler, at station $z/C = -0.38$, the flow separates further downstream of the flap leading edge.

The mean pressure distribution on the surface of the high-lift model around the side-edge of the main-element is shown in Figure 6.20. When a vortex is within

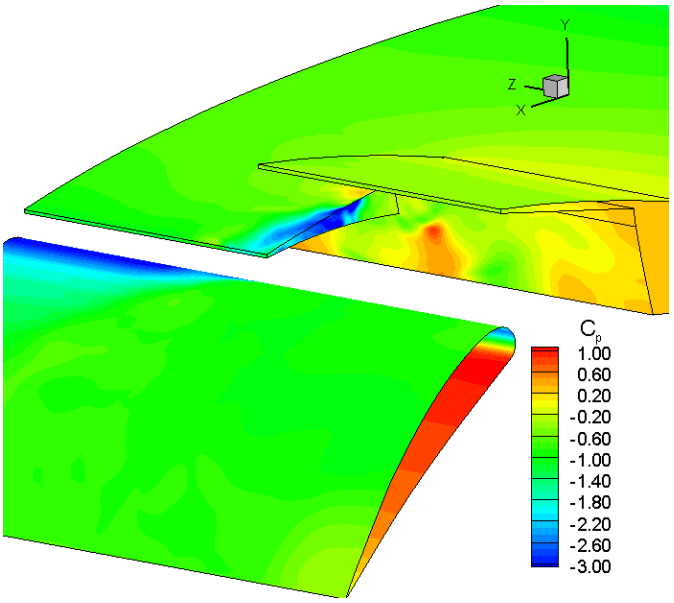


FIGURE 6.20: Surface mean pressure distribution around high-lift configuration.

close proximity of a solid wall, it induces a low pressure footprint on the solid surface. Figure 6.20 clearly shows the trajectory of the vortex that forms around the side-edge of the main-element.

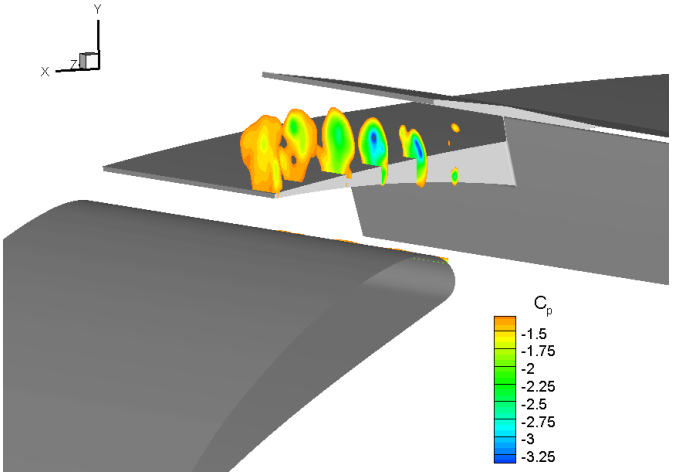


FIGURE 6.21: Pressure contours showing the formation and development of the side-edge vortex.

Figure 6.21 shows contours of pressure on spanwise slices through the vortex. The vortex forms at the bottom corner of the main-element side-edge as the flow from the lower surface of the wing moves to the upper surface. The vortex grows in size downstream until it moves on to the upper surface of the main-element. Further downstream, the vortex separates from the main-element near the trailing edge.

### 6.4.2 Instantaneous Flow Field

The instantaneous 3D flow field over the half-span spoiler configuration is shown in Figure 6.22. Positive iso-surface of $Q$-criterion coloured by the velocity magnitude reveals the turbulent structures in the flow. A vortex occupies the gap between the side-edge of the deflected spoiler and the main-element trailing edge. Due to the pressure difference between the suction-side and pressure-side surface of the main-element, the flow is driven from the pressure-side surface to the suction-side surface. The flow separates at the side-edge bottom corner forming a small vortex which grows downstream. Figure 6.22 shows that the separated vortex interacts with the deflected spoiler above and the flap suction surface downstream.

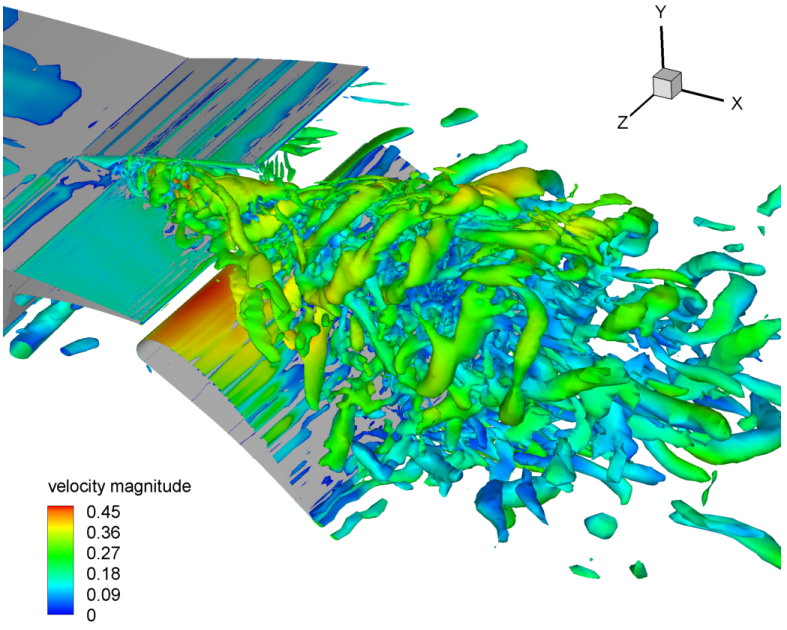


FIGURE 6.22: Positive iso-contours of the $Q$-criterion showing the vortex that occupies the gap between the deployed spoiler and main-element.

Figure 6.23 shows $y-z$ planes through the vortex at different streamwise locations. The vortex is fully developed at around $x/C = 0.83$ and induces flow curvature on the shear layer that separates from the deployed spoiler, Figure 6.23(b). Downstream of $x/C = 0.83$, the vortex moves away from the suction surface of the main-element. The vortex appears to be growing further in the radial directions such that the most outer part of the shear layer interacts with the lower surface of the deflected spoiler (Figure 6.23(c)). The vortex interacts with the suction surface of the flap, inducing strong pressure fluctuations on the flap surface. The pressure fluctuations caused by the vortex on the spoiler and flap surface have a

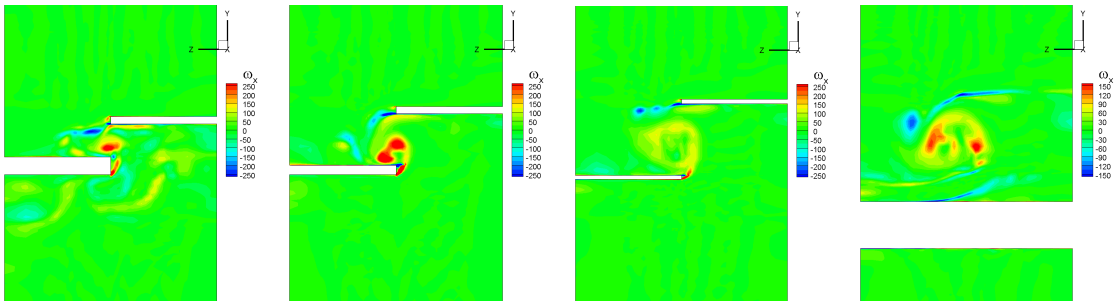

(a) $x/C = 0.78$ (b) $x/C = 0.83$ (c) $x/C = 0.88$ (d) $x/C = 0.92$

FIGURE 6.23: Contours of the streamwise vorticity, $\omega_x$, on $y - z$ planes along the side-edge vortex.

significant effect on the overall far-field noise. The details of the near- and far-field acoustics are presented in the following section.

### 6.4.3 Near-field Noise Propagation

The magnitude of the dipole source term in the FW-H equation (Equation 3.54) is proportional to the root mean square of the time derivative of surface pressure fluctuations,

$$\sqrt{\frac{1}{T_2 - T_1} \int_{T_1}^{T_2} \left[\frac{\partial p}{\partial t}\right]^2 \mathrm{d}t}. \tag{6.1}$$

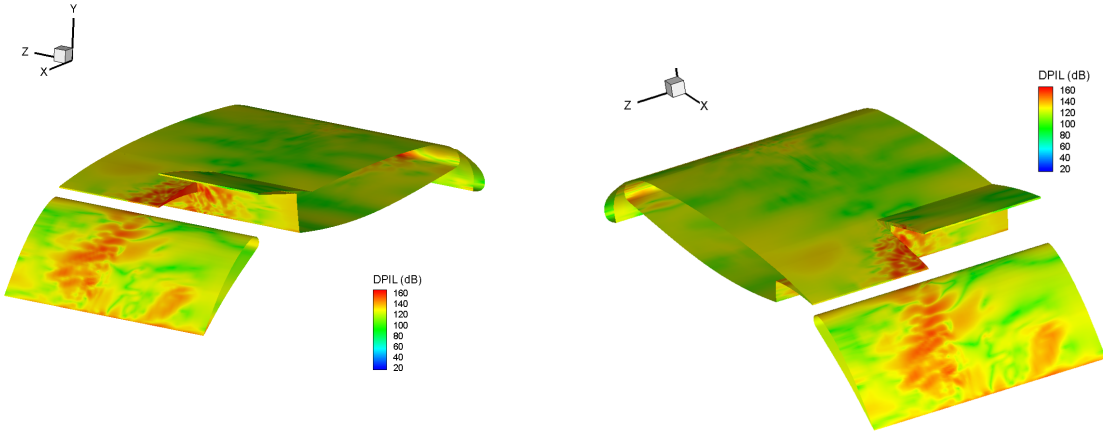


(a) (b)

FIGURE 6.24: Dipole source strength distribution on the surface of the HLD with the half-span spoiler.

The distribution of the magnitude of the surface dipole source term on the high-lift surface is shown in Figure 6.24. In order to show the distribution clearly, a decibel

scale is used, with the time Derivative of Pressure fluctuations Intensity Levels (DPIL) defined as

$$\mathrm{DPIL} = 20\log 10 \left( \frac{\sqrt{\frac{1}{T_2 - T_1} \int_{T_1}^{T_2} \left[\frac{\partial p}{\partial t}\right]^2 \mathrm{d}t}}{p_{ref}} \right), \tag{6.2}$$

where the reference pressure $p_{ref} = 2 \times 10^{-5}$ Pa.

The highest surface dipole sources occurs on the side-edge and suction surface of the main-element, where the side-edge vortex is in close proximity to the surface. Additional noise sources are found: on the side-edge of the deployed spoiler, where the vortex shear layer grazes the spoiler surface; and on the flap suction surface, where the separated side-edge vortex induces strong pressure fluctuations.

### 6.4.4 Far-field Noise Radiation

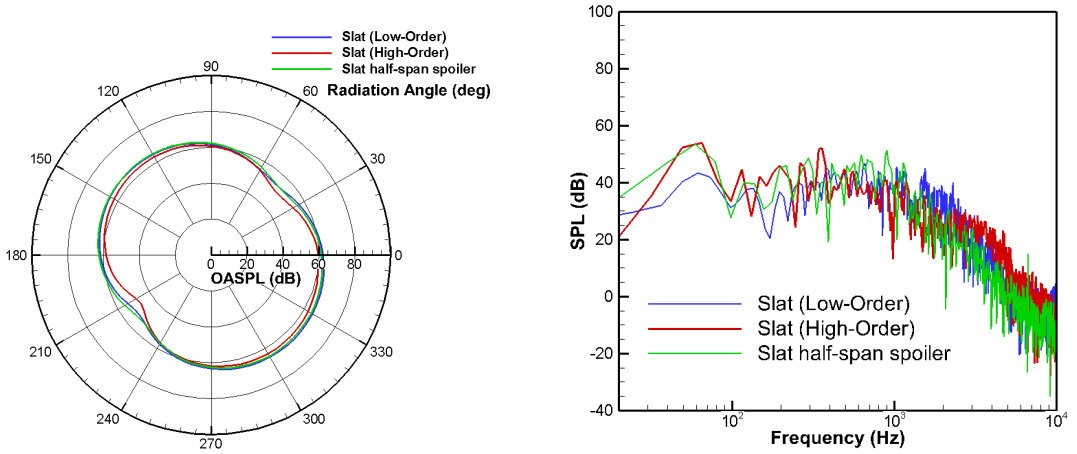


(a) Overall far-field noise directivity.

(b) Far-field noise spectra at $\theta = 270$ degrees.

FIGURE 6.25: Comparison of the far-field overall noise directivity and spectra from the slat.

Figure 6.25 shows a comparison of the slat overall noise directivity and spectra at the overhead position for the steep HLDs with the full-span and the half-span spoiler.

Figure 6.25(a) shows that the overall noise level from the slat with the half-span spoiler is the same that from the slat with the full-span spoiler. Therefore, deploying a half-span spoiler does not have a significant effect on the overall

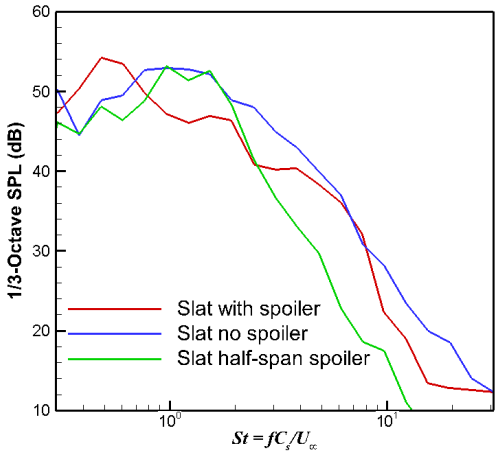


FIGURE 6.26: Comparison of the 1/3-Octave far-field noise spectra from the slat at $\theta = 270$ degrees.

noise levels from the slat. As previously observed in section 6.3, the high-order simulation predicts lower overall noise levels compared to the low-order simulations.

The slat far-field noise spectra in Figure 6.25(b) are in very good agreement. All three spectra have a peak at approximately 60 Hz which is due to the vortex shedding behind the flap.

Figure 6.26 shows the 1/3-octave noise spectra for the observer at $\theta = 270$ degrees. When the full-span spoiler is deflected, the slat noise peak occurs at $St \approx 0.5$. The slat noise peak occurs at a higher frequency $St \approx 1$ for both the half-span spoiler and no spoiler HLD configurations.

The slat on the steep high-lift configuration with a half-span spoiler deflected has two different flow regimes along its span. The deployed spoiler reduces the circulation around the slat spanwise section upstream. The reduced sectional lift affects the slat cove flow dynamics, thus resulting in a larger recirculation region in comparison to the flow in the remainder of the spanwise section of the slat. In contrast, for the section of the slat without a spoiler downstream, the slat cove does not increase in size. The aggregate of the two slat spanwise sections produces a far-field noise signature similar to the slat without the spoiler with a peak at $St \approx 1$.

The flap far-field noise directivity and spectra with the half- and full-span spoiler are compared in Figure 6.27. The far-field directivity plot shows that the overall noise level from the flap with the half-span spoiler is higher compared with the

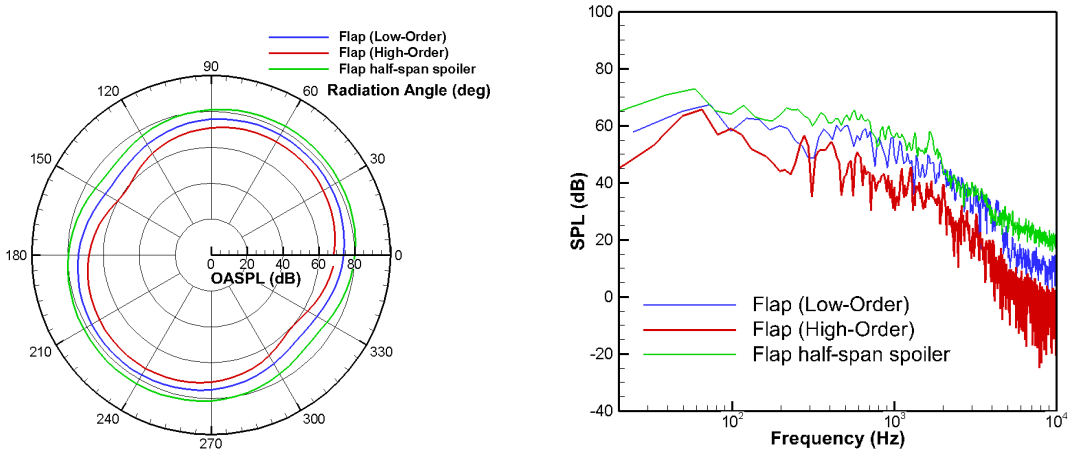


(a) Overall far-field noise directivity.

(b) Far-field noise spectra at $\theta = 270$ degrees.

FIGURE 6.27: Comparison of the far-field overall noise directivity and spectra from the flap.

full-span spoiler.

The far-field noise spectra show that the noise from the flap with the half-span spoiler is higher than the noise from the flap with the full-span spoiler over most high frequencies. The increase in noise at the high frequencies for the flap with the half-span spoiler is caused by the interaction of the large side-edge vortex with the flap suction surface.

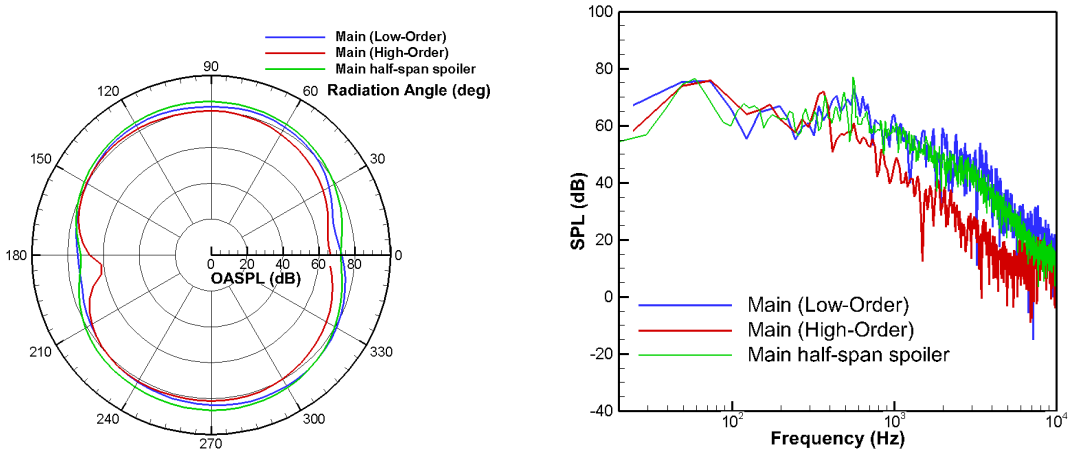


(a) Overall far-field noise directivity.

(b) Far-field noise spectra at $\theta = 270$ degrees.

FIGURE 6.28: Comparison of the far-field overall noise directivity and spectra from the main-element.

The far-field noise from the main-element with the half-span spoiler is compared to the noise from the main-element with the full-span spoiler in Figure 6.28. The

overall noise from the main-element with the half-span spoiler is higher compared with the noise from the main-element with the full-span spoiler by approximately 3 dB or less for observers in the forward quadrant $180 < \theta < 300$ degrees.

Figure 6.28(b) shows that the noise from the main-element with the half-span spoiler is the same as the noise from the full-span spoiler all frequencies. The noise spectrum of the main-element with the half-span spoiler has a peak at $f \approx 600$ Hz. The noise peak is not observed on the far-field noise spectrum from the slat and the flap.

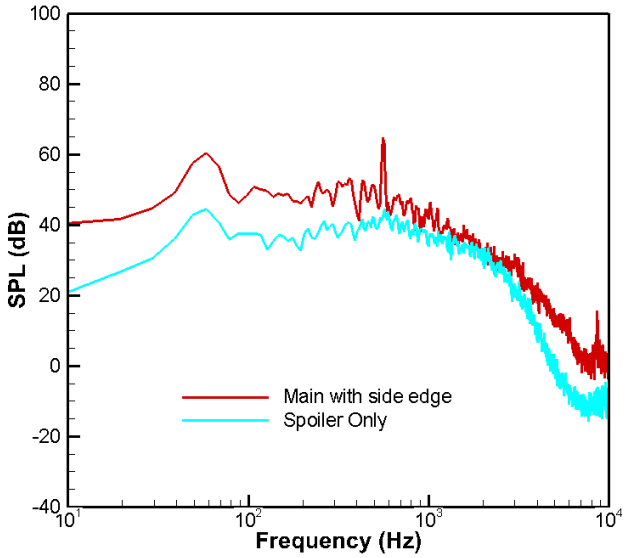


FIGURE 6.29: Comparison of the far-field noise spectra from the main-element and the isolated spoiler for the HLD with a half-span spoiler.

Figure 6.29 compares the far-field noise spectra from the main-element (including the spoiler) and the isolated half-span spoiler. The noise peak at $f \approx 600$ Hz is not observed in the far-field noise spectrum from the isolated spoiler. This suggests that the source of the noise is on the main-element.

Figure 6.30 shows the power spectral density of the pressure signal at various probes located around the spoiler side-edge. The location of the probes is shown in Figure 6.30(a). Figure 6.30(b) shows that the probe at the bottom edge of the main-element side-edge has more high frequency broadband content compared to the other location. This is where the shear layer from the lower surface of the main-element separates from the side-edge. The PSD of the surface probe located at the top surface of the main-element has a small tone at the same frequency, $f \approx 600$ Hz, that is observed in the main-element far-field spectrum. This suggests that

the source of the noise peak is located on the upper surface of the main-element near the side-edge. This is the location where the side-edge vortex emerges and interacts with the surface of the main-element.

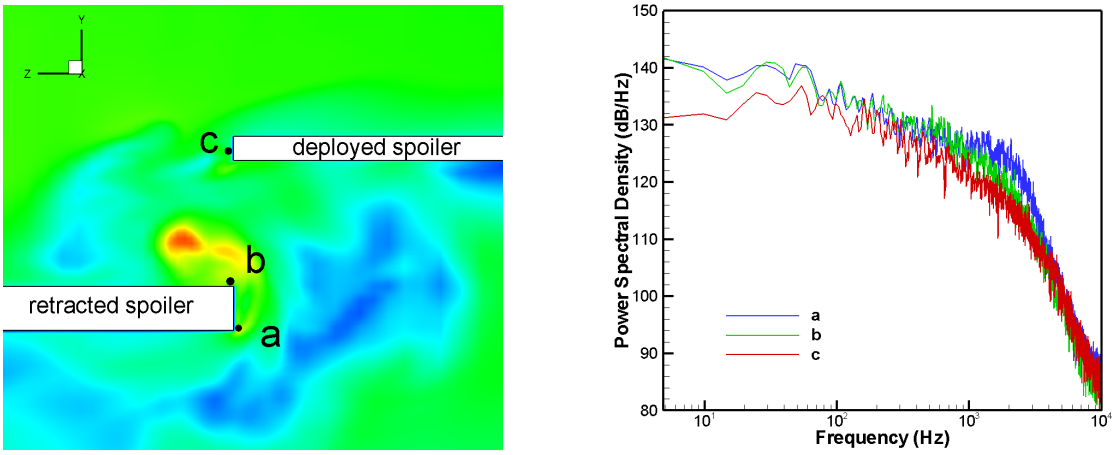


(a) Monitor locations.

(b) PSD of the signal at the monitors.

FIGURE 6.30: Power spectral density of the pressure from the probes located around the spoiler side-edge at $x/C = 0.83$.

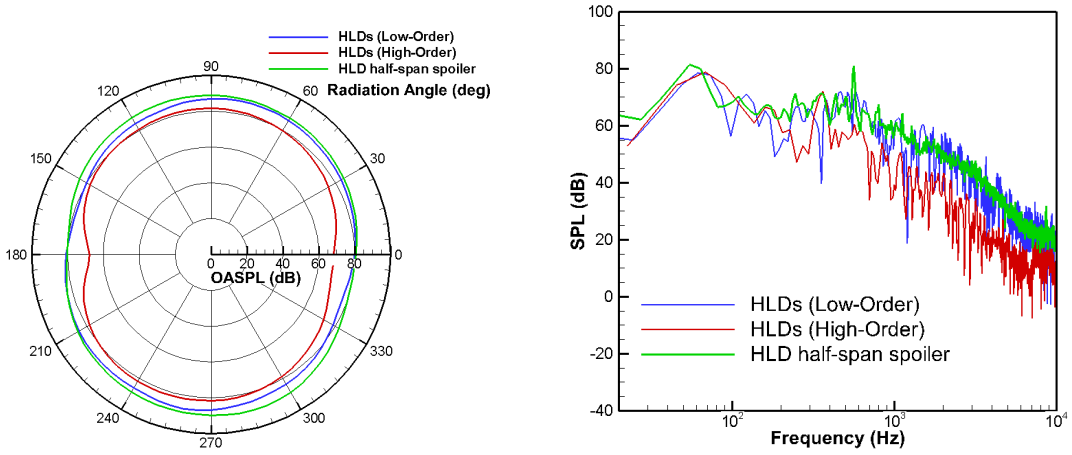


(a) Overall far-field noise directivity.

(b) Far-field noise spectra at $\theta = 270$ degrees.

FIGURE 6.31: Comparison of the far-field overall noise directivity and spectra from the HLDs.

Figure 6.31 shows a comparison of the far-field overall noise directivity from the steep HLDs. The overall noise level from the HLDs with the half-span spoiler is higher than the noise from the HLDs with the full-span spoiler.

The noise spectra at the overhead position are presented in Figure 6.31(b). The noise spectrum from the HLDs with the half-span spoiler shows a broadband noise level that is the same as the noise from the HLDs with the full-span spoiler. The

noise spectra from the HLDs with the full- and half-span spoiler have a common noise peak at frequency $f \approx 60$ Hz which is attributed to the large scale vortex shedding behind the deployed spoiler.

## 6.5 Summary

In this chapter, the results of the 3D computation of the flow around the HLD with a half-span spoiler deployed using the low-order solver are presented. The results are compared with the 3D simulation of the HLD with a full-span spoiler using the low-order and high-order solvers.

The flow field results show that the gap between the spoiler and the main-element side-edge is occupied by a strong vortex. The flow from the pressure surface of the main-element separates at the side-edge bottom corner and rolls up into a strong streamwise vortex downstream. The vortex grows in size downstream and moves on to the suction surface of the main-element. Contours of mean pressure on the surface of the high-lift model show the trajectory of the vortex on the main-element near the side-edge.

The interaction of the vortex with the surface of the main-element, the spoiler and the flap is shown to be responsible for both the tonal and broadband noise increase. Surface distribution of the dipole source strength from the FW-H equation shows strong dipole noise sources on the main-element side-edge where the vortex forms, the suction surface of the main-element and the spoiler side-edge where the tip of the vortex comes in contact with the lower edge of the spoiler. In addition, contours of the dipole source strength show high levels on the flap suction surface, arising from the pressure fluctuations induced by the separated vortex downstream of the main-element trailing edge.

Far-field noise spectra from the HLDs with the half-span spoiler show an increase in the broadband noise at high frequencies compared with the full-span configuration. The broadband noise increase on the flap is attributed to the side-edge vortex interaction with the surface of the main-element, spoiler and the flap. The interaction of the side-edge vortex with the top surface of the main-element is responsible for the tonal noise increase at $f \approx 600$ Hz.

Comparison of the slat far-field noise spectra shows that the noise peak shifts in frequency to $St = 1.0$ as a result of the different flow regimes along the span of the slat. The slat cove vortex increases in size over the section with the spoiler

due to the reduction in circulation whereas the slat cove size is unchanged along the section of the slat that is not upstream of the spoiler.

The far-field noise spectra from both the HLD with the full- and half-span spoilers show a dominant noise peak at a frequency of $f = 60$ Hz, which is attributed to the large scale vortex shedding downstream of the deployed spoiler and flap.

The 3D simulations have captured the unsteady flow field around the side-edge of the spoiler and show that it has significant effects on the near-field and far-field acoustics.

Based on the understanding of the spoiler noise mechanisms gained from the 2D and 3D simulations of the preceding chapters, a noise reduction treatment is recommended in Appendix A. A preliminary 2D simulation is performed and the flow field and far-field acoustics results are presented and compared. The results demonstrate the potential of the noise treatment in reducing the noise impact of the spoiler. However, further work is required to optimise the noise treatment to get the best aerodynamic and acoustic performance.

# Chapter 7

# Conclusions and Recommendations

## 7.1 Conclusions

A numerical investigation has been performed of the aerodynamics and aeroacoustics of a deflected spoiler during steep approach as part of a new operational procedure to alleviate noise pollution.

The aims of the research area to understand the noise generation mechanisms of the high-lift wing with a deflected spoiler and to recommend a noise reduction treatment for aircraft in steep approach.

A hybrid strategy is used to compute the far-field noise using the Ffowcs-Williams and Hawking integral method. Two- and three-dimensional simulations of the flow field around the high-lift configurations have been performed. In total, computations are performed on three different HLDs configurations: the HLDs without the spoiler, the HLDs with a full-span spoiler and the HLDs with a half-span spoiler.

A high-order solver, employing $4^{\text{th}}$-order spatial numerical scheme, is used to simulation the flow around the 2D and 3D conventional and steep HLDs. For the simulation of the HLD with a half-span spoiler, a low-order finite volume solver is used, which employs $2^{\text{nd}}$-order spatial scheme.

The following is summary of the main findings from the current study.

The flow-field results from the 2D and 3D simulations show that deploying the spoiler causes the slat cove vortex to expand due to the reduced flow incidence at the slat leading edge.

The 2D simulations show that the larger slat cove vortex causes the flow to separate at the main-element leading edge. The frequency of the vortex shedding at the main-element leading edge is twice the frequency of vortex shedding from the slat cusp. Contours of vorticity around the slat with the spoiler deployed, show that there is a clear link between the flow unsteady dynamics at the slat cusp and the main-element leading edge. The shedding of vortices from the main-element coincided with the passage of vortices from the slat cusp.

In contrast to the 2D simulations, 3D simulations did not predict the flow separation at the main-element leading edge. The 3D simulations predict a favourable pressure gradient at the main-element leading edge whereas the 2D simulations predict a very strong pressure gradient. For the 2D simulations, the boundary layer is unable to overcome the strong negative pressure gradient, thus resulting in flow separation.

The 2D and 3D simulations results show that the flow separates from the suction surface of the flap at the leading edge when the spoiler is deployed, whereas in the absence of the spoiler, the flow separation is delayed and occurs close to the mid-chord position. Vortex shedding occurs behind the flap trailing edge in the conventional and steep HLD configuration. The frequency of vortex shedding from the flap trailing edge reduces by a factor of 2 when the spoiler is deployed.

The lift and drag forces on the HLDs fluctuate at the same frequency as the vortex shedding from the flap. Deploying the spoiler increases the drag by a factor of approximately 2 while the lift is reduced by a factor of approximately 0.5. The fluctuations in the lift and drag increase when the spoiler is deployed.

The 3D simulation of the flow around the high-lift configuration with a half-span spoiler shows that a streamwise vortex occupies the region between the deployed spoiler and the main-element, similar to the vortex on a flap side-edge. The interaction of the streamwise vortex with the edge of the spoiler and the main-element is shown to be a source of high frequency broadband and tonal noise. The distribution of the dipole source strength from the FW-H equation on the surface of the high-lift configuration shows high source strength levels on the spoiler and the main-element where the vortex interacts with the surface.

The impact of a spoiler on the overall high-lift noise is an increase in noise level.

The results from the 2D and 3D simulations show that the maximum noise increase occurs at low frequency $f \approx 60$ Hz. The noise at $f \approx 60$ Hz is due to the vortex shedding from the spoiler and flap. The Strouhal number based on the flap chord is $St \approx 0.16$.

The far-field results from the 2D simulations show that, in addition to the broadband noise increase, deploying the spoiler results in strong tonal noise increase. When the spoiler is deployed, the noise spectra from the HLD has tonal noise components at $St = 3.6$ based on the slat chord length. The frequency of the noise peak agrees very well with the frequency of vortex shedding from the main element leading edge separation bubble. In addition there is a peak in the noise spectra at a frequency $St = 0.16$ based on the spoiler blunt trailing edge thickness. The source of this tonal noise is the vortex shedding from the spoiler trailing edge.

The far-field results from the high-order 3D simulations did not capture the two tonal components from the 2D noise spectra. This is because the 3D simulation did not predict the flow separation from the main-element leading edge and the vortex shedding from the spoiler trailing edge. One of the reasons for the discrepancies is the reduced resolution of the 3D grids in the $x-y$ planes. The number of grid point in the $x-y$ plane is reduced by up to 60% in order to reduce the computational time and resource requirements. The different turbulence models used may also contribute to the observed difference in the flow features, since the low-order 3D simulation also did not predict the flow separation at the main-element. However the low-order 3D simulation is able to capture the vortex shedding from the spoiler trailing edge.

The 3D simulations have highlighted the importance of getting the $x-y$ grid profile resolution right in order to resolve the details of the 3D flow field. The 3D simulations using the high-order solver use very coarse grids in the $x-y$ profile thus suffer from a lack of small scale turbulence structures details. However, increasing the grid resolution in the $x-y$ profile increases the computational time and resources required. Therefore a critical balance needs to be established in order to capture small scale details within manageable time and resources constraints.

One strategy to reduce the noise due to the spoiler is to reduce or eliminate the low frequency vortex shedding behind the spoiler. Initial 2D simulations have shown that perforations on the spoiler can eliminate the low frequency vortex shedding. The perforations work by allowing air to bleed through the holes therefore prevent the shear layers separated from the top and bottom edges from interacting to form

vortices.

Far-field noise spectrum shows that the perforations significantly reduces the low frequency noise due to the vortex shedding behind the spoiler and flap. However they also boost noise at non-dimensional frequency of $St \approx 0.2$ based on diameter of the holes. The perforations also reduce the drag generated by the spoiler, thus reducing the effectiveness of the spoiler as an air brake.

## 7.2 Future Recommendations

The current work has highlighted the need for further computation of the spoiler noise reduction treatment. The 2D simulations performed as part of this research shows that the flow behind the perforations is turbulent with very small scale structures. In order to better understand the turbulent flow field, simulations of the 3D flow field around the perforations can be performed using DES or hybrid RANS/LES turbulence models capable of resolving the small scale structures behind the perforations.

The 2D simulations are performed for a uniformly perforated plate of 40% porosity. Previous tests by de Bray [46] showed that the most effective configuration is a centrally perforated plate with a porosity of 20%. Further 2D simulations may be performed with different porosity in order to identify an optimal porosity for further 3D simulations.

In addition to the above simulations, a feasibility study can be performed of the implementation of the perforated spoilers on real aircraft, with considerations including the aerodynamic performance, weight and structural constraints.

The development of a physics-based spoiler noise prediction model. The first stage of the work would involve performing simulations of the steep configuration with different geometrical settings. The parameters of most interest to the spoiler noise are; the spoiler deflection angle, the high-lift angle of attack, and the freestream velocity. Statistical regression analysis can be applied to determine trends. The model can include the noise impact of the spoiler on the slat and flap noise, thus forming a full high-lift noise prediction model for steep approach.

Finally the noise prediction model can be used to optimise steep approach trajectory parameters such as glide angle, approach speed, spoiler deflection, and

the point of deploying the spoiler in order to further reduce the noise on the ground.

## 7.3 Dissemination

This work has been presented at the 16th AIAA/CEAS Aeroacoustic Conference on 9th June 2010 in Stockholm, Sweden [75].

# Appendix A

# 2D Simulation of Spoiler Noise Reduction

## A.1 Introduction

In this Appendix the preliminary computations of a noise reduction treatment for spoiler noise during steep approach is discussed. A 2D simulation is performed of the flow around a perforated spoiler. The flowfield and far-field acoustics are compared with the 2D simulation of the solid spoiler in Chapter 4.

## A.2 2D Simulation of Perforated Spoiler

The results of the 2D URANS simulation of steep HLDs with a perforated spoiler is presented. The results include aerodynamic forces and flowfield plots. The simulations are performed using a second-order finite volume commercial CFD code.

### A.2.1 Grid and Flow Conditions

The high-lift geometry used in the simulation is identical to the HLD configuration used in the 2D simulations in Chapter 4, consisting of the slat and the flap deployed at 30 and 38 degrees respectively. In contrast to the configuration in Chapter 4, the perforated spoiler is deflected at an angle of 60 degrees. The spoiler deflection

angle is chosen in order to increase the drag to a level comparable with the solid spoiler. The perforated spoiler has a porosity of 40%. The porosity is based on the findings of de Bray [46]. In addition, to improve the effectiveness of the bleed air on the flow downstream of the spoiler, the main-element trailing edge is included in the simulation. A fully structured grid, with similar topology as in the previous 2D

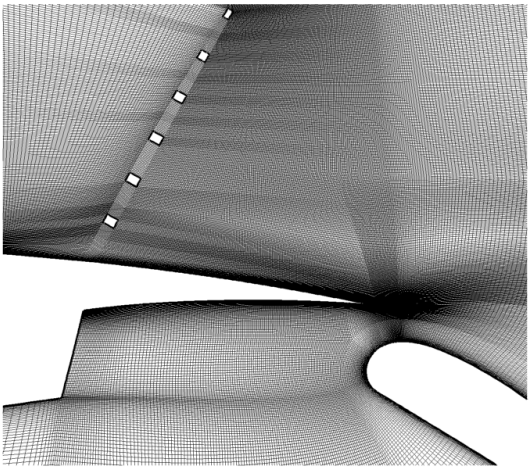

FIGURE A.1: A close-up of the grid around the perforated spoiler.

simulation, is generated around the high-lift configuration consisting of $3.25 \times 10^5$ cells. Figure A.1 shows a close-up of the grid around the perforated spoiler. A fine grid is used to resolve the turbulent flow through the perforations and the wake of the spoiler. The chord length of the spoiler is $11\%C$, therefore at 40% porosity the following expression gives the diameter of the holes, $h = 0.4 * 0.11/N$, where $N$ is the number of holes which in Figure A.1 is 6. The hole diameter $D = 7 \times 10^{-3}$ m.

The flow conditions used are identical to the 2D simulation of Chapter 4. The adiabatic no-slip wall boundary condition is used on the surface of the HLDs including the perforated spoiler, whereas the non-reflecting pressure far-field boundary condition is used on the streamwise domain extent.

### A.2.2 Results and Discussion

In this section the results of the 2D simulation of the flow around the HLDs with the perforated spoiler is presented. The flow field and far-field results are compared with the 2D simulation of the HLDs with a solid spoiler to assess the potential of perforations in reducing noise from the steep HLDs.

### A.2.2.1 Time Averaged Flow

The mean pressure distribution around the HLDs with a perforated spoiler is compared with the pressure distribution around the conventional and steep HLD configurations from Chapter 4 in Figure A.2. The pressure distribution on the HLD with the perforated spoiler compares closely with the conventional HLD configuration.

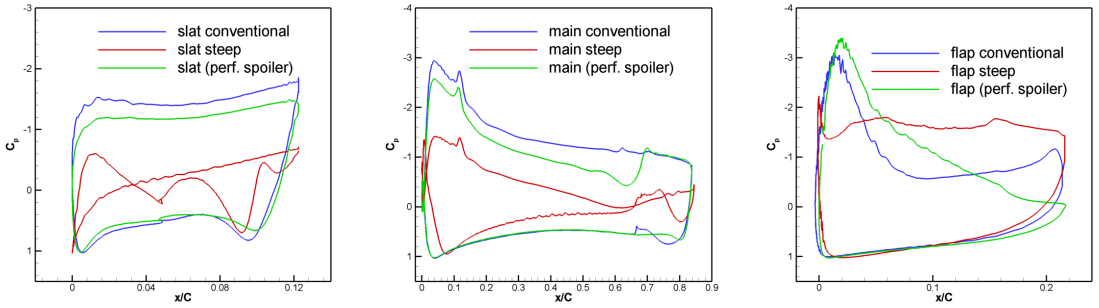


(a) Slat. (b) main-element. (c) Flap.

FIGURE A.2: Comparison of the mean pressure distribution around the HLD configurations.

Figure A.2 show a recovery of the pressure distribution on the three high-lift elements towards the pressure distribution of the conventional high-lift configuration. Deflecting a perforated spoiler has a relatively small effect on the circulation around the HLDs compared to the solid spoiler.

TABLE A.1: Comparison of the mean lift and drag coefficient of the HLD configurations.

| **HLD configuration** | $C_L$ | $C_D$ |
|---|---|---|
| Conventional | 2.23 | 0.20 |
| Steep with solid spoiler | 1.00 | 0.40 |
| Steep with perforated spoiler | 1.80 | 0.25 |

Table A.1 compares the mean lift and drag coefficient for the three HLD configurations. The perforated spoiler causes a 20% loss in lift, whereas the solid spoiler caused a 55% loss in lift compared to the conventional configuration. However, the solid spoiler causes an increase in the drag of 100%, whereas the perforated spoiler increase the drag by 25% compared to the conventional high-lift configuration.

The loss in lift when the perforated spoiler is deflected is a desirable effect. This means that only a small change to the approach velocity or angle attack is required

to meet the maximum lift requirement for safety during landing. A large increase in the approach velocity and/or the angle attack would result in an increase in noise.

#### A.2.2.2 Instantaneous Flow Field

Figure A.3 shows the instantaneous flow streamlines around the HLD configuration with the perforated spoiler. The flow behind the perforations is unsteady, with vortex shedding from the gaps between the holes. The flow quickly straightens downstream of the perforations such that the flow over the flap is unaffected by the perforations upstream. There is no evidence of vortex shedding from the flap as is the case with a solid spoiler. The boundary layer on the flap surface does not separate until about 85% of the flap chord length. A small recirculation region appears from 85% to the trailing edge of the flap.

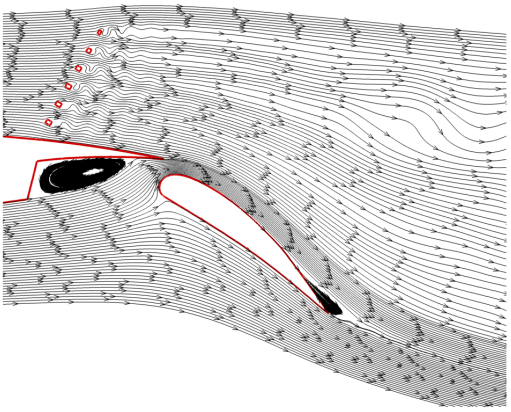

FIGURE A.3: Instantaneous flow streamlines around the perforated spoiler and flap region.

Figure A.4 compares contours of the spanwise vorticity $\omega_z$ distribution behind the solid and perforated spoiler. The vortical structures behind the spoiler disappeared when perforations are introduced. This is clear evidence that air flow through the perforations eliminates the vortex shedding behind the spoiler. The perforations also have an effect on the flow on the flap. The flow remains attached over a large proportion of the flap suction surface.

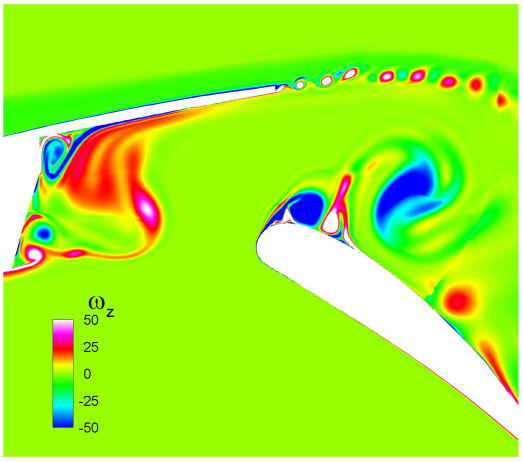


(a) Steep configuration with solid spoiler.

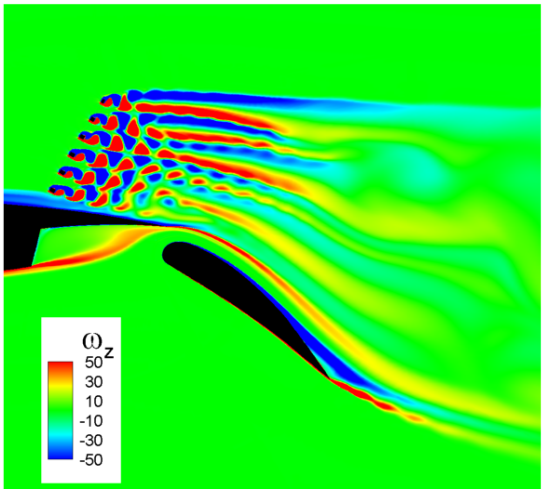


(b) Steep configuration with perforated spoiler.

FIGURE A.4: Instantaneous spanwise vorticity field around the HLDs with solid and perforated spoiler.

## A.3 Far-field Noise

Figure A.5 shows a comparison of the noise spectra at the overhead position from the HLD configuration with the solid and the perforated spoilers. The perforations on the spoiler significantly reduces the noise for frequencies below 800 Hz. The noise peak at frequency of $f = 60$ Hz due to the large scale vortex shedding is reduced by up to 20 dB. However, the perforations causes a broad noise peak increase at a frequency $f = 2.5$ kHz. The peak is attributed to the air flow through the perforations. The contours of spanwise vorticity in Figure A.4(b) clearly show the vortex shedding behind the perforations.

The PSD of the pressure signal at monitor points behind the perforated spoiler are

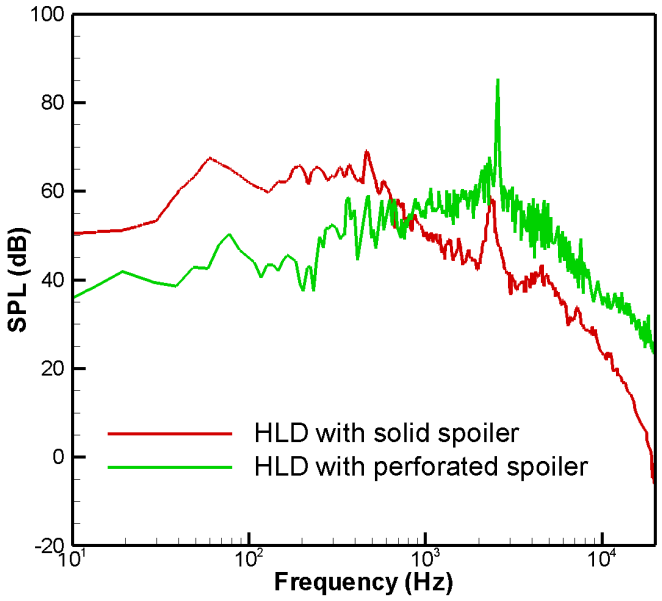


FIGURE A.5: Comparison of the noise spectra at the overhead position from the steep HLD with a solid and a perforated spoiler.

shown in Figure A.6. The monitor probes are located behind the holes, behind the spoiler in between two adjacent holes and downstream of the spoiler. All the power spectral density shows a peak at $f = 2.5$ kHz. The frequency of the peak corresponds to a Strouhal number, $St = fD/U_\infty = 0.223$, where $U = 80$ m/s and the hole diameter $D = 7 \times 10^{-3}$ m. All the spectra shows a large peak at $St = 0.22$, followed by several peaks at integer multiple of this fundamental frequency, confirming the occurrence of vortex shedding. This results shows that the noise peak in Figure A.5 is therefore due to the vortex shedding behind the perforations. The fact that the frequency of the noise peak is approximately the same as the noise peak from the HLD with solid spoiler seems only a coincident in this case, the different flow mechanism are responsible for the each individual peak.

The noise peak can be shifted to higher frequencies by reducing the diameter of the holes. However, reducing the diameter of the holes would result in a reduction of the bleed air from the spoiler and hence a reduction in the effectiveness of the perforations in breaking the large scale vortex structures behind the spoiler. The optimisation of the hole diameter for acoustic and aerodynamic performance is beyond the scope of the current work.

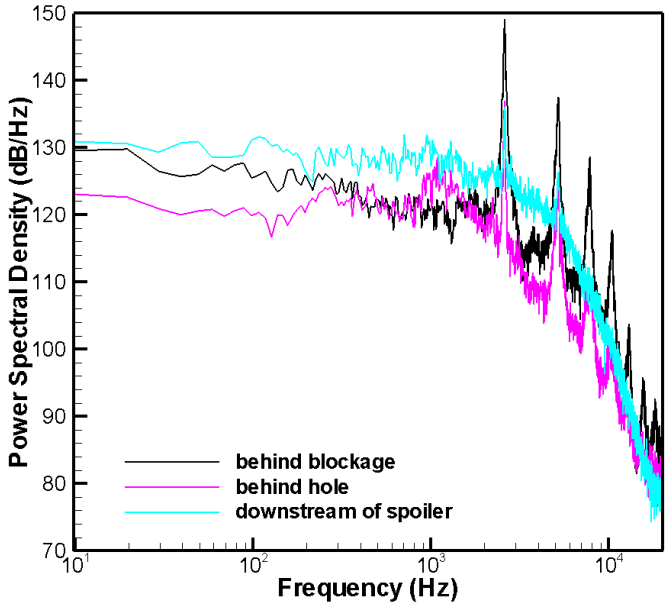


FIGURE A.6: Power spectral density of the pressure signal at the monitor point downstream of the perforated spoiler.

## A.4 Summary

The low frequency vortex shedding behind the spoiler is identified as the major noise generation mechanism for the steep configuration. A means of eliminating the vortex shedding from behind the spoiler is developed. Previous experiments show that perforations are very effective in reducing and eliminating the vortex shedding behind flat plates.

A 2D simulation is performed to demonstrate the effectiveness of perforations in reducing the vortex shedding behind the spoiler. The results shows that the perforations in the spoiler completely eliminate the low frequency vortex shedding observed on the solid spoiler.

Comparison of the lift and drag forces show that the perforated spoiler causes only a 30% more loss in lift compared with the solid spoiler. However, the perforated spoiler generates 75% less drag compared with the solid spoiler.

The far field noise spectra show a significant noise reduction at frequencies below 800 Hz and with the noise at $f = 60$ Hz reduced by up to 20 dB. However, the vortex shedding behind the holes in the spoiler also causes a broadband peak centered at $St = 0.22$, based on the hole diameter. The power spectral density of pressure probes located downstream of the spoiler also show peak at harmonics of the fundamental frequency. The noise peak can be shifted to higher frequency by

optimisation of the diameter of the holes. Further work to optimise the perforation for acoustic and aerodynamic performance is beyond the scope of the current work.

# Appendix B

# Validation of the High-Order Code

In this appendix the validation of the SotonCAA and FW-H code is presented. The problems chosen represent the wide variety of aeroacoustic phenomena which the code should be able to simulate, which includes linear and non-linear propagation of acoustic waves. The specific problems that have been considered are: the noise radiated by a monopole, the propagation of an acoustic pulse through a skewed block interface, and the scattering of sound by a circular cylinder.

## B.1 Monopole Radiation

The following test case is used to demonstrate the accuracy of the FW-H acoustic code (see Section 3.3) used in the current study. The field from a monopole source is computed in the farfield using the FW-H acoustic code. The complex potential for the monopole flow is given in [76] as

$$\phi(x, y, z, t) = A\frac{1}{4\pi r}\exp^{i(\omega t - kr)}, \tag{B.1}$$

where $r = \sqrt{x^2 + y^2 + z^2}$ is the distance between the source and observer. The variables required by the FW-H code are obtained from the real parts of

$$p^{'} = -\rho_0\frac{\partial \phi}{\partial t}, \tag{B.2}$$

$$u' = \frac{\partial \phi}{\partial x}, \tag{B.3}$$

$$v' = \frac{\partial \phi}{\partial y}, \tag{B.4}$$

$$w' = \frac{\partial \phi}{\partial z}, \tag{B.5}$$

and

$$\rho' = \frac{p'}{c_0^2}. \tag{B.6}$$

The following constants are defined as $\omega = 4\pi/46$ and $A = 0.1$. The integration surface is a circle centred at $x = 0$ and $y = 0$ with radius of 5 units and extended in the $z$-direction from $z = -5$ to $z = 5$. The circumference of the circle is divided into 200 panels and in the $z$-direction, the integration surface is divided into 20 panels. A comparison of the computed pressure history at (50,0,0) and the analytical solution obtained using Equation B.2 is given in Figure B.1. The agreement between the computed results and the analytical results is very good. Identical results are obtained from observers at different positions on the circle of radius 50 unit lengths away.

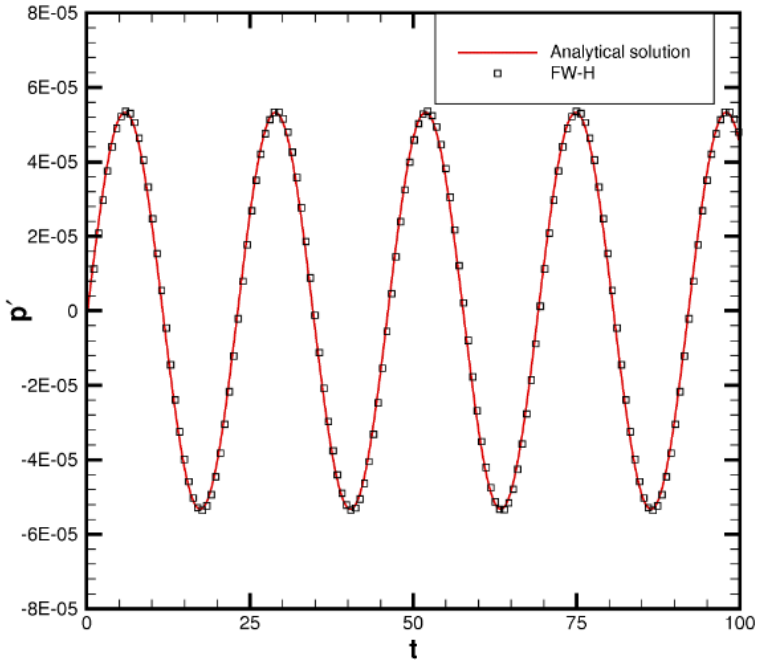


FIGURE B.1: Comparison of the computed pressure history at (50,0,0) and the analytical solution for a stationary monopole.

## B.2 Gaussian Pulse Propagation

The test of the two-dimensional Gaussian pulse propagation is used to validate the overall order of accuracy and the performance of the characteristic interface conditions applied at internal boundaries. The Euler equations are used to solve an initial value problem at $t = 0$ given by

$$p' = p - p_0 = A\text{exp}\left[-\text{In2}\left(\frac{x^2 + y^2}{9}\right)\right] \tag{B.7}$$

$$u' = 0, v' = 0, \rho' = p' \tag{B.8}$$

where $u'$ and $v'$ are the velocity perturbations in the $x$ and $y$ directions and $A$ is pulse amplitude. The freestream Mach number is $M_x = 0.5$ and the amplitude is set to $A = 0.001$. A small amplitude is chosen so that the solution can be compared to the linearised solution. The analytical solution of the linearised Euler equations corresponding to this problem is given in [77].

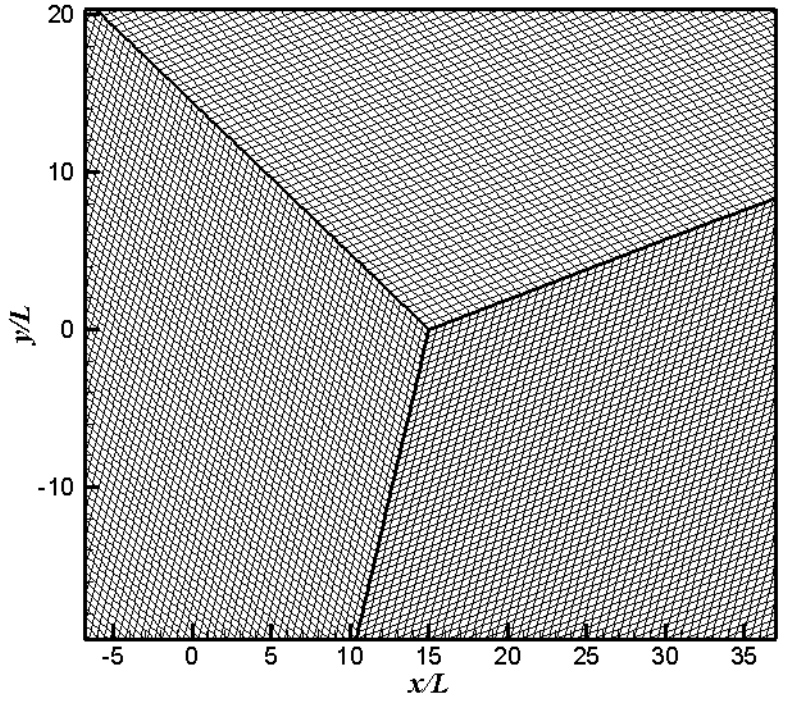


FIGURE B.2: A close-up of the mesh across the boundary of the 3 skewed blocks.

The pressure distribution is solved on a highly skewed 3 block grid to demonstrate the performance of the characteristic interface condition applied along the skewed grid interface. To asses the spatial accuracy of the numerical scheme, the Euler equations are solved on 3 meshes of different levels of spatial resolution (200 by 200, 150 by 150 and 100 by 100). Figure B.2 shows the finest mesh at the boundary

between the three blocks. A small time step is chosen $\Delta t = 0.25L/c_0$ corresponding to a CFL number of 0.7. The number of sub-iterations in the implicit time stepping scheme is set to 5. The simulation is run for 120 time steps to reach a non-dimensional time of 30.

Figure B.3 shows the pressure distribution at the non-dimensional time of 30 on the finest grid. The pulse was initiated at (0,0) and convected at Mach number $M = 0.5$ in the $x$ direction. The pressure field shows that the acoustic waves can propagate across the skewed block boundary without distortion or amplification. A pressure monitors is located near the vertex shared by the 3 blocks at (20.326,-0.067). Figure B.4 compares the time history of pressure at this location obtained on the three mesh sizes with the analytical solution. The results show good agreement with analytical solution for all three meshes. The order of accuracy of the numerical scheme is obtained by a linear least square fitting of the maximum error of the calculated pressure at position (20.326,-0.067) on the different grids, Figure B.5. The order of accuracy of the numerical scheme is 3.67, determined from the slope of the curve in Figure B.5. This is close to the expected spatial order of accuracy of 4. The discrepancy can be explained by the use of one-side stencils of reduced order close to the boundary for the characteristic interface condition.

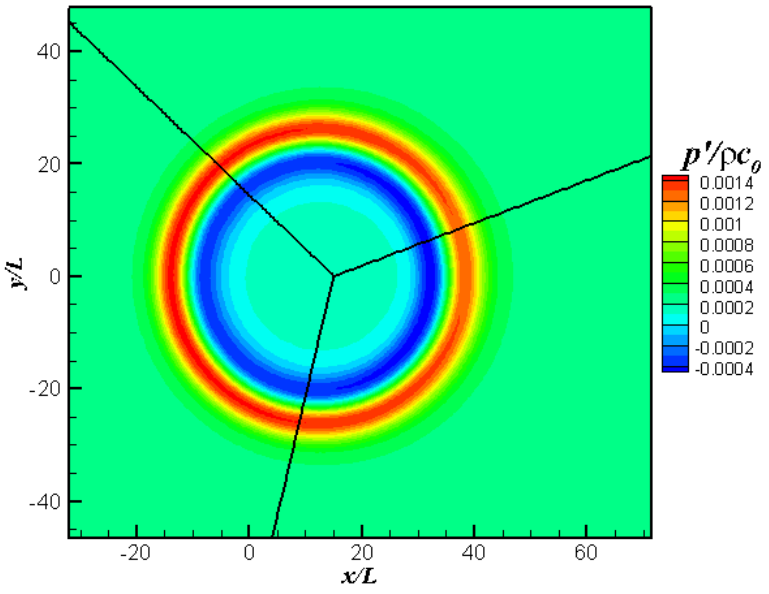


FIGURE B.3: Non-dimensional pressure distribution at a non-dimensional time step of $tc_0/L = 30$ obtained across a highly skewed 3 block.

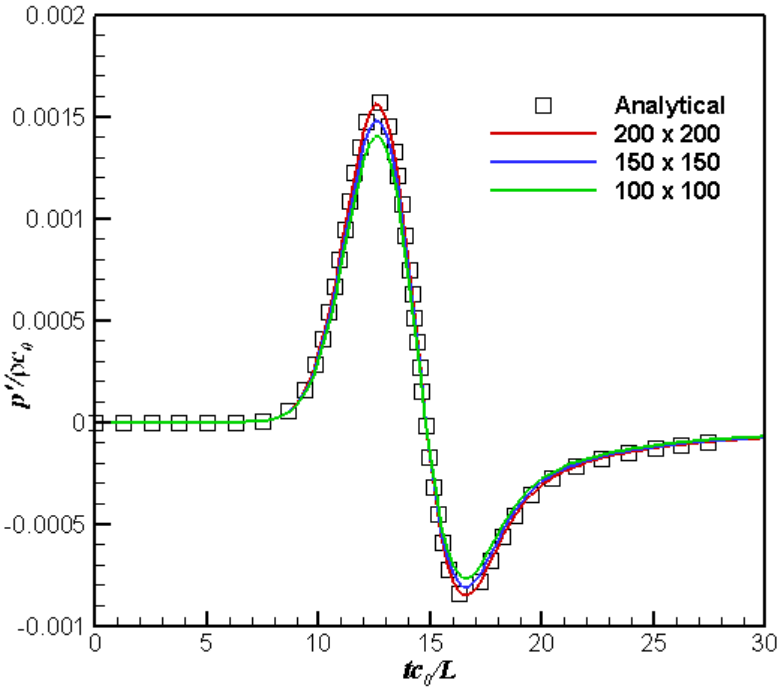


FIGURE B.4: Comparison of the time history of pressure obtained on the three different meshes at position (20.326,-0.067).

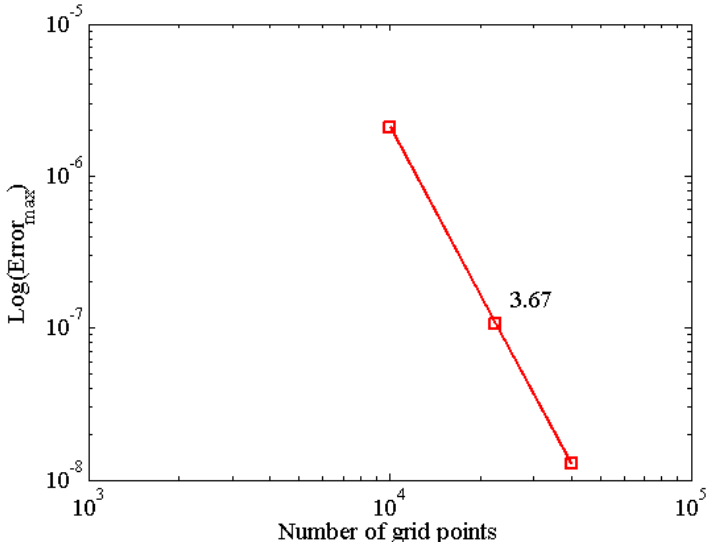


FIGURE B.5: The maximum error of the solution on the three different meshes.

## B.3 Acoustic Wave Scattering by Cylinder

The following case study is used to demonstrate the accuracy of the high-order code and the performance of the explicit buffer zone boundary conditions. The case study is a two-dimensional acoustic scattering problem from the Second CAA workshop [78]. The physical problem models how sound from a propeller is scattered by the fuselage of an aircraft. The propeller is modelled as a line source,

whereas the fuselage is modelled as a cylinder, thus reducing the problem to two-dimensional computation. The cylinder has a radius of $R$=0.5 and is located at the origin (0,0). At time $t$=0, the following initial conditions are prescribed:

$$u = v = 0, \tag{B.9}$$

$$p(x, y, 0) = \exp\left[-\ln 2\left(\frac{(x-4)^2 + y^2}{0.2^2}\right)\right]. \tag{B.10}$$

The solution is obtained by solving the linearized Euler equation using the computational grid shown in Figure B.6. The number of points in the radial and azimuthal directions are 90 and 150 respectively. The time step is chosen such that the CFL number is 1.0. A characteristic wall boundary condition is applied on the cylinder surface and an explicit buffer zone boundary condition is applied on the extent of the computational domain.

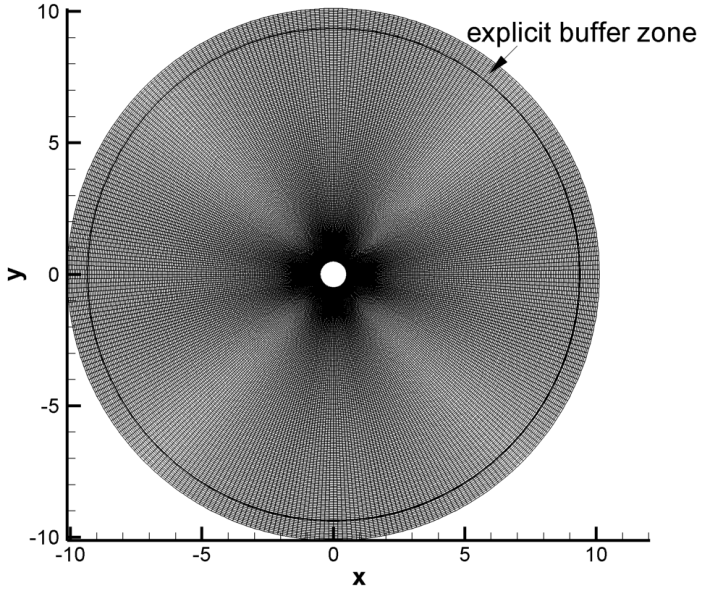


FIGURE B.6: Computational grid for the acoustic scattering problem showing location of the explicit buffer zone boundary conditions.

The damping coefficient $\sigma_{bz}$ is given by

$$\sigma_{bz}(x_{bz}) = \alpha_{bz}\left(1 + \frac{x_{bz} - L_{bz}}{L_{bz}}\right)^{\beta_{bz}} \tag{B.11}$$

The following values for the constants are used: $\alpha_{bz} = 1.0$, $\beta_{bz} = 1.5$ and the buffer width $L_{bz} = 20$ points.

In Figure B.7, contours of fluctuating pressure show the propagation of the acoustic waves and the scattering by the circular cylinder. At the buffer zone region the acoustic waves are explicitly damped without any spurious reflections.

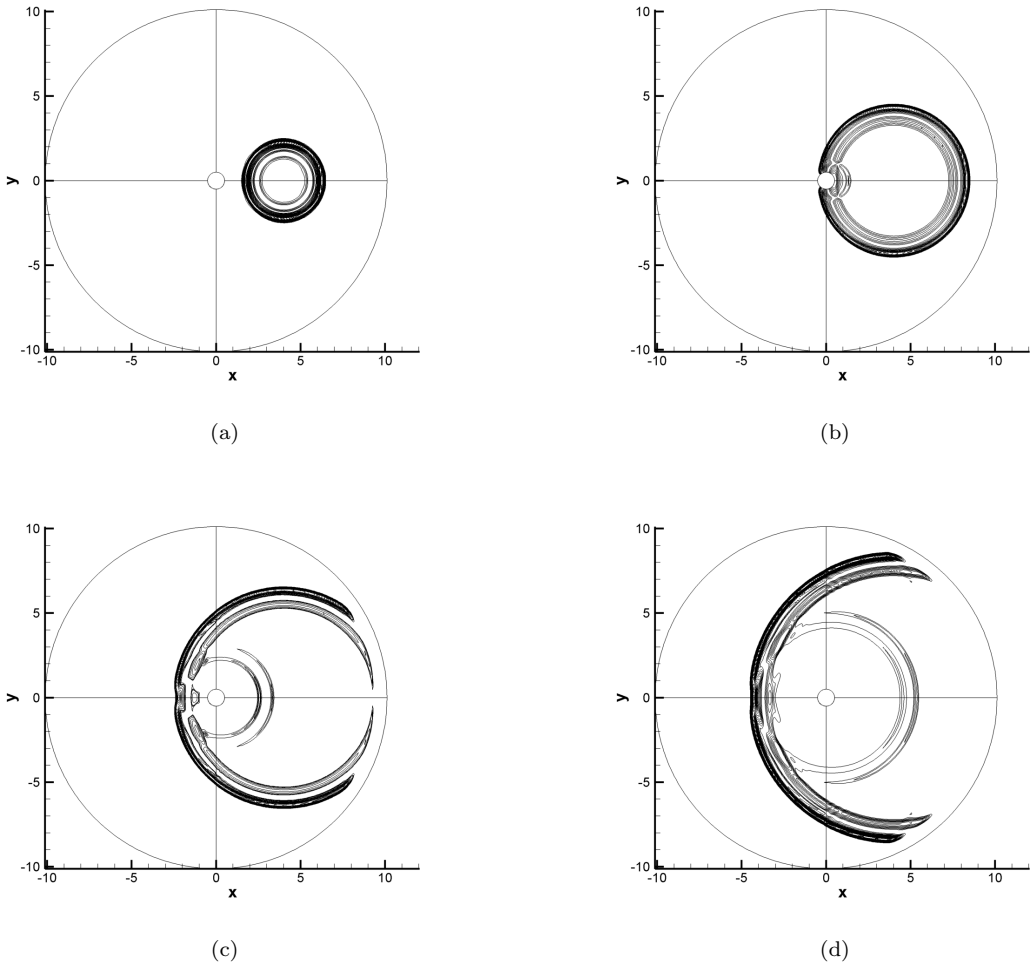


(a) (b)

(c) (d)

FIGURE B.7: Pressure contours showing the scattering of acoustic wave by a cylinder and the performance of the explicit buffer zone boundary condition in suppressing spurious reflections.

Figure B.8 shows a comparison between the numerical solution and the exact solution at a location $r$= 5, $\theta$= 90 degrees. The agreement between the solutions highlight the accuracy of the numerical scheme used in SotonCAA. The numerical scheme employed in SotonCAA are capable of capturing the propagation and the scattering of sound waves from a circular cylinder. In addition, the buffer zone boundary conditions have been shown to prevent spurious reflection as acoustic waves exit the computational domain.

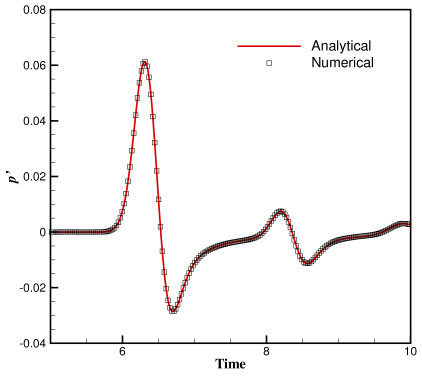


(a) $r = 5.0$, $\theta = 90$ degrees

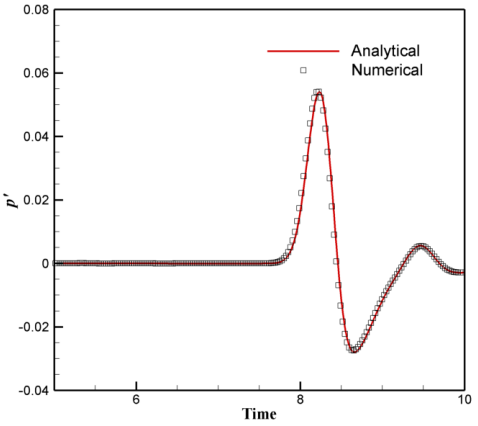


(b) $r = 5.0$, $\theta = 135$ degrees

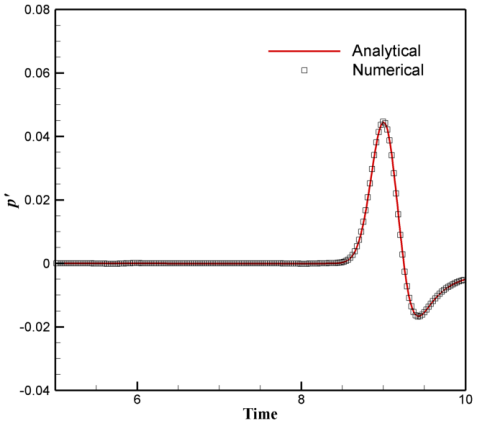


(c) $r = 5.0$, $\theta = 180$ degrees

FIGURE B.8: Comparison of the numerical solution and the exact solution at 3 different location from $t = 5$ to $t = 10$.

# Bibliography


[1] Crighton, D., "Airframe Noise," *Aeroacoutics of Flight Vehicles: Theory and Practice*, edited by H. H. Hubbard, Vol. 1, NASA RP 1258, 1991, pp. 391–443.

[2] Antoine, N. and Kroo, I., "Aircraft Optimization For Minimal Environmental Impact," *Journal of Aircraft*, Vol. 41, No. 4, 2004, pp. 790–797.

[3] Clarke, J. B., Ho, N. T., Ren, L., Brown, J. A., Elmer, K. R., Tong, K. O., and Wat, J. K., "Continuous Descent Approach: Design and Flight Test for Louisville International Airport," *Journal of Aircraft*, Vol. 41, No. 5, 2004, pp. 1054–1066.

[4] Dobrzynski, W., "Almost 40 Years of Airframe Noise Research - What did we Achieve?" *Journal of Aircraft*, Vol. 47, No. 2, March-April 2010, pp. 353–367.

[5] Kipersztok, O. and Sengupta, G., "Flight Test of the 747-JT9D for Airframe Noise," *Journal of Aircraft*, Vol. 19, No. 12, 1982, pp. 1061–1069.

[6] Williams, J. F. and Hawkings, D., "Sound Generation by Turbulence and Surfaces in Arbitrary Motion," *Philosophical Transactions for the Royal Society of London, Series A, Mathematical and Physical Sciences*, Vol. 264, No. 1151, 1969, pp. 321–324.

[7] Fink, M. and Schlinker, R., "Airframe Noise Component Interaction Studies," *Journal of Aircraft*, Vol. 17, No. 2, 1980, pp. 99–105.

[8] Dobrzynski, W., Nagakura, K., Gehlhar, B., and Buschbaum, A., "Airframe Noise Studies on Wings With Deployed High-lift Devices," AIAA Paper 98-2337, 1998.

[9] Dobrzynski, W., Gehlhar, B., and Buchholz, H., "Model and Full Scale High-Lift Wing Wind Tunnel Experiments Dedicated to Airframe Noise Reduction," *Aerospace Science Technology*, Vol. 5, 2001, pp. 27–33.

[10] Guo, Y. and Joshi, M., "Noise Characteristics of Aircraft High Lift Systems," *AIAA Journal*, Vol. 41, No. 7, 2003, pp. 1247–1256.

[11] Dobrzynski, W. and Pott-Pollenske, M., "Slat Noise Source Studies for Farfield Noise Prediction," AIAA Paper 2001-2158, 2001.

[12] Soderman, P., Kafyeke, F., Burnside, N., Chandrasekharan, R., Jaeger, S., and Boudreau, J., "Airframe Noise Study of a CRJ-700 Aircraft Model in the NASA Ames 7- by 10-Foot Wind Tunnel No.1," AIAA Paper 2002-2406, 2002.

[13] Choudhari, M., Lockard, D., Macaraeg, M., Singer, B., Streett, C., Neubert, G., Stoker, R., Underbrink, J., Berkman, M., Khorrami, M., and Sadowski, S., "Aeroacoustic Experiments in the Low-Pressure Tunnel," NASA TM-2002-211432, 2002.

[14] Khorrami, M., Berkman, M., and Choudhari, M., "Unsteady Flow Computations of Slat With a Blunt Trailing Edge," *AIAA Journal*, Vol. 38, No. 11, Nov. 2000, pp. 2050–2058.

[15] Singer, B., Lockard, D., and Brentner, K., "Computational Aeroacoutics Analysis of Slat Trailing Edge Flow," *AIAA Journal*, Vol. 38, No. 9, 2000, pp. 1558–1564.

[16] K.Takeda, X.Zhang, and Nelson, P., "Computational Aeroacoustic Simulations of Leading-Edge Slat Flow," *Journal of Sound and Vibration*, Vol. 270, 2004, pp. 559–572.

[17] Khorrami, M., Choudhari, M., and Jenkins, L., "Characterization of Unsteady Flow Structures Near Leading Edge Slat: Part II. 2D Computations," AIAA Paper 2004-02802, 2004.

[18] Khorrami, M., Berkman, M., and Singer, B., "Time-Accurate Simulations and Acoustic Analysis of Slat Free-Shear Layer," *AIAA Journal*, Vol. 40, No. 7, July 2002, pp. 1284–1291.

[19] Khorrami, M., Singer, B., and Berkman, M., "Time-Accurate Simulatoins and Acoustic Analysis of Slat Free Shear Layer: Part II," AIAA Paper 2002-2579, 2002.

[20] Choudhari, M. and Khorrami, M., "Effect of Three-dimensional Shear-Layer Structures on Slat Cove Unsteadiness," *AIAA Journal*, Vol. 45, No. 9, September 2007, pp. 2174–2186.

[21] Imamura, T., Enomoto, S., Yokokawa, Y., and Yamamoto, K., "Three-Dimensional Unsteady Flow Computations Around a Conventional Slat of High-Lift Devices," *AIAA Journal*, Vol. 46, No. 5, May 2008, pp. 1045–1053.

[22] Lockard, D. and Choudhari, M., "The Effect of Cross Flow on Slat Noise," AIAA Paper 2010-3835, 2010.

[23] Khorrami, M. and Lockard, D., "Effects of Geometric Details on Slat Noise Generation and Propagation," AIAA Paper 2006–2664, May 2006.

[24] Horne, W., James, K., Arledge, T., Soderman, P., Burnside, N., and Jaeger, S., "Measurements of 26% Scale 777 Airframe Noise in the NASA Ames 40 by 80 Foot Wind Tunnel," AIAA-2005-2810, May 2005.

[25] Khorrami, M. and Choudhari, M., "Application of Passive Porous Treatment to Slat Trailing Edge Noise," NASA TM-2003-212416, May 2003.

[26] Dobrzynski, W., Bieler, H., Chow, L., and Remy, H., "The Airframe Noise Reduction Challenge - Lessons Learnt From the European SILENCER Project," Deurscher Luft- und Raumfahrt Kongress, Braunschweig, Nov. 2006.

[27] Herr, M. and Dobrzynski, W., "Experimental Investigations in Low-Noise Trailing-Edge Design," *AIAA Journal*, Vol. 43, No. 6, June 2005, pp. 1167–1175.

[28] Ortmann, J. and Wild, J., "Effect of Acoustic Slat Modifications on Aerodynamic Properties of High-Lift Systems," *Journal of Aircraft*, Vol. 44, No. 4, July August 2007, pp. 1258–1263.

[29] Ma, Z. and Zhang, X., "Numerical Investigation of Broadband Slat Noise Attenuation with Acoustic Liner Treatment," *AIAA Jornal*, Vol. 47, No. 12, 2009, pp. 2812–2820.

[30] Hayes, J., Horne, W., Solderman, P., and Bent, P., "Airframe Noise Characteristic of a 4.7% Scale DC-10 Model," AIAA-97-1594, 1997.

[31] Khorrami, M., Singer, B., and Radeztsky, R., "Reynolds-Averaged Navier-Stokes Computations of a Flap Side-Edge Flowfield," *AIAA Journal*, Vol. 37, No. 1, Jan. 1999, pp. 14–22.

[32] Streett, C., "Numerical Simulation of Fluctuations Leading to Noise in a Flap-edge Flowfield," AIAA Paper 98-0628, 1998.

[33] Choudhari, M. and Khorrami, M., "Computational Study of Porous Treatment for Altering Flap Side-Edge Flow Field," AIAA Paper 2003-3113, 2003.

[34] Angland, D., Zhang, X., and Molin, N., "Measurements of Flow Around a Flap Side Edge With Porous Edge Treatment," *AIAA Journal*, Vol. 47, No. 7, 2009, pp. 1660–1671.

[35] Storms, B., Hayes, J., Jaeger, S., and Soderman, P., "Aeroacoustic Study of Flap-Tip Noise Reduction Using Continous Moldline Technology," AIAA Paper 2000-1976, 2000.

[36] Koop, L., Ehrenfried, K., Dillmann, A., and Michel, U., "Reduction of Flap Side Edge Noise by Active Flow Control," AIAA Paper 2002-2469, 2002.

[37] Croom, D., "Low-Speed Wind-tunnel Parametric Investigation of Flight Spoilers as Trailing-Vortex-Alleviation Devices an a Transport Aircraft Model," NASA Technical Paper 1419, 1979.

[38] Cole, S., "Effects of Spoiler Surface on a Low-aspect-ratio Rectangular Wing," *J. Aircraft*, Vol. 29, No. 5, 1992, pp. 768–773.

[39] Jr., W. W., Seethram, H., and Calhoun, J., "Wind Tunnel and Flight Development of Spoilers for Ggeneral Aviation Aircraft," SAE Paper 750523, 1975.

[40] Lee, C., Bodapati, S., and Karamcheti, K., "Flow Measurements of an Airfoil with Deflected Spoiler," AIAA Paper 83-0365, 1983.

[41] Bodapati, S., "Unsteady Flow Visualisation of Airfoil with Spoilers," *Proceedings of the Second Asian Congress of Fluid Mechanics., Beijing, China*, 1984, pp. 795–800.

[42] Pfeiffer, N. J. and Zumwalt, G., "Computational Model for Low Speed Flows Past Airfoils with Spoilers," *AIAA Journal*, Vol. 20, No. 3, 1981, pp. 376–382.

[43] Kim, J. H. and Rho, O. H., "Numerical Simulation of Flowfield around airfoil with Stationary or Oscillating Spoiler," *Journal of Aircraft*, Vol. 35, No. 5, 1998, pp. 704–711.

[44] Choi, S. and Chang, K., "Navier-Stokes Computation of a Rapidly Deploying Spoiler," *Journal of Aircraft*, Vol. 37, No. 4, 2000, pp. 655–661.

[45] Consigny, H., Gravelle, A., and Molinaro, R., "Aerodynamic Characteristics of a Two-dimensional Moving Spoiler in Subsonic and Transonic Flow," *Journal of Aircraft*, Vol. 21, No. 9, 1984, pp. 687–693.

[46] de Bray, B., "Low Speed Wind Tunnel Tests on Perforated Square Flat Plates Normal to the Airstream: Drag and Velocity Measurements," Aeronautical Research Council Technical Report C.P. No. 323, 1957.

[47] Castro, I., "Wake Characteristics of Two-dimensional Perforated Plates Normal to an Airstream," *Journal of Fluid Mechanics*, Vol. 46, No. 3, 1971.

[48] Tam, C., "Recent Advances in Computational Aeroacoustics," *Fluid Dynamics Research*, Vol. 38, No. 9, Sept. 2006, pp. 591–615.

[49] Hixon, R., "A New Class of Compact Schemes," AIAA Paper 98-0367, 1998.

[50] Ashcroft, G. and Zhang, X., "Optimized Prefactored Compact Scheme," *Journal of computational physics*, Vol. 190, 2003, pp. 459–477.

[51] Kim, H., Lee, S., and Fujisawa, N., "Computation of Unsteady Flow and Aerodynamic Noise of NACA0018 Airfoil Using Large-Eddy Simulation," *International Journal of Heat and Fluid Flow*, Vol. 27, 2006, pp. 229–242.

[52] Visbal, M. and Gaitonde, D., "High-order Accurate Methods for Complex Unsteady Subsonic Flows," *AIAA Journal*, Vol. 37, No. 10, 1999, pp. 1231–1239.

[53] Yoon, S. and Jameson, A., "Lower-Upper Symmetric Gauss-Seidel Method for the Euler and Navier-Stokes Equations," AIAA Paper 87-0600, 1987.

[54] Spalart, P. and Allmaras, S., "A One-equation Turbulence Model for Aerodynamic Flows," AIAA Paper 92-0439, 1992.

[55] Menter, F., "Two-equation Eddy Viscosity Turbulence Models for Engineering Applications," *AIAA Journal*, Vol. 32, No. 8, 1994, pp. 1598–1605.

[56] Khorrami, M., Berkman, M., Li, F., and Singer, B., "Computational Simulation of a Three-Dimensional High-Lift Wing," AIAA Paper 2002-2804, 2002.

[57] Choudhari, M., Khorrami, M., Lockard, D., Atkins, H., and Lilley, G., "Slat Cove Modelling: A Posteriori Analysis of Unsteady RANS Simulations," AIAA Paper 2002-2468, 2002.

[58] Spallart, P., "Young-Person's Guide to Detached Eddy Simulation Grids," NASA Technical Report CR-2001-211032, July 2001.

[59] Terracol, M., Manoha, E., Herrero, C., Labourasse, E., Redonnet, S., and Sagaut, P., "Hybrid Methods for Airframe Noise Numerical Prediction," *Theoretical Computational Fluid Dynamics*, Vol. 19, 2005, pp. 197–227.

[60] Wang, M. and Moin, P., "Computation of Trailing-edge Flow and Noise Using Large-Eddy Simulation," *AIAA Journal*, Vol. 38, No. 12, 2000, pp. 2201–2209.

[61] Manoha, E., Troff, B., and Sagaut, P., "Trailing edge noise prediction using Large Eddy Simulation and acoustic analogy," *AIAA Journal*, Vol. 38, No. 4, 2000, pp. 575–583.

[62] Deck, S., "Zonal-Detached-Eddy Simulation of The Flow Around a High-lift Configuration," *AIAA Journal*, Vol. 43, No. 11, 2005, pp. 2373–2384.

[63] Spalart, P., Jou, W., Strelets, M., and Allmaras, S., "Comments on the Feasibility of LES for Wings and on a Hybrid RANS/LES Approach," *1st AFSOR Int. Conf. on DNS/LES*, Greyden Press, Columbus, OH, 1997, pp. 137–147.

[64] Shur, M., Spalart, P., Strelets, M., and Travin, A., "Detached-Eddy Simulation of an Airfoil at High Angle of Attack," *4th Int. Symposium on Eng. Turb. Modeling and Experiments*, Corsica, France, 1999.

[65] Spalart, P., Deck, S., Shur, M., Squires, K., Strelets, M., and Travin, A., "A New Version of Detached-Eddy Simulation, Resistant to Ambiguous Grid Densities," *Theor. Comp. Fluid Dyn.*, Vol. 20, 2006, pp. 181–195.

[66] Kim, J. and Lee, D., "Characteristic Interface Conditions for Multiblock High-Order Computation on Singular Structured Grid," *AIAA Journal*, Vol. 41, No. 5, 2003, pp. 2341–2348.

[67] Farassat, F. and Succi, G., "The Prediction of Helicopter Rotor Discrete Frequency Noise," *Vertica*, Vol. 7, No. 4, 1983, pp. 309–320.

[68] Ashcroft, G. and Zhang, X., "A Computational Investigation of the Noise Radiated by Flow-Induced Oscillations," AIAA Paper 2001-0512, 2001.

[69] Richards, S., Zhang, X., Chen, X., and Nelson, P., "The Evaluation of Non-reflecting Boundary Conditions for Duct Acoustic Computation," *Journal of Sound and Vibration*, Vol. 270, No. 3, Feb. 2004, pp. 539–557.

[70] Takeda, K., Zhang, X., Ashcroft, G., and Nelson, P., "Unsteady Aerodynamics of Flap Cove Flow in a High-Lift Device Configuration," AIAA Paper 2001-706, 2001.

[71] Casper, J. H., Lockard, D. P., Khorrami, M. R., and Street, C. L., "Investigation of Volumetric Sources in Airframe Noise Simulations," AIAA Paper 2004–2805, 2004.

[72] Rumsey, C. L. and Ying, S. X., "Prediction of High Lift: Review of Present CFD Capability," *Progress in Aerospace*, Vol. 38, No. 2, 2002, pp. 145–180.

[73] Rizzetta, D., Visbal, M., and Blaisdell, G., "A Time-Implicit High-order Compact Differencing and Filtering Scheme For Large-eddy Simulation," *Int. J. Numer. Meth. Fluids*, Vol. 42, 2003, pp. 665–693.

[74] Oerlemans, S., Broersma, L., and Sijtsma, P., "Quantification of Airframe Noise Using Microphone arrays in Open and Close Wind Tunnels," *International Journal of Aeroacoustics*, Vol. 6, No. 4, 2007, pp. 309–333.

[75] Kanjere, K., Zhang, X., Hu, Z., and Angland, D., "Aeroacoustic Investigation of Deployed Spoiler During Steep Approach Landing," AIAA Paper 2010-3992, 7-9 June 2010.

[76] Dowling, A. and Williams, J. F., *Sound and Sources of Sound*, Ellis Horwood, 1983, pp. 207–208.

[77] Hardin, J., Ristorcelli, J., and Tam, C., "ICASE/LARC Workshop on Benchmark Problems in Computational Aeroacoustics," *ICASE/LARC Workshop on Benchmark Problems in Computational Aeroacoustics*, NASA Conference Publications 3300 Washington DC, 1999.

[78] Tam, C. and Hardin, J., editors, *Proceedings of the Second Computational Aeroacoustic Workshop on Benchmark Problems*, 1997.